Studies on low-carbon aromatics and jet fuel synthesis

低炭素芳香族およびジェット燃料の合成に関する研究

Guo Xiaoyu

郭 暁羽

Supervisor: Prof. Noritatsu Tsubaki

Tsubaki Laboratory

Graduate School of Science and Engineering

University of Toyama

Preface

At present, traditional jet fuels and low-carbon aromatics are mainly delivered from traditional petrochemical industries, with the fossil resource decreasing and the serious pollution caused by fossil fuel combustion, the jet fuels and low-carbon aromatics synthesis by petroleum-free method attracted more and more attention. Besides, the development of petrochemical industries leads to serious of environmental problems such as global warming. Using recyclable raw materials to produce high value-added products instead of traditional petrochemical industrial, such as jet fuel and low-carbon aromatics, which makes more sense to reduce carbon emissions.

Isobutyl alcohol, biological isobutyl alcohol as a new generation biomass energy can be produced through biomass fermentation from non-food crops such as cellulose, The bio-isobutyl alcohol was utilized to produce the jet-range hydrocarbons, and it is a new promising process route which maybe instead of traditional petrochemical industrial route.

The utilization of CO_2, as the main greenhouse gas, have attracted widespread attention to effectively reduce CO_2 emissions, CO_2 as raw materials was hydrogenated into low-carbon aromatics, it seems to be an efficient and replaceable solution for low-carbon aromatics synthesis, which meets the requirements of the sustainable process and carbon emission.

Thus, our work focuses on new catalysts exploits, new catalytic reaction process develops, and new reactor designs in low-carbon aromatics and jet fuel synthesis in the thesis: (1) Catalytic isobutyl alcohol oligomerization to generate liquid fuels over H-Y, SAPO-34, H-MOR zeolite and Al-MCM-41 catalysts (Chapter 1); (2) Various dealuminum methods of zeolite Beta to generate the jet fuels by converting isobutyl alcohol (Chapter 2) ; (3) Multifunctional catalyst composed of Na-Fe@C and hollow H-ZSM-5 for directly converting CO_2 to low-carbon aromatics (Chapter 3).

In chapter 1, It presents an new catalytic process for the direct conversion of isobutyl alcohol into jet-range hydrocarbons. A series of catalysts such as H-Y, SAPO-34, H-MOR zeolite and Al-MCM-41 was developed and applied in direct isobutyl alcohol

conversion to liquid fuels, especially H-MOR shows the best reactivity, achieving 94% conversion of isobutyl alcohol and 63% selectivity C_{5+} liquid fuels, the reaction system was discussed and was considered to be a two-step process i) isobutyl alcohol dehydration reaction via a typical acid catalysis, ii) a polymerization reaction of small molecules into large ones, the present work shows that the pore size and acid property of the zeolite are the two main factors controlling this catalytic dehydration and oligomerization reaction. This work offers a new and efficient method to generate the liquid fuels from isobutyl alcohol directly.

Chapter 2 shows that Beta zeolite by different dealuminum methods shows the different pore size and acid property for direct conversion of isobutyl alcohol into jet-range hydrocarbons. The Beta was treated by the HCl or the EDTA to dealuminate, it shows the different dealuminum process by the strong acid and weak acid, the extra-framework Al was can be partly removed by HCl treatment, which cause the pores of the zeolite Beta become smoother, and the acid property was manipulated by this treatment. Consequently, isobutyl alcohol can be quantitatively oligomerized over the dealuminated zeolite Beta with the selectivity of C_{8-16} exceeding 50% at a conversion of 98%. The present work provides a possible way to develop a promising catalyst for generating jet fuels by catalytic oligomerization from isobutyl alcohol.

In chapter 3, we report a Multifunctional catalyst composed of Na-Fe@C and hollow H-ZSM-5 for directly converting CO_2 to low-carbon aromatics. A carbon encapsulated iron catalyst with Na modification (Na-Fe@C) was prepared using Fe-based metal-organic frameworks (Fe-MOFs) as precursors. Benefiting from the periodic structure of Fe-MOFs, highly dispersed Fe_3O_4 nanoparticles encapsulated by a few graphene-like carbon layers were obtained after pyrolysis of Fe-MOFs under N_2 atmosphere. After combining Na-Fe@C with the NaOH treated H-ZSM-5, the alkenes produced from Na-Fe@C can be converted to aromatics via the dehydrogenation and cyclization reactions on the acidic sites of H-ZSM-5. Surprisingly, the STY of aromatics (203.8 g_{CH2} kg_{cat}^{-1} h^{-1}) obtained from the multifunctional catalyst composed of Na-Fe@C and hollow H-ZSM-5. Furthermore, the driving force in the tandem process was also

clarified, the interplay between the two catalyst components facilitated the dehydrogenation and cyclization reactions of the intermediate alkenes, which was beneficial for the aromatics synthesis. This work offers a simple and effective strategy to synthesize low-carbon aromatics from CO_2 under mild conditions directly.

.

Contents

Chapter 1

Catalytic Oligomerization of Isobutyl Alcohol to

Hydrocarbon Liquid Fuels over Acidic Zeolite Catalysts

Abstract

Catalytic isobutyl alcohol oligomerization to generate hydrocarbon liquid fuels over zeolite has been investigated over H-Y, SAPO-34, H-MOR zeolite and Al-MCM-41 catalysts, as a new way to direct conversion of isobutyl alcohol to hydrocarbon liquid fuels, considering the fact that isobutyl alcohol can be obtained from biomass by microbes. In this study, all of the zeolite samples showed good reactivity, especially H-MOR, achieving 94% conversion of isobutyl alcohol and 63% selectivity of C_{5+} liquid fuels in all products. The effects of reaction conditions including reaction temperature and reaction time were also discussed. The physicochemical properties of the catalysts were characterized by XRD, Nitrogen adsorption-desorption, NH3-TPD, TG/DTA, and GS/MS. The reaction system discussed here involves two reactions, i) isobutyl alcohol dehydration reaction via a typical acid catalysis, ii) a polymerization reaction of small molecules into large ones, according to the experimental and characterization results, the pore size and acid property of the zeolite are the two main factors controlling this catalytic dehydration and oligomerization reaction

Keywords: Isobutyl alcohol; Jet fuel; Liquid fuels; Mordenite; Oligomerization.

1.1. Introduction

Global demand for energy is predicted to increase in the coming decade, considering the decreasing crude oil especially petroleum resources, which has attracted widespread attention. [1] Liquid fuel, since its wide application, plays a dominant role in the transport sector. [2] In this context, main researches in the field of renewable and clean fuels focus on alcohol which can be used to substitute the conventional liquid fuels partially. [3,4]

Alcohol (for example. especially methanol/ethanol until now) oligomerization reactions are main reactions, which have been wildly employed for generating ultra-clean fuels and hydrocarbons. In past decades, various types of catalysts such as alumina, solid acids and zeolites have been investigated for alcohol oligomerization reaction. [5-12] Isobutyl alcohol, as the next-generation biofuels, has attracted much attention from global researchers. Nowadays, isobutyl alcohol has mainly been obtained via two routes: direct formation through non-fermentative pathways from vegetable fiber and the indirect syngas conversion to isobutyl alcohol, which makes isobutyl alcohol as a promising chemical or energy intermediate available from the viewpoint of industry. [13-18] Therefore, direct conversion of higher alcohols such as isobutyl alcohol into hydrocarbon liquid fuels becomes a potential industrialization technology. However, there exist very few studies devoted to the isobutyl alcohol oligomerization to liquid fuels.

$$C_4H_9OH \rightarrow C_4H_8 + H_2O \qquad (1)$$

$$C_4H_8 + C_4H_8 \rightarrow C_8H_{16} \quad C_4H_8 + C_8H_{16} \rightarrow C_{12}H_{24} \ldots \qquad (2)$$
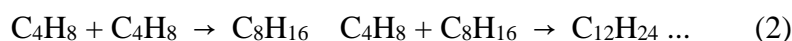
The catalytic oligomerization of isobutyl alcohol to liquid fuels includes two catalytic steps: (1) isobutyl alcohol dehydration to isobutylene, and (2) isobutylene oligomerization to C_{5+} hydrocarbons. In the first step, alcohol dehydration as an endothermic reaction requires strong acid sites. In addition, different from methanol or

ethanol dehydration, isobutyl alcohol dehydration is thermodynamically favored of high temperatures. [19,20] Thus the solid acids other than zeolite are not suitable for the isobutyl alcohol dehydration reaction. On the contrary, zeolite materials with ordered microporous structures have been widely used as the most important solid catalysts in many industrial processes. [21,22] For example, silica-alumina phosphate zeolite SAPO-34 with the CHA topological structure has attracted widespread attention due to its excellent catalytic performance in the methanol-to-olefin (MTO) reaction field. [5] Compared with the traditional zeolite, MCM-41 with mesoporous structure has a much-decreased transport resistance that may increase the utilization of acidic sites by bulky molecules. Although the pure silica MCM-41 does not have acidic sites, the acidity can be provided by the incorporation of metal ions such as aluminum, titanium, and zirconium into the framework structure, which makes it a candidate acid catalyst for several organic reactions. [7,8] G.R.Moradi et al. demonstrated that H-mordenite zeolite is a promising and attractive catalyst for methanol dehydration, achieving 96% conversion and 98% selectivity to DME for methanol dehydration reaction. [6]

The second step is isobutylene oligomerization, a typical acid catalysis reaction. [23,24] Catalysts are mainly divided into traditional liquid acid catalysts and solid acid catalysts. Via acid catalysis, it is generally believed that the process is based on the mechanism of carbonium ions.[25-27] Yoon et al. [28] reported that H-MOR, H-Y, H-BEA zeolites exhibited high activity on isobutylene oligomerization, in which the H-BEA shows 100% conversion and 60% selectivity to trimers of isobutene, avoid using un-stable cation exchanged resin, heteropoly acid, sulfated titania catalysts at the higher temperature. [27-31]

It is noted that both reaction (1) and reaction (2) can be catalyzed by acidic zeolite, providing a clue for combining both reactions to directly produce hydrocarbon liquid fuels through isobutyl alcohol oligomerization. Therefore, the catalytic oligomerization of isobutyl alcohol to liquid hydrocarbons over different commercial catalysts such as H-Y, Al-MCM-41, H-MOR, and H-SAPO-34 was investigated in detail with a batch reactor. In addition, related effects of the catalyst factors such as acid site, pore structure,

and pore size, for influencing reactive activity were also studied via the utilization of XRD, Nitrogen adsorption-desorption, NH_3-TPD, TG/DTA.

1.2. Experimental

1.2.1. Catalyst preparation

Catalysts are summarized in Table 1.1 Commercial zeolites with the ammonium form were calcined at 500 °C for 4 h to thermally decompose NH^{4+} to H^+ and NH_3.

1.2.2. Characterization

XRD patterns of catalysts were analyzed by RINT 2400 System (Rigaku, Japan) with Cu-Kα radiation (λ=0.154 nm) at 40 kV and 20 mA. The scan was at a rate of 0.02°/min.

N_2 physisorption tests were carried out with a NOVA-2200e, Quantachrome Instruments equipment. Prior to tests, samples of 50-60 mg were first degassed at 300 °C for 2 h. Afterward, the N_2 adsorption isotherms were recorded at -196 °C to obtain the surface area, pore volume and the average pore size according to the BJH method.

The acidity of catalysts was studied by the temperature programmed desorption (TPD) using BELCAT-B-TT (BEL.JAPAN INC.) with NH_3. The TPD of NH_3 was carried out between 50 °C and 900 °C under a helium flow (30 mL/min) with a heating rate of 10 °C/min. Before the test, the samples were pretreated under helium atmosphere at 500 °C for 1 h, then, cooled to 50 °C, and exposed to pure NH_3 (30 mL/min) for 0.5 h.

The char/coke was analyzed through thermogravimetric analysis (DTA/TGA-60, Shimadzu). It was carried out in a METTLER TOLEDO STARe system, with the heating rate of 10 °C/min under air atmosphere to identify the type of char and coke as well as to determine the total amounts of carbon deposition in the spent catalysts.

The liquid fuels were confirmed by the gas chromatography-mass spectrometry (GC-MS Shimadzu GCMS 1600).

Pyridine adsorption (Py-IR) spectra were recorded with a Tensor 27 IR spectrometer from Bruker. The H-Y and H-MOR samples were directly pressed into thin wafers,

which were mounted into a vacuum cell. Prior to the measurement, the sample cell was evacutated to 10^{-2} Pa at 500°C for 1h, the IR spectra were then recorded at150°C.

1.2.3. Catalytic tests

Isobutyl alcohol oligomerization reaction was carried out in an 85 mL steel batch reactor. In brief, 0.5 g of the catalyst and 10 ml of isobutyl alcohol (2-Methyl-1-Propanol, Tokyo Chemical Industry) were placed into the reactor. Then the reactor system was purged three times with N_2 to remove the trapped air. After purging, the reactor was pressurized with N_2 of 1 MPa, and then the reactor system was heated up to reaction temperature.

After the reaction, the reactor was cooled down to the 0 °C and then depressurized to atmospheric pressure to collect the gas product. Liquid phase products were separated by the filter. The liquid products were analyzed by a capillary chromatography (GC-14B, FID, Shimadzu, Japan). The gas products were also analyzed by another capillary chromatography (GC-14B, FID, Shimadzu, Japan). The filtered solid was then washed three times with n-hexane (100 mL, each time) and dried at 120 °C for 12 h for further analysis.

The conversion of isobutyl alcohol was calculated by monitoring its disappearance:

Isobutyl alcohol conversion (%) = [1-($C_{mole\ of\ isobutyl\ alcohol\ after\ reaction}$)/($C_{mole\ of\ initial\ isobutyl\ alcohol}$)]*100%

The selectivity of component i was calculated by monitoring its disappearance at carbon mol. base:

Sel. C_i = ($C_{mole\ of\ Ci\ hydrocarbon}$/$\sum_{i=1}^{n} C_{mole\ of\ Ci\ hydrocarbon}$) *100%

1.3. Results and discussion

1.3.1. Catalytic performance

The crystalline structures of SAPO-34, H-MOR, H-Y, and Al-MCM-41 zeolites obtained from different companies were confirmed by X-ray diffraction analysis. In the XRD patterns (Figure 1.1), all characteristic diffraction peak positions matched those reported for H-MOR, SAPO-34, and H-Y zeolite structure respectively, and no-impurity phase was observed. [5,18] For Al-MCM-41, the XRD pattern with 2 theta at the range of $2-8°$ was presented in below. The characteristic reflctions in the XRD pattern of MCM-41 correspond to (100) and (110) hexagonal planes and are regarded as the character of highly ordered MCM-41.

The NH_3-TPD was used to confirm the acidity of the different types of catalysts. As shown in Figure 1.2, all of these catalysts have two similar peaks: the desorption peak distributing around 170 ℃ could be described to weak acid sites, while the desorption peak around 400 ℃ was assigned to strong acid sites which could be further divided to strong Brønsted acid sites formed by the framework Al atoms in the zeolite [32]. Therefore, the strength of strong acid sites decreases in the order of Al-MCM-41 > H-MOR ≥ H-Y ≥ SAPO-34 . Generally, the strong BrØnsted acid sites were indispensable for isobutyl alcohol dehydration and the subsequent oligomerization reaction., Different from the order of strong sites, the ranking of weak acid sites strength is in the order of H-MOR > SAPO-34 > Al-MCM-41 > H-Y. Both of strong acid sites and weak acid sites as a vital factor for the reaction, will be discussed below.

The textural properties the are summarized in Table 1.2, and the N_2 adsorption-desorption curves and pore size distribution was shown in Figure 1.3. As seen, SAPO-34 exhibits a single micropore structure among these zeolites. However the mesopore ratio is constantly increased with the order of H-MOR, H-Y, and Al-MCM-41. It is noted that Al-MCM-41 is almost fully mesoporous, and the influence of the varied pores on catalytic performance is to be expected and will be further discussed below.

During the oligomerization process of isobutylene, the acid site, pore structure, as well as crystalline size of the catalyst, play crucial factors. However, there is no systematic investigation concerning their influences on isobutyl alcohol

oligomerization reaction yet. Herein, we first investigate the effects of these factors on the catalytic performance. H-MOR, H-Y, SAPO-34, and Al-MCM-41 were evaluated, and the results were summarized in Figure 1.4. For the isobutyl alcohol oligomerization reaction, there still exist some side reactions, such as undesired diisobutyl Ether (DIE) formation (equation 3) and the cracking reaction forming gaseous hydrocarbons. To further compare the catalytic performance, these by-products are listed in others as shown in Table 1.3.

$$2 \text{ iso-C}_4\text{H}_9\text{OH} \rightarrow (\text{iso-C}_4\text{H}_9)_2\text{O} + \text{H}_2\text{O} \qquad (3)$$
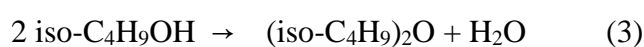
As discussed above, isobutyl alcohol oligomerization reaction is divided into two reactions, the isobutyl alcohol dehydration into water and isobutylene, followed by isobutylene oligomerization to the target liquid fuels. Therefore, the conversion of isobutyl alcohol is strongly related to the dehydration abilities of various catalysts. By contrary, the selectivity of isobutylene stands for the oligomerization ability of the catalysts, for example, the lower selectivity of the isobutylene, the better oligomerization ability.

To gain more sight, the molecular size of main reactants and the pore openings of zeolite were listed in Table 1.4, we can find that molecular volume of reactants is too large for SAPO-34 to enter the channel structure, just reacting at the outer surface of SAPO-34. More importantly, it should be noted that the diffusion limitation of the reactants will be a major factor controlling isobutyl alcohol catalytic dehydration and subsequent oligomerization reaction where small molecules are oligomerized to large molecules. So, for Al-MCM-41, with 3nm pore opening which is much larger than the molecular size of reactants and products, the diffusion resistance of the reactants is much lower than in H-MOR and H-Y, which may advantageous to the oligomerization reaction [33].

Compared with H-Y, both Al-MCM-41 and H-MOR with higher strong acid strength exhibit higher reactivity of isobutyl alcohol dehydration, reaching isobutyl alcohol

conversion of 74% and 82%, respectively (Figure 1.4 and Table 1.3). As for H-Y zeolite with lower strong acid strength, the conversion of isobutyl alcohol is only 53%. This phenomenon well with the view of Ordomsky et al. that strong acid sites of the catalyst play a critical factor in isobutyl alcohol conversion. [34] Moreover, the strength of strong acid sites decreases in the order Al-MCM-41 > H-MOR ≥ H-Y. As depicted in Figure 1.2, both reactions of isobutanol dehydration and the isobutylene oligomerization are based on the mechanism of carbonium ions, and the oligomerization of isobutylene consumes carbonium ions and promotes the dehydration of isobutyl alcohol. However, the isobutyl alcohol conversion of Al-MCM-41 with higher strength of strong acid is lower than that of H-MOR, which may be due to a balance between the initial isobutyl alcohol dehydration and the subsequent isobutylene oligomerization. Al-MCM-41 zeolite was also not suitable for dehydration process owing to the low weak acid sites. H-MOR zeolite with a better capability of isobutylene oligomerization is able to convert more isobutylene into C_{5+} liquid hydrocarbon, which then enhances the conversion of isobutyl alcohol to isobutylene by the shift effect of this consecutive process.

There is a lot of literature dealing with the shape selective functions of SAPO-34 on MTO reaction, [35-37] but it seems that these are not effective in isobutyl alcohol oligomerization reaction. This phenomenon may be due to the fact that molecular volume of isobutylene is too large for SAPO-34 to enter the channel structure, just reacting at the outer surface of SAPO-34. Consequently, for the tested catalysts, H-MOR has the highest conversion and better selectivity.

TG/DTA was used to analyze the carbon deposition on spent catalysts. The results of spent zeolite are illustrated in Figure 1.5, which can provide information about the coke weight of spent catalyst. Obviously, after reaction, the carbon deposition appears. However, the endothermic peak over 200°C-400°C which defined as week coke, and over 400°C which is the hard coke. we can especially find that the main coke of SAPO-34 is the hard coke, and for Al-MCM-41 which is main week coke, which by my opinion is the hard coke of SAPO-34 cause the low activity during the reaction process

In order to disclose the isobutyl alcohol oligomerization reaction behavior in detail, the effect of reaction temperature was investigated. The catalytic performance of H-MOR under the changed reaction temperature was listed in Table 1.5. According to Table 1.3, the catalysts exhibited benign behavior with the conversion of 82%. Furthermore, there is a volcanic relationship between the conversion and reaction temperature, in which the conversion approaches the maximum value at 240°C. The reasons listed below may explain the observed behavior: first, the reaction for isobutyl alcohol oligomerization is two-step: the reaction (1) is the dehydration of isobutyl alcohol, an endothermic reaction in which high temperature is helpful for the dehydration; however, the reaction (2) is an exothermic reaction. To the coupled reactions, there must exist an optimum reaction temperature. Second, considering the physical properties of isobutyl alcohol, the boiling point of isobutyl alcohol is at 108°C while the critical temperature is at 260°C. Therefore, the partial isobutyl alcohol was inevitably changed from liquid state to gas state when the reaction temperature exceeded the critical temperature and then decreased the contact interface with catalysts. Thus, the conversion of isobutyl alcohol finally decreased with temperature enhancement as demonstrated.

The effect of reaction time on isobutyl alcohol oligomerization is depicted in Figure 1.6. As seen, conversion of the catalysts was increased rapidly from 30% to 74% at first 2h and then approached to the maximum by a continuous but significantly lower linear increase, reaching 94% at 10h. However, the selectivity of the isobutylene decreased in the first 6h and then stabilized at 30%, which should result from the coke deposition process during oligomerization reaction. Different from isobutylene selectivity, the selectivity of C_{12+} was increased between 6h and 8h while the oligomerization reaction was still in progress.

To explain the observed activity phenomenon of H-MOR, TG/DTA was used to analyze the spent catalysts. The results of spent H-MOR are illustrated in Figure 1.7, which can provide information about the coke weight of spent catalyst. Obviously, after 1h reaction, the carbon deposition appears. However, with the prolonged reaction time,

the endothermic peak occurs at 300°C. Besides, after 2h reaction, the endothermic peak shifts to 400°C - 600°C. According to catalytic performance (Figure 1.6), the catalyst presents high activity in the first 2h, which is consistent with the observation from TG/DTA where the high catalytic activity leads to the rapid formation of carbon deposits. Furthermore, an endothermic peak between 400°C and 600°C is gradually increased from 4 h to 8 h. Meanwhile, the selectivity of C_{9+} is increased, which may be ascribed to the coke deposition process during oligomerization reaction. And 8h and 10h have essentially the same endothermic peak. At the same time, the product selectivity has not changed, but the dehydration is still in progress. Thus the endothermic peak between 400°C and 600°C is assigned to the formed hard coke in the catalysts, which may result in the deactivation of oligomerization reaction. On the other hand, the endothermic peak at 300°C may be ascribed to the heavy oligomers, which does not influence the catalytic performance.

1.4. Conclusions

   In conclusion, a series of zeolites were adopted for dehydration reaction of isobutyl alcohol to generate liquid hydrocarbon fuels. SAPO-34 zeolite was easy to be deactivated due to the presence of microporous, while Al-MCM-41 zeolite was also not suitable for dehydration process owing to the low weak acid sites. By contrary, isobutyl alcohol conversion of 82% and C_{5+} olefins of 58% were achieved on H-MOR zeolite at 240°C. In addition, the conversion was enhanced with increasing temperature and reached its maximum at 240°C. Obviously, the factors that affect the catalytic performance include not only the physicochemical properties of catalysts (such as pore structure and the acid sites) but also the physical properties of isobutyl alcohol. With the proceeding of reaction, the conversion of the catalysts was increased rapidly at first 4 h from 30% to 82% and then slowly increased to the maximum level of 94% at 10 h. According to the results of TG/DTA, the generating of hard coke made the deactivation of the catalyst rapidly. These findings provide new insights for the potential applications of isobutyl alcohol oligomerization to liquid hydrocarbon fuels.

References

[1] Q. Zhang, J. Kang, Y. Wang, ChemCatChem. **2010,** *2*, 1030–1058.

[2] Q. Fu, W.X. Li, Y. Yao, H. Liu, H.Y. Su, M. Ding, X.K. Gu, L. Chen, Z. Wang, H. Zhang, B. Wang, X. Bao, Science **2010**, *328*, 1141–1144.

[3]Q. Cheng, N. Zhao, S. Lyu, Y. Tian, F. Gao, L. Dong, Z. Jiang, J. Zhang, N. Tsubaki, X. Li, Appl. Catal. B Environ. **2019,** 73–83.

[4] L. Guo, Y. Cui, P. Zhang, X. Peng, Y. Yoneyama, G. Yang, N. Tsubaki, ChemistrySelect. **2018**, *3*, 13705–13711.

[5] Q. Sun, N. Wang, G. Guo, J. Yu, Chem. Commun. **2015**, *51*, 16397–16400.

[6] G.R. Moradi, F. Yaripour, P. Vale-Sheyda, Fuel Process. Technol. **2010**, *91*, 461–468.

[7] S.P. Naik, V. Bui, T. Ryu, J.D. Miller, W. Zmierczak, Appl. Catal. A Gen. **2010**, *381*, 183–190.

[8] Q. Tang, H. Xu, Y. Zheng, J. Wang, H. Li, J. Zhang, Appl. Catal. A Gen. **2012**, *413–414*, 36–42.

[9] V. Vishwanathan, K.W. Jun, J.W. Kim, H.S. Roh, Appl. Catal. A Gen. **2004**, *276*, 251–255.

[10]S. Wang, Y. Chen, Z. Qin, T.S. Zhao, S. Fan, M. Dong, J. Li, W. Fan, J. Wang, J. Catal. **2019**, 382–395.

[11]S. Wang, P. Wang, Z. Qin, Y. Chen, M. Dong, J. Li, K. Zhang, P. Liu, J. Wang, W. Fan, ACS Catal. **2018**, *8*, 5485–5505.

[12]S. Wang, S. Li, L. Zhang, Z. Qin, Y. Chen, M. Dong, J. Li, W. Fan, J. Wang, Catal. Sci. Technol. **2018**, *8*, 3193–3204.

[13]S. Atsumi, T. Hanai, J.C. Liao, Nature. **2008**, *451*, 86–89.

[14]M.M. El-Dalatony, E.S. Salama, M.B. Kurade, K.Y. Kim, S.P. Govindwar, J.R. Kim, E.E. Kwon, B. Min, M. Jang, S.E. Oh, S.W. Chang, B.H. Jeon, Chem. Eng. J. **2019**, 797–805.

[15]L. Devi, K.J. Ptasinski, F.J.J.G. Janssen, Biomass and Bioenergy. **2003**, *24*, 125–140.

[16] T. Zhang, Y. Wu, X. Gao, H. Xie, G. Yang, N. Tsubaki, Y. Tan, Fuel. **2019**, *237*, 1021–1028.

[17] X. Gao, T. Zhang, Y. Wu, G. Yang, M. Tan, X. Li, H. Xie, J. Pan, Y. Tan, Fuel. **2018**, *217*, 21–30.

[18] X. Gao, Y. Wu, T. Zhang, L. Wang, X. Li, H. Xie, Y. Tan, Catal. Sci. Technol. **2018**, *8*, 2975–2986.

[19] Z. Buniazet, C. Lorentz, A. Cabiac, S. Maury, S. Loridant, Mol. Catal. **2018**, *451*, 143–152.

[20] Z. Buniazet, A. Cabiac, S. Maury, D. Bianchi, S. Loridant, Appl. Catal. B Environ. **2019**, 594–603.

[21] X. Gao, B. Xu, G. Yang, X. Feng, Y. Yoneyama, U. Taka, N. Tsubaki, Catal. Sci. Technol. **2018**, *8*, 2087–2097.

[22] X. Feng, P. Zhang, Y. Fang, W. Charusiri, J. Yao, X. Gao, Q. Wei, P. Reubroycharoen, T. Vitidsant, Y. Yoneyama, G. Yang, N. Tsubaki, Catal. Today. **2019**,

[23] K. Hauge, E. Bergene, D. Chen, G.R. Fredriksen, A. Holmen, Catal. Today. **2005**, *100*, 463–466.

[24] J.W. Yoon, J.S. Chang, H. Du Lee, T.J. Kim, S.H. Jhung, J. Catal. **2007**, *245*, 253–256.

[25] J.N. Kondo, K. Domen, J. Mol. Catal. A Chem. **2003**, *199*, 27–38.

[26] R. Alcántara, E. Alcántara, L. Canoira, M.J. Franco, M. Herrera, A. Navarro, React. Funct. Polym. **2000**, *45*, 19–27.

[27] T.K. Phung, L. Proietti Hernández, A. Lagazzo, G. Busca, Appl. Catal. A Gen. **2015**, *493*, 77–89.

[28] J.W. Yoon, S.H. Jhung, D.H. Choo, S.J. Lee, K.Y. Lee, J.S. Chang, Appl. Catal. A Gen. **2008**, *337*, 73–77.

[29] P. Liu, E. Redekop, X. Gao, W.-C. Liu, U. Olsbye, G.A. Somorjai, J. Am. Chem. Soc. **2019**, *141*, 11557–11564.

[30] E. Kocaman, Ö. Akarçay, N. Bağlar, S. Çelebi, A. Uzun, Mol. Catal. **2018**, *457*, 41–50.

[31] M. Ma, E. Zhan, X. Huang, N. Ta, Z. Xiong, L. Bai, W. Shen, Catal. Sci. Technol. **2018**, *8*, 2124–2130.

[32] S.A. Bates, W.N. Delgass, F.H. Ribeiro, J.T. Miller, R. Gounder, J. Catal. **2014**, *312*, 26–36.

[33] K.P. Möller, M. Kojima, C.T. O'Connor, Chem. Eng. J. Biochem. Eng. J. **1994**, 54, 115–123.

[34] V. V. Ordomsky, J. Van Der Schaaf, J.C. Schouten, T.A. Nijhuis, J. Catal. **2012**, *287*, 68–75.

[35] B.P.C. Hereijgers, F. Bleken, M.H. Nilsen, S. Svelle, K.P. Lillerud, M. Bjørgen, B.M. Weckhuysen, U. Olsbye, J. Catal. **2009**, *264*, 77–87.

[36] D. Chen, K. Moljord, T. Fuglerud, A. Holmen, Microporous Mesoporous Mater. **1999**, *29*, 191–203.

[37] X. Li, F. Rezaei, D.K. Ludlow, A.A. Rownaghi, Ind. Eng. Chem. Res. **2018**, *57*, 1446–1453.

Tables and Figures

Table 1.1. The properties of different catalysts for the isobutanol oligomerization

Catalysts	Topology	Composition	Preparation	Manufacturer
H-MOR	MOR(1D)	SiO_2/Al_2O_3 mol 18	Calcined at 500 °C for 4h	TOSOH
H-Y	FAU(3D)	SiO_2/Al_2O_3 mol 15	Calcined at 500 °C for 4h	TOSOH
SAPO-34	CHA(3D)	SiO_2/Al_2O_3 mol 4.2	Calcined at 500 °C for 4h	ACS MATERIAL
Al-MCM-41	Mesoporous Silica	SiO_2/Al_2O_3 mol 25	Calcined at 500 °C for 4h	ACS MATERIAL

Table 1.2. BET results of the zeolite after calcination

Catalysts	Surface area/ (m^2g^{-1})			Pore volume/(cm^3g^{-1})		
	Total	Micropore	Mesopore	Total	Micropore	Mesopore
SAPO-34	557	540	0	0.28	0.28	0.00
H-MOR	436	407	0	0.26	0.20	0.00
H-Y	651	556	0	0.56	0.29	0.00
Al-MCM-41	658	49	589	0.76	0.02	0.70

Table 1.3. Catalytic performance of isobutanol oligomerization using varied catalysts

Catalysts	Reaction time	Temperature	Conv. (%)	Hydrocarbon Selectivity (%)			
				C_4 olefin	C_5-C_8 olefin	C_{9+} olefin	others
H-MOR	4h	240°C	82	35	45	13	7
H-Y	4h	240 °C	53	46	35	9	10
SAPO-34	4h	240 °C	37	20	47	32	1
Al-MCM-41	4h	240 °C	74	48	36	10	6

(**a**) Reaction conditions: isobutyl alcohol 10 mL; reaction time: 4h; catalyst weight: 0.5 g; loaded gas: N_2 1.0 MPa.

Table 1.4. The molecular size of reactants, and pore openings of each zeotype material.

Isobutyl alcohol	Isobutylene	Diisobutyl Ether	Diisobutylene	Triisobutylene	H-MOR	Al-MCM-41	H-Y	SAPO-34
0.53x 0.42nm	0.42x 0.42nm	0.75x 0.44nm	0.75x 0.44nm	0.83x 0.51nm	0.65 nm	3nm	0.73 nm	0.37 nm

Table 1.5. Catalytic performance of isobutyl alcohol oligomerization under varied temperature with H-MOR (SiO$_2$/Al$_2$O$_3$ mol = 18) catalyst[a].

Zeolite	Temp.(ºC)	Conv.(%)	Hydrocarbon Selectivity(%)			
			C$_4$ olefin	C$_5$-C$_8$ olefin	C$_{9+}$ olefin	others
H-MOR	280	48	29	52	8	11
H-MOR	260	46	25	54	7	14
H-MOR	240	82	35	45	13	7
H-MOR	220	54	11	57	24	8
H-MOR	200	43	9	58	28	5

(**a**) Reaction conditions: isobutyl alcohol 10 mL; reaction time: 4h; catalyst weight: 0.5 g; loaded gas: N$_2$ 1.0 MPa.

20
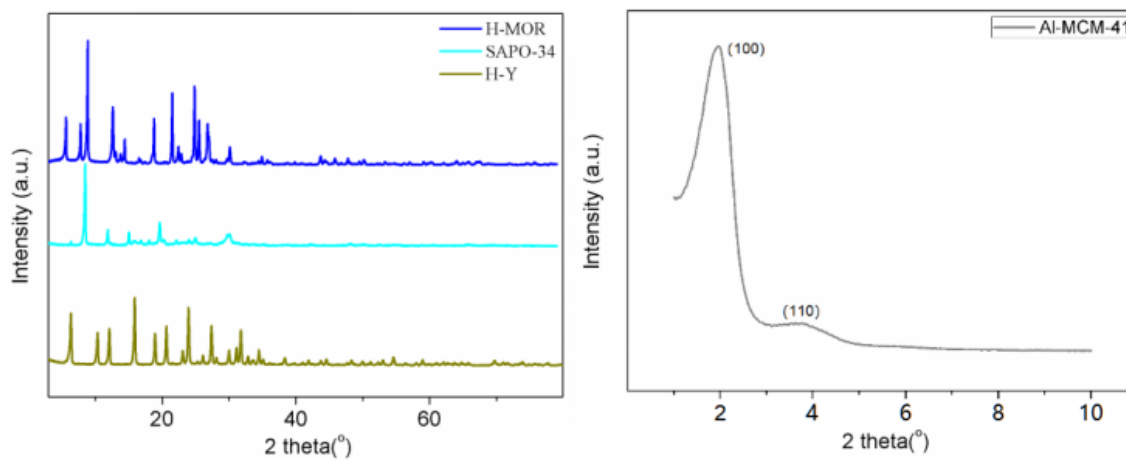
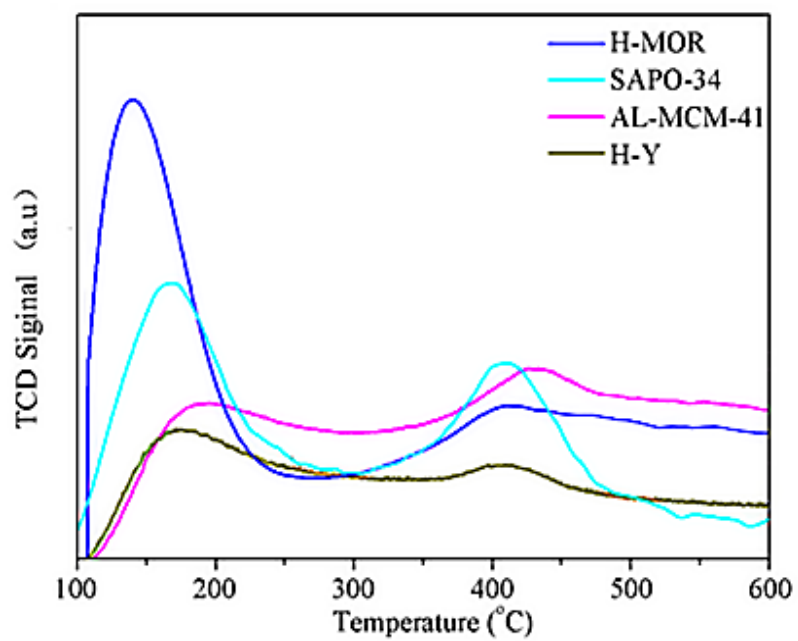**Figure 1.1. XRD patterns of the zeolite after calcination.**

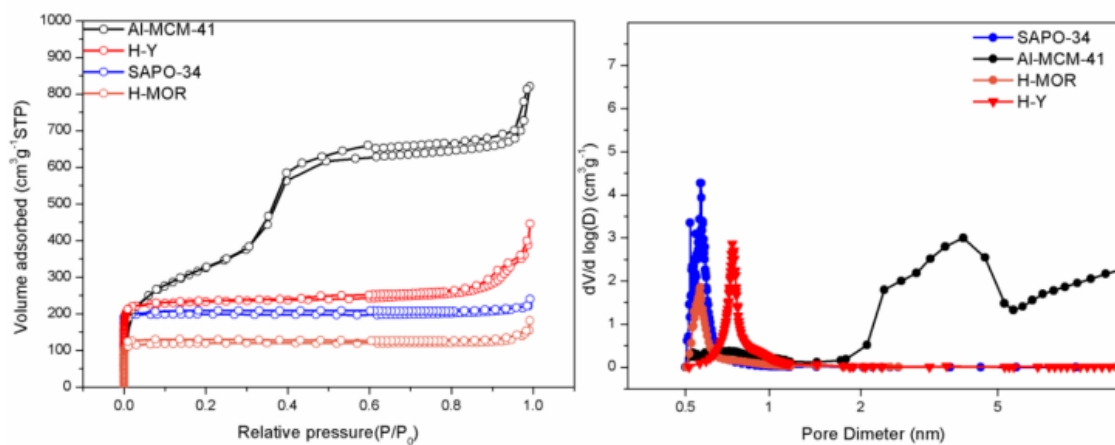**Figure 1.2. NH₃-TPD of the zeolite after calcination**

Figure 1.3. N₂ adsorption-desorption curves and pore size distribution plots of the sample.

Figure 1.4. Catalytic performance of isobutyl alcohol oligomerization with different catalysts.(Reaction conditions: isobutyl alcohol 10 mL; reaction temperature: 240 ℃; reaction time: 4h; catalyst weight: 0.5 g; loaded gas: N₂ 1.0 MPa.)

Figure 1.5. The TG/DTA result of the spent zeolites (Inserted number stands for the final weight left)
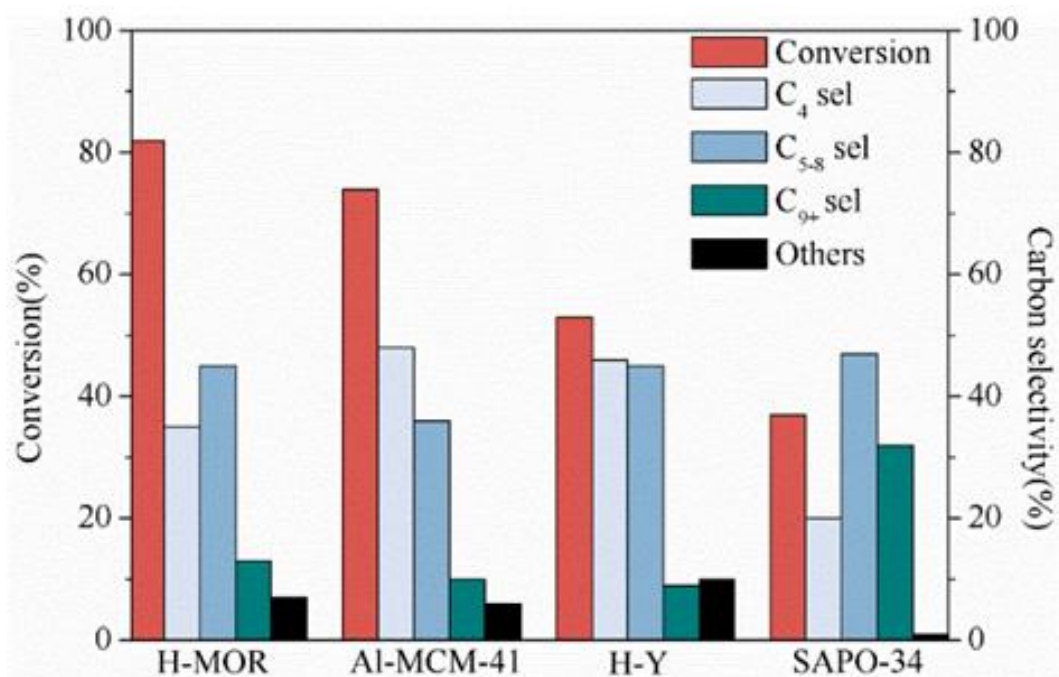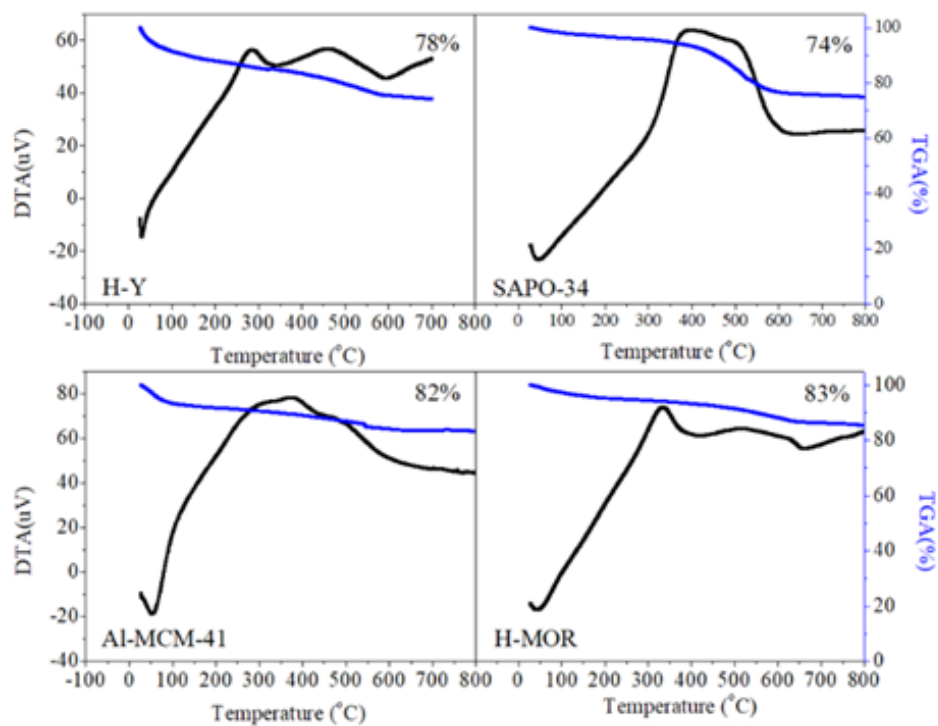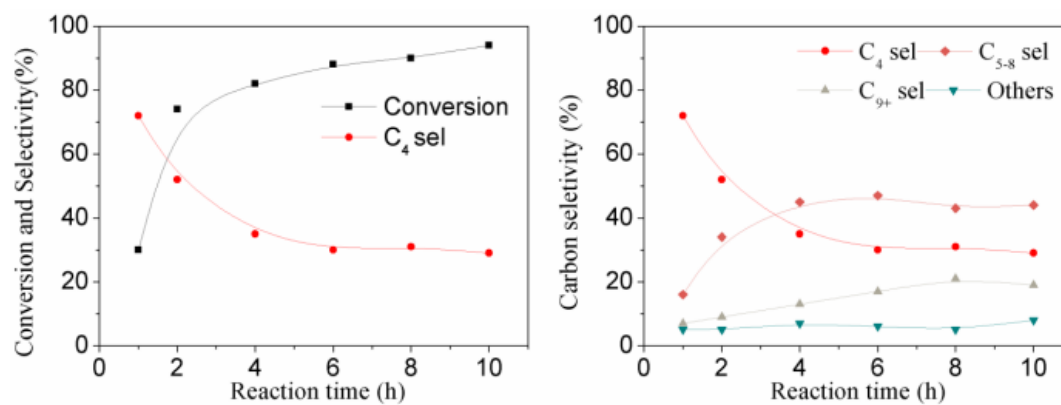
Figure 1.6. Catalytic performance of isobutyl alcohol oligomerization with varied reaction time.(Reaction conditions: isobutyl alcohol 10 mL; reaction temperature: 240 °C;   catalyst weight: 0.5 g; loaded gas: N_2 1.0 MPa.)

Figure 1.7. The TG/DTA result of the spent H-MOR catalysts in different reaction times. (Inserted number stands for the final weight left)

Chapter 2

Catalytic Oligomerization of Isobutyl Alcohol to Jet Fuels over Dealuminated Zeolite Beta
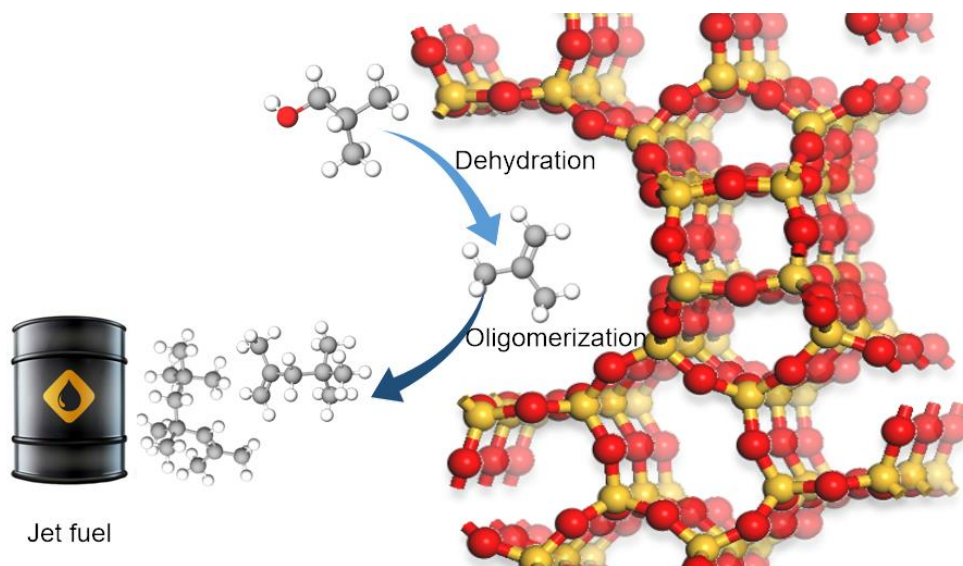
Abstract

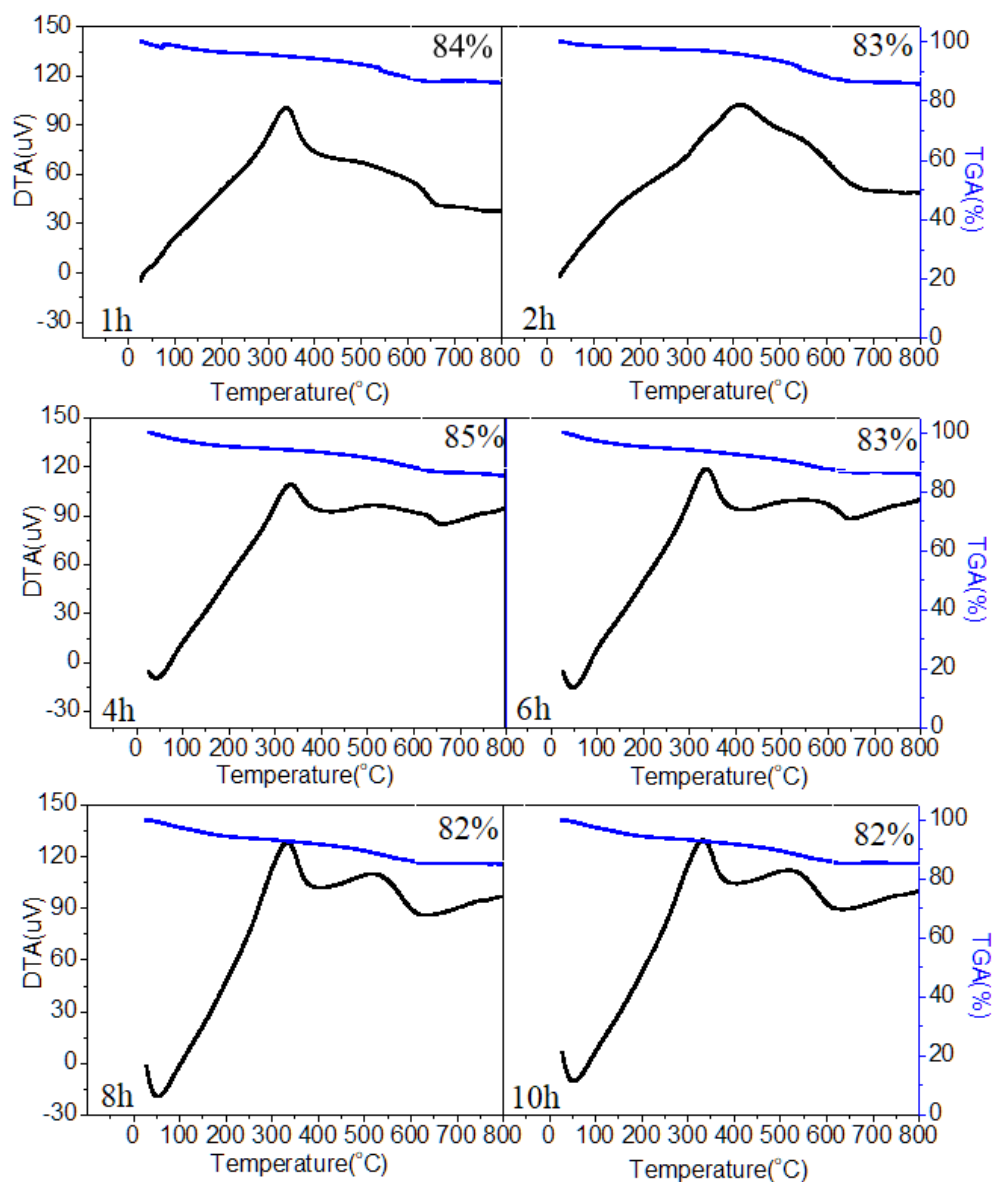Various dealuminum methods of zeolite Beta to generate the jet fuels by converting isobutyl alcohol has been investigated in detail. And related factors of the zeolite catalyst such as acid site, pore structure, and pore size which can influence reactive activity, were also studied utilizing XRD, SEM, XRF, Nitrogen adsorption-desorption, NH_3-TPD, Py-FTIR, and ^{27}Al solid-state NMR. Removal of extra-framework aluminum or part of framework aluminum by hydrochloric acid dealumination, is able to improve the diffusion property of the products in the channel of zeolite Beta via increasing the ratio of Lewis/Brønsted. Consequently, isobutyl alcohol can be quantitatively oligomerized over dealuminated zeolite Beta with the selectivity of C_{8-16} exceeding 50% at a conversion of 98%. Moreover, the deactivated catalyst can be easily regenerated by calcining it in flowing air. High conversion, high jet fuels selectivity, and facile regeneration make it an attractive potential catalyst for isobutyl alcohol oligomerization reaction.

Keywords: Isobutyl alcohol; Oligomerization; Beta zeolite; Jet fuels; Dealumination.

2.1. Introduction

At present, jet fuels are mainly obtained through traditional petrochemical and coal chemical industries. Considering the shortage of traditional fossil energy and the growing market demand, the development and utilization of biomass have become the current research hotspot. More recently, biological isobutyl alcohol as a new generation biomass energy can be produced through biomass fermentation [1,2]. The production of jet-range hydrocarbons utilizing biological isobutyl alcohol as a raw material is a very new promising process route that does not depend on traditional fossil energy sources.

Industrial production methods of isobutyl alcohol mainly include chemical synthesis and biological fermentation. The chemical synthesis technology such as carbonylation and aldol condensation [3], etc., has been flourishing since 1950s, and is currently the main production method of isobutyl alcohol in the world. In recent years, with the advancement of science and technology as well as the development of society, the production of isobutyl alcohol by using genetically-modified microbes or metabolic engineering has received worldwide attention [4-6]. More importantly, researches have demonstrated that microbes can synthesize isobutyl alcohol using non-food crops such as cellulose, CO_2 and low protein. In future, non-grain production of isobutyl alcohol is expected to implement its formation on a large scale [7,8]. Atsumi et al. [5] used genetic engineering to knock out the genes that express byproducts during isobutyl alcohol synthesis pathway, which allows the highly efficient formation of isobutyl alcohol isobutyl alcohol with a 86% of the theoretical value. Li et al. [9] put forward an ultrasound-assisted route to enhance sugar utilization of cassawa starch as a raw material, thus improving the production yield of isobutyl alcohol. Wendy et al. [10] also employed genetic engineering to modify cellulose clostridium and C. cellulolyticum, as a result of which these engineered bacteria could directly convert cellulose into isobutyl alcohol and the isobutyl alcohol production can reach 660 mg/L in 8 days.

Therefore, in recent years, the further processing of isobutyl alcohol such as converting it into high value chemicals with a broader market prospect, has attracted much attention. Gevo, Inc of United States used isobutyl alcohol as crude material to produce high-value jet-range hydrocarbons through dehydration, oligomerization, and hydrogenation reactions [11]. The detailed processes are as follows: first, isobutyl alcohol is fixed into dehydration reactor and then dehydrates to isobutylene; after separating the water, the obtained isobutylene will generate high-carbon alkene in polymerization reactor, followed by hydrogenation of C_{8-16} alkenes to get jet fuels. These reaction processes are complex, and three-step reactions need to be carried out on three kinds of catalysts. Thus, recent developments of alcohol dehydration and alkene oligomerization over acidic zeolite have attracted much attention [12-15]. It should be noted that both isobutyl alcohol dehydration and isobutylene oligomerization can be catalyzed by acidic zeolite, providing a clue for combining both reactions to directly produce jet-range hydrocarbons through isobutyl alcohol oligomerization. Metal-organic frameworks (MOFs) and microporous layered silicate are kinds of new porous functional materials. Through the coordination of different organic ligands with metal centers, MOFs endowed with the functions are widely used in catalysis and many other fields [16]. Microporous layered silicate having the zeolite-like open microchannels within its layers, can exhibit excellent molecular recognition ability for the aromatic compounds via the microchannels, which is considered as excellent catalysts [17]. In the recent decade, periodic mesoporous organosilica (PMO) with aluminosilica realizes an ordered porous structure and wide variety of organic moiety, and its high surface area has been widely employed in the catalysts [18].

Beta, BEA type zeolite, with a three dimensional pore network including 12-MR pores has been widely used for various dehydration and oligomerization reactions, such as methanol to olefins (MTO) reaction [19,20] and alkene oligomerization reaction [21,22]. Herein, we conducted the isobutyl alcohol oligomerization reaction over zeolite Beta catalysts treated by various dealuminum or desilication methods to

compare the effectiveness of the catalysts in isobutyl alcohol oligomerization reaction, and to provide possible way to develop a promising catalyst. Besides, related factors of the zeolite catalyst such as acid site, pore structure, and pore size influencing reactive activity, were also studied via the utilization of XRD, SEM, XRF, Nitrogen adsorption-desorption, NH_3-TPD, Py-FTIR, and ^{27}Al-NMR. Especially, the reaction activity, C_{8-16} hydrocarbons selectivity and regenerability of the catalysts were discussed in detail.

2.2. Experimental

1.1 2.2.1. Preparation of the materials

Briefly, the commercial Beta zeolites (TOSOH) were mixed with 0.1 mol/L NH_4NO_3 aqueous solution and stirred at 80 $^{\circ}$C for 3 h. After filtration and washing with deionized water until no nitrate ions could be detected, and then the obtained products were dried at room temperature overnight, calcined at 550 $^{\circ}$C for 4 h. This proton-exchanged parent zeolite Beta was designated as BEA.

The zeolites H-Beta was treated by the HCl or the EDTA to dealuminate. The HCl treatment was carried out under stirring at 80 $^{\circ}$C in a 20 mL 1 mol/L HCl solution (2 g BEA) for 0.25, 0.5, 1, or 2 h. For EDTA treatment, the Beta were refluxed in 20 mL of distilled water with 0.96 g of H_4EDTA for a certain time (1, 2, 4 or 8 h). The mixture was heated to a specific temperature (at 100 $^{\circ}$C) with stirring. Respectively, the HCl treatment and EDTA of H-Beta zeolites are defined as HClxh-BEA and EDTAxh-BEA, in addition, for different treatment methods, x means the treatment time of the samples.

The desilicated process was achieved by NaOH treatment. 3 g of H-Beta were dispersed into 60 mL of NaOH solution (0.4 mol/L) at 65 $^{\circ}$C under stirring for 30 min. The slurry was filtered and then washed with deionized water and dried at 120 $^{\circ}$C. The obained sample was designated as NaOH-BEA.

2.2.2. Catalyst characterization

The XRD patterns of catalysts were analyzed by RINT 2400 System (Rigaku, Japan) with Cu-Kα radiation (λ=0.154 nm) at 40 kV and 20 mA. The scan was performed with a rate of 0.02°/s. The surface morphology was evaluated using a scanning electron microscopy (SEM, JEOL-JSM-6360). N_2 physisorption tests were carried out with a Quantachrome Instruments equipment (NOVA-2200e). Prior to tests, 30-40 mg samples were first degassed at 300 °C for 2 h. Afterward, the N_2 adsorption isotherms were recorded at -196 °C to obtain the surface area, pore volume and the average pore size according to the BJH method. And XRF analyses were used to determine the Si/Al of Beta zeolite by different treatment and performed on PHILIPS PW2404R.

The acidity of catalysts was studied with NH_3 temperature programmed desorption (TPD) using BELCAT-B-TT (BEL.JAPAN INC.). The NH_3-TPD was carried out between 50 °C and 900 °C under a helium flow (30 mL/min) with a heating rate of 10 °C/min. Before the test, the samples were pretreated under helium atmosphere at 500 °C for 1 h, then, cooled to 50 °C, and exposed to pure NH_3 (30 mL/min) for 0.5 h.

Pyridine adsorption (Py-FTIR) spectra were recorded with a Tensor 27 IR spectrometer from Bruker. The BEA, HCl2h-BEA, EDTA8h-BEA zeolite samples were directly pressed into thin wafers, which were mounted into a vacuum cell. Prior to the measurement, the sample cell was vacuumized to 10^{-2} Pa at 500 °C for 1h, the IR spectra were then recorded at 150 °C.

The ^{27}Al-MAS NMR spectra were registered using JNM-ECX 500 MHz (magnetic field is 11.7 T), equipped with a 4 mm probe at the spinning speed of 15 kHz. The pulse sequence contained one single excitation pulse of 1.2 μs (π/8) duration, the repeat time was 1 s.

The char/coke was analyzed through thermogravimetric analysis (DTA/TGA-60, Shimadzu). It was carried out in a METTLER TOLEDO STARe system, with the

heating rate of 10 °C/min under air atmosphere to identify the type of char and coke as well as to determine the total amounts of carbon deposition in the spent catalysts.

2.2.3. Catalytic testing

Isobutyl alcohol oligomerization reaction was carried out in an 85 mL steel batch reactor. In brief, 0.5 g of the catalyst and 10 ml of isobutyl alcohol (2-Methyl-1-Propanol, Tokyo Chemical Industry) were placed into the reactor. Then the reactor system was purged three times with N_2 to remove the trapped air. After purging, the reactor was pressurized with N_2 of 1 MPa, and then the reactor system was heated up to reaction temperature.

After reaction, the reactor was cooled down to the 0 °C and then depressurized to atmospheric pressure to collect the gas product. Liquid phase products were separated by filter. The liquid products were analyzed by a capillary chromatography (GC-14B, FID, Shimadzu, Japan). The gas products were also analyzed by another capillary chromatography (GC-14B, FID, Shimadzu, Japan). The filtered solid was then washed three times with n-hexane (100 mL, each time) and dried at 120 °C for 12 h for further analysis.

The conversion of isobutyl alcohol was calculated by its consumption:

Isobutyl alcohol conversion (%) = [1-($C_{mole\ of\ isobutyl\ alcohol\ after\ reaction}$)/($C_{mole\ of\ initial\ isobutyl\ alcohol}$)]*100%

The selectivity of component i was calculated with carbon molar base:

Sel. C_i = ($C_{mole\ of\ Ci\ hydrocarbon}/\sum_{i=1}^{n} C_{mole\ of\ Ci\ hydrocarbon}$) *100%

2.3. Results and Discussion

2.3.1. Structural and textural properties of catalysts

It can be seen from Figure 2.1 that XRD spectra of the Beta zeolite after treatment with hydrochloric acid, EDTA or NaOH still retain characteristic peaks at 7.4 and 22.4°, which can be attributed to typical crystal structure, indicating that hydrochloric acid, EDTA or NaOH treatment could not break the channel structure system of Beta-

zeolite zeolite. Moreover, the intensities of low angle peak and high angle peak increase significantly after dealumination treatment, which is due to the removal of impurities and extra-framework aluminum in zeolite after acid pickling, and then it improves the crystallinity of Beta zeolite obviously. But for HCl dealuminization, the crystallinity increases first and then decreases with the increase of dealumination time. This is because that dealuminization in high concentration of HCl for a long time removes a part of framework aluminum and breaks the internal structure, leading to defective lattice and lowered crystallinity [23]. In contrast, in the XRD spectra of Beta zeolite treated with strong alkali solution of NaOH, the intensities of absorption peaks at $2\theta=7.4^{o}$ are significantly reduced, which demonstrates that the structures of zeolite are partly destroyed after NaOH treatment [24].

Figure 2.2 gives SEM images of Beta zeolite under different treatment conditions. Regular stacked grains can be clearly seen in all zeolite samples. Some of Beta zeolite are flake, and few collapses occurs after treatment by NaOH solution, proving that strong alkali is corrosive to the crystal grains of zeolite. The alkali liquor dissolves Si in the zeolite framework and causes the zeolite framework to collapse. However, when the zeolite is treated with hydrochloric acid and EDTA solution, no damages can be found in the crystal grains. As the treatment time increases, the morphology of the zeolite has not changes. It suggests that hydrochloric acid and EDTA would modify the zeolite in a milder manner, which is also consistent with their XRD characterization results.

The Si/Al molar ratio of the Beta zeolite by different treatments was calculated by XRF and showed in Table 2.1. Thus, according to Table 2.1,we can estimate the dealumination degree on the zeolite. For HCl dealuminization, it has strong ability on dealumination process, and the Si/Al increases from 19.8 to 52.6. For the case of EDTA dealuminization, it modifies the zeolite in a milder manner, and the Si/Al was increased slightly from 19.8 to 37.8 [23].

The samples were characterized by nitrogen adsorption-desorption method. Figure 2.3 gives the nitrogen adsorption-desorption isotherms and corresponding BJH pore

size distribution curves of the samples under different treatment conditions, and the analysis data are also given in Table 2.1. In Figure 2.3, pristine Beta zeolite shows a large micropore volume. After dealuminization, the specific surface area and pore volume of Beta zeolite rise together. However, the pore size distribution shifts to big pore size after EDTA treatment. For the zeolite undergoing hydrochloric acid treatment, its pore size distribution shifts to left first and then shifts to right, along with increasing dealuminization time. As discussed above, EDTA dealuminization mainly removes the surface aluminum and amorphous aluminum, but it cannot get rid of framework aluminum completely [23]. Differently, hydrochloric acid dealuminization not only eliminates aluminum in the pores of zeolite and some amorphous impurities that block the pores, but also removes extra-framework aluminum. Therefore, some micropores with a certain amount of framework aluminum can be formed, which makes the channels more smooth. From Figure 2.3 and Table 2.1, it can be concluded that the specific surface area of Beta zeolite treated with NaOH is greatly reduced. Especially, the micropores numbers is significantly lowered because the strong alkali dissolves the silicon framework in the zeolite, leading to the structure collapse of zeolite [25]. These results are consistent with the above SEM and XRD characterizations, which proves that the employed NaOH solution is too strong to the modification of Beta zeolite.

2.3.2. ^{27}Al-solid-NMR characterization of catalysts

To better understand the detail of dealumination process, the Al species of Beta zeolite and the acid treated Beta zeolites were comparative investigated by ^{27}Al NMR. As shown in Figure 2.4, the peaks at 60 and 0 ppm can be ascribed to the tetrahedral framework Al (FAl) and octahedral extra-framework Al species (EFAl), respectively [26,27]. After treating by EDTA acid, the intensity of peak at 0 ppm decreases obviously. The ratio of EFAl/FAl changes from 0.18 to 0.1 after EDTA treatment, which indicates the non-framework Al are more easily to be eliminated than the framework Al during acid leaching process. However, it is interesting to note that the

intensity of EFAl is disappeared and the intensity of FAl decreases after HCl treatment (2 h). Therefore, the framework aluminum can be partly removed by HCl treatment [28].

2.3.3.   NH₃-TPD and Py-FTIR analysis of the catalysts

Figure 2.5 depicted the NH_3-TPD curves of H-beta zeolites prepared under different treatment conditions. NH_3 desorption peaks at around 220 °C and 350 °C can be attributed to the weak and strong acid sites, respectively. Compared with the parent zeolite, the acid strength of the BEA zeolites after EDTA or HCl treatment is decreased with the peak position shifts to lower temperature or peak intensity decreases, which can be attributed to the removal of the Al species in the zeolite channels [29]. The acidity of BEA zeolite undergoes tremendous change after NaOH treatment with strong acid sites even disappears due to the desilication process by the strong alkali solution.

The acid properties of BEA, HCl2h-BEA, and EDTA8h-BEA were further characterized by the in-situ pyridine-adsorption Fourier Transform infrared spectroscopy (py-FTIR) was shows in Figure 2.6. The typical peaks at 1540 and 1450 cm^{-1} are derived from the interactions of pyridine molecules with the Brønsted (B) and Lewis (L) acid sites, respectively. The characteristic peak at 1490 cm^{-1} can be attributed to the sum of Brønsted and Lewis acid sites. The amounts of Brønsted and Lewis acid sites can be further quantified based on the previous literature and the results are shown in the Table 2.2 [23]. Both of the B and L acid sites decreases after HCl or EDTA treatment compared with that of the parent BEA zeolite due to the extraction of framework and extra-framework Al species by acidic solution [30,31]. However, it should be noted that HCl treatment leads to the higher amount ratio of L to B acid sites, which is beneficial to the oligomerization reaction due to the synergistic effect between the L and B acid sites [23].

2.3.4. Catalytic performance of the catalysts in isobutyl alcohol oligomerization

The conversion of isobutyl alcohol catalyzed over Beta zeolite catalyst and the distribution of olefin products were shown in Figure 2.7. It is clear that the conversion of isobutyl alcohol over the modified Beta zeolite dealuminated with respective HCl or EDTA is higher than that of original Beta zeolite. Meanwhile, the conversion of isobutyl alcohol increases with an augment of dealumination time. When the Beta zeolite is dealuminated with HCl for 2h, the conversion of isobutyl alcohol is up to 98%, much higher than that of 75% over original Beta zeolite. However, as Beta zeolite treated by NaOH, the conversion of isobutyl alcohol decreases markedly. As for the produced $C_4^=$, the selectivity is the opposite tendency as that of isobutyl alcohol conversion. As depicted in Figure 2.8, C_4 is the primary isobutylene which is formed from isobutyl alcohol dehydration, and C_{8-16} mainly composes of isobutylene dimer, trimer and tetramer. For isobutyl alcohol oligomerization over Beta zeolite, the pore openings of Beta zeolite as well as molecular size of reactants play critical role in the selectivity of products listed in Table 2.3, which is mainly attributed to the shape-selectivity function of zeolite. By dealumination of Beta zeolite with HCl or EDTA, the selectivity of C_{8-16} is increased. This may be due to a fact that the impurities and the part of aluminum ions on zeolite skeleton and extra framework on Beta zeolite are effectively removed by dealuminated treatment, enlarging the pore size of Beta zeolite and then enhancing the diffusion ability of products. By comparison, the C_{8-16} selectivity over NaOH-treated Beta zeolite is also obtained, and the C_{8-16} selectivity is negligible. The result indicates that the acidity of Beta zeolite is responsible for the oligomerization of isobutyl alcohol.

In order to further investigate isobutyl alcohol oligomerization reaction, the hydrocarbons distribution of C_{8-16} over BEA, HCl (2 h) or EDTA (8 h)-treated Beta zeolite was presented in Figure 2.8. For BEA catalyst, the products are primary C_{8-12}, which mainly originates from the cracking of hydrocarbon with large molecule. However, with regard to HCl (2 h) or EDTA (8 h)-treated Beta zeolite, the products distribution shifts to heavy hydrocarbon. It is worth noting that the HCl (2 h) -treated Beta zeolite presents more obvious deviation. This could be explained that both

reactions of the isobutyl alcohol dehydration and the isobutylene oligomerization are based on the mechanism of carbonium ions in isobutyl alcohol oligomerization shown in Figure 2.9 [32-34]. Brønsted acid is generally deemed as the active center of cracking reaction, large amounts of the Brønsted acid may increase the formation of carbon deposits which will block the acidic site of catalyst and result in the deactivation of catalyst [35], and Lewis acid acts as the active center for isobutylene oligomerization. Although the total acid content greatly reduced after HCl treatment with 2 h, the ratio of Lewis acid to Brønsted acid increased due to the removal of extra-framework aluminum and partial framework aluminum on Beta zeolite, thus promoting the reaction to proceed towards oligomerization. Simultaneously, the oligomerization of isobutylene consumed carbonium ions and thus promoted the dehydration of isobutyl alcohol. All of these factors contributed to the excellent catalytic activity of the Beta zeolite treated with HCl (2 h). Furthermore, Brønsted acid is generally deemed as the active center of cracking reaction, and the relatively weak acid sites on HCl (2 h)-treated Beta zeolite resulted in less products of isobutylene pyrolysis, which consists of C_8, C_{12} and C_{16} mainly.

The carbon balance of the experiment employing catalysts by different treatment is listed in Table 2.4. As we can see, it is clear that the carbon balance over the modified Beta zeolite dealuminated with respective HCl or EDTA is better than those over original Beta zeolite.

To explain the coke formed during the reaction, TG/DTA was used to analyze the spent catalysts. The results of spent catalysts by different treatments are illustrated in Figure 2.10, which can provide information on the coke weight of spent catalyst. Obviously, the endothermic peak between 400 °C and 600 °C was decreased after the HCl or EDTA treatment. A possible explanation is that Brønsted acid was decreased by the acid treatment, suppressing the formation of carbon deposits [35]. And the pore size and the pore opening were increased due to the removal of impurities and extra-framework aluminum in zeolite after acid pickling. Consequently the catalysts by acid treatment formed less hard coke. On the other hand, the main weight loss of

HCl2h-BEA and EDTA8h-BEA occurred below 200 ℃, which might be ascribed to the water in the catalysts. Meanwhile, the carbon balance of HCl2h-BEA and EDTA8h-BEA is better than those of other catalysts.

The effect of reaction time on isobutyl alcohol oligomerization over HCl2h-BEA is depicted in Figure 2.11. Apparently, the isobutyl alcohol conversion increased rapidly from 30% to 74% at first 2 h of reaction and then approached to the maximum with continuous increased reaction time, reaching 98% at 4h. As shown in Figure 2.11b, the selectivity of oligomeric products(C_{8-16}) displays the similar trend with isobutyl alcohol conversion, which reaches the maximum at 4 h but then decreases slightly after 6h. The slight decrease of C_{8-16} selectivity could be attributed to the increase of the by-products (C_{5-7} and C_{16}^{+}) with prolonged reaction time. The $C_4^{=}$ selectivity presents almost opposite trend with isobutyl alcohol conversion and C_{8-16} selectivity. It is because that this reaction system discussed here mainly involved two reactions (isobutyl alcohol dehydration and isobutylene oligomerization), and both reactions could occur at same acid sites of catalyst successively. The isobutyl alcohol is first dehydrated to produce isobutylene and then isobutylene is oligomerized to oligomeric C_{8-16} products. However, by prolonging the reaction time, about 20% $C_4^{=}$ still exists and could not be converted completely, which maybe because that the generated C_{16}^{+} products blocked the acid site of HCl2h-BEA catalyst and led to deactivation of catalyst.

However, this process is promising as a new way to produce jet fuels with the potential to be an industrialization technology, so, the regeneration of the catalysts would be important. In order to investigate the regenerability of cataytlys, the spent HCl2h-BEA after 8 h of reaction is calcined in the air at 600 ℃ for 6h, and the catalytic performance of the regenerated catalyst was shown in Figure 2.12. It is obvious that the calcined HCl2h-BEA fully recovered the catalytic performances and the conversion and C_{8-16} selectivity is very similar to those of the fresh catalyst. It is probably because that although some oligomeric products adsorbed strongly on active acid sites or the generated C_{16}^{+} products blocked the channels of zeolite, which

leads to deactivation of the catalyst, they does not destroy the pore structure and active site of beta zeolite. Therefore, the regeneration of this catalyst is easily, which make the HCl2h-BEA catalyst as an attractively potential catalyst for isobutyl alcohol oligomerization.

2.4. Conclusions

In this paper, we used various dealuminization methods, with HCl and EDTA as acids, to treat zeolite, by which to effectively adjust the pore structure and acidity of Beta zeolite. With the obtained zeolite as catalysts, we also investigated their catalytic performance for isobutyl alcohol oligomerization to synthesize jet fuels. Although undergoing dealumination processes, the Beta zeolite still remains its integrated channels and framework. The employed dealumination process could effectively remove the extra-framework aluminum and impurities. As a result, the pores of zeolite samples become smoother, by which to further improve their catalytic activity. Due to the dealumination process, the total acidic sites and the number of Brønsted acid sites on zeolite were reduced to some extent. However, the increased ratio of Lewis/Brønsted acidic sites was available for promoting the oligomerization reaction step to form jet fuels. Meanwhile, the promoted oligomerization reaction step also facilitated the dehydration reaction step of isobutyl alcohol. Among the tested catalysts, the HCL2h-BEA catalyst exhibited the highest conversion of 98% and the highest C_{8-16} selectivity of 59%. In addition, after removing the carbon deposit on this HCL2h-BEA catalyst by calcination, this spent catalyst also given similar catalytic performance to its fresh one.

References

[1] X. Wang, G. Yang, J. Zhang, S. Chen, Y. Wu, Q. Zhang, J. Wang, Y. Han, Y. Tan, Synthesis of isoalkanes over a core (Fe-Zn-Zr)-shell (zeolite) catalyst by CO_2 hydrogenation, Chem. Commun. 52 (2016) 7352–7355. doi:10.1039/c6cc01965j.

[2] R.C. Saxena, D.K. Adhikari, H.B. Goyal, Biomass-based energy fuel through biochemical routes: A review, Renew. Sustain. Energy Rev. 13 (2009) 167–178. doi:10.1016/j.rser.2007.07.011.

[3] E.J. Steen, Y. Kang, G. Bokinsky, Z. Hu, A. Schirmer, A. McClure, S.B. Del Cardayre, J.D. Keasling, Microbial production of fatty-acid-derived fuels and chemicals from plant biomass, Nature. 463 (2010) 559 – 562. doi:10.1038/nature08721.

[4] S. Atsumi, W. Higashide, J.C. Liao, Direct photosynthetic recycling of carbon dioxide to isobutyraldehyde, Nat. Biotechnol. 27 (2009) 1177 – 1180.doi:10.1038/nbt.1586.

[5] S. Atsumi, T. Hanai, J.C. Liao, Non-fermentative pathways for synthesis of branched-chain higher alcohols as biofuels, Nature. 451 (2008) 86 – 89. doi:10.1038/nature06450.

[6] C. Dellomonaco, J.M. Clomburg, E.N. Miller, R. Gonzalez, Engineered reversal of the β-oxidation cycle for the synthesis of fuels and chemicals, Nature. 476 (2011) 355–359. doi:10.1038/nature10333.

[7] R.C. Saxena, D.K. Adhikari, H.B. Goyal, Biomass-based energy fuel through biochemical routes: A review, Renew. Sustain. Energy Rev. 13 (2009) 167–178. doi:10.1016/j.rser.2007.07.011.

[8] E.I. Lan, J.C. Liao, Microbial synthesis of n-butanol, isobutanol, and other higher alcohols from diverse resources, Bioresour. Technol. 135 (2013) 339 – 349. doi:10.1016/j.biortech.2012.09.104.

[9] S. Wang, Y. Chen, H. Liang, Y. Chen, M. Shi, J. Wu, X. Liu, Z. Li, B. Liu, Q. Yuan, Y. Li, Intestine-Specific Delivery of Hydrophobic Bioactives from Oxidized Starch Microspheres with an Enhanced Stability, J. Agric. Food Chem. 63 (2015) 8669–8675. doi:10.1021/acs.jafc.5b03575.

[10] W. Higashide, Y. Li, Y. Yang, J.C. Liao, Metabolic engineering of Clostridium cellulolyticum for production of isobutanol from cellulose, Appl. Environ. Microbiol. 77 (2011) 2727–2733. doi:10.1128/AEM.02454-10.

[11] I.L. Us, M.J. Mccall, METHODS AND SYSTEMS FOR PRODUCING JET - RANGE HYDROCARBONS, 2 (2018).US Patent No.: US9862655B2

[12] P.L. Benito, A.G. Gayubo, A.T. Aguayo, M. Olazar, J. Bilbao, Effect of Si/Al Ratio and of Acidity of H-ZSM5 Zeolites on the Primary Products of Methanol to Gasoline Conversion, J. Chem. Technol. Biotechnol. 66 (1996) 183 – 191. doi:10.1002/(sici)1097-4660(199606)66:2<183::aid-jctb487>3.3.co;2-b.

[13] A.N. Mlinar, P.M. Zimmerman, F.E. Celik, M. Head-Gordon, A.T. Bell, Effects of Brønsted-acid site proximity on the oligomerization of propene in H-MFI, J. Catal. 288 (2012) 65–73.   doi:10.1016/j.jcat.2012.01.002.

[14] K.K. Ramasamy, Y. Wang, Catalyst activity comparison of alcohols over zeolites, J. Energy Chem. 22 (2013) 65–71. doi:10.1016/S2095-4956(13)60008-X.

[15] U. V. Mentzel, S. Shunmugavel, S.L. Hruby, C.H. Christensen, M.S. Holm, High yield of liquid range olefins obtained by converting i-propanol over zeolite H-ZSM-5, J. Am. Chem. Soc. 131 (2009) 17009–17013. doi:10.1021/ja907692t.

[16] P. Panahi, N. Nouruzi, E. Doustkhah, H. Mohtasham, A. Ahadi, A. Ghiasi-Moaser, S. Rostamnia, G. Mahmoudi, A. Khataee, Zirconium based porous coordination polymer (PCP) bearing organocatalytic ligand: A promising dual catalytic center for ultrasonic heterocycle synthesis, Ultrason. Sonochem. 58 (2019). https://doi.org/10.1016/j.ultsonch.2019.104653.

[17] E. Doustkhah, Y. Ide, Bursting Exfoliation of a Microporous Layered Silicate to Three-Dimensionally Meso-Microporous Nanosheets for Improved Molecular Recognition, ACS Appl. Nano Mater. 2 (2019) 7513–7520. https://doi.org/10.1021/acsanm.9b01508.

[18] E. Doustkhah, H. Mohtasham, M. Hasani, Y. Ide, S. Rostamnia, N. Tsunoji, M. Hussein, Merging periodic mesoporous organosilica (PMO) with mesoporous aluminosilica (Al/Si-PMO): A catalyst for green oxidation, Mol. Catal. 482 (2020). https://doi.org/10.1016/j.mcat.2019.110676.

[19] P. Tian, Y. Wei, M. Ye, Z. Liu, Methanol to olefins (MTO): From fundamentals to commercialization, ACS Catal. 5 (2015) 1922 – 1938. doi:10.1021/acscatal.5b00007.

[20] M. Yoshioka, T. Yokoi, T. Tatsumi, Development of the CON-type Aluminosilicate Zeolite and Its Catalytic Application for the MTO Reaction, ACS Catal. 5 (2015) 4268–4275. doi:10.1021/acscatal.5b00692.

[21] J.W. Yoon, J.S. Chang, H. Du Lee, T.J. Kim, S.H. Jhung, Trimerization of isobutene over a zeolite beta catalyst, J. Catal. 245 (2007) 253 – 256. doi:10.1016/j.jcat.2006.10.008.

[22] M. Torres, M. Gutiérrez, V. Mugica, M. Romero, L. López, Oligomerization of isobutene with a beta-zeolite membrane: Effect of the acid properties of the catalytic membrane, Catal. Today. 166 (2011) 205–20. doi:10.1016/j.cattod.2010.08.002.

[23] A. Gola, B. Rebours, E. Milazzo, J. Lynch, E. Benazzi, S. Lacombe, L. Delevoye, C. Fernandez, Effect of leaching agent in the dealumination of stabilized Y zeolites, Microporous Mesoporous Mater. 40 (2000) 73 – 83. doi:10.1016/S1387-1811(00)00243-2.

[24] M. Bjørgen, F. Joensen, M. Spangsberg Holm, U. Olsbye, K.P. Lillerud, S. Svelle, Methanol to gasoline over zeolite H-ZSM-5: Improved catalyst performance by

treatment with NaOH, Appl. Catal. A Gen. 345 (2008) 43 − 50. doi:10.1016/j.apcata.2008.04.020.

[25] Y. Wu, F. Tian, J. Liu, D. Song, C. Jia, Y. Chen, Enhanced catalytic isomerization of α-pinene over mesoporous zeolite beta of low Si/Al ratio by NaOH treatment, Microporous Mesoporous Mater. 162 (2012) 168 − 174. doi:10.1016/j.micromeso.2012.06.027.

[26] F. Yi, Y. Chen, Z. Tao, C. Hu, X. Yi, A. Zheng, X. Wen, Y. Yun, Y. Yang, Y. Li, Origin of weak Lewis acids on silanol nests in dealuminated zeolite Beta, J. Catal. (2019). doi:10.1016/j.jcat.2019.10.008.

[27] D. Yuan, C. Kang, W. Wang, H. Li, X. Zhu, Y. Wang, X. Gao, B. Wang, H. Zhao, C. Liu, B. Shen, Creation of mesostructured hollow Y zeolite by selective demetallation of an artificial heterogeneous Al distributed zeolite crystal, Catal. Sci. Technol. 6 (2016) 8364−8374. doi:10.1039/c6cy01841f.

[28] C.S. Triantafillidis, A.G. Vlessidis, L. Nalbandian, N.P. Evmiridis, Effect of the degree and type of the dealumination method on the structural, compositional and acidic characteristics of H-ZSM-5 zeolites, Microporous Mesoporous Mater. 47 (2001) 369−388.   doi:10.1016/S1387-1811(01)00399-7.

[29] A.B. Halgeri, J. Das, Novel catalytic aspects of beta zeolite for alkyl aromatics transformation, Appl. Catal. A Gen. 181 (1999) 347−354. doi:10.1016/S0926-860X(98)00395-0.

[30] G. Busca, Acid catalysts in industrial hydrocarbon chemistry, Chem. Rev. 107 (2007) 5366−5410. doi:10.1021/cr068042e.

[31] A.A. Gabrienko, S.S. Arzumanov, A. V. Toktarev, A.G. Stepanov, Solid-state NMR characterization of the structure of intermediates formed from olefins on metal oxides (Al_2O_3 and Ga_2O_3), J. Phys. Chem. C. 116 (2012) 21430−21438. doi:10.1021/jp3071103.

[32] J.N. Kondo, K. Domen, IR observation of adsorption and reactions of olefins on H-form zeolites, J. Mol. Catal. A Chem. 199 (2003) 27–38. doi:10.1016/S1381-1169(03)00015-3.

[33] R. Alcántara, E. Alcántara, L. Canoira, M.J. Franco, M. Herrera, A. Navarro, Trimerization of isobutene over Amberlyst-15 catalyst, React. Funct. Polym. 45 (2000) 19–27. doi:10.1016/S1381-5148(00)00004-3.

[34] T.K. Phung, L. Proietti Hernández, A. Lagazzo, G. Busca, Dehydration of ethanol over zeolites, silica alumina and alumina: Lewis acidity, Brønsted acidity and confinement effects, Appl. Catal. A Gen. 493 (2015) 77 – 89. doi:10.1016/j.apcata.2014.12.047.

[35] T. V. Choudhary, A. Kinage, S. Banerjee, V.R. Choudhary, Influence of Si/Ga and Si/Al ratios on propane aromatization over highly active H-GaAlMFI, Catal. Commun. 7 (2006) 166–169. https://doi.org/10.1016/j.catcom.2005.10.006.

Tables and Figures

Table 2.1. Physical properties of the Beta zeolite by different treatments.

Catalysts	Si/Al*	Surface Area (m²/g)			Pore Volume (cm³/g)		
		Total	Micropore	External	Total	Micropore	External
BEA	19.8	512.1	445.0	67.1	0.324	0.261	0.063
NaOH-BEA	8.4	308.2	167.5	140.7	0.392	0.104	0.288
HCl0.25h-BEA	22.9	525.8	467.7	58.1	0.351	0.276	0.075
HCl0.5h-BEA	31.4	576.7	501.6	75.1	0.374	0.298	0.076
HCl1h-BEA	37.8	627.9	529.0	98.9	0.443	0.317	0.126
HCl2h-BEA	52.6	708.7	575.9	132.8	0.475	0.343	0.132
EDTA1h-BEA	23.5	697.6	594.4	103.2	0.499	0.341	0.158
EDTA2h-BEA	26.4	765.1	647.6	117.5	0.581	0.367	0.214
EDTA4h-BEA	35.9	807.6	682.1	125.5	0.565	0.385	0.180
EDTA8h-BEA	37.8	816.9	661.0	155.9	0.607	0.374	0.232

*Si/Al was calculated by XRF.

Table 2.2. Lewis and Brønsted acid sites as well as L/B ratio determined by FTIR of adsorbed pyridine (Py).

Sample	Acid sites (µmol/g)		L/B
	Lewis	Brønsted	
BEA	2.651	3.517	0.75
HCl2h-BEA	0.695	0.451	1.51
EDTA8h-BEA	0.626	1.165	0.54

Notes: (Lewis acid sites determined from the IR band at 1455 cm^{-1} and Brønsted acid sites from the one at 1546 cm^{-1}).

Table 2.3. The molecular size of reactants, and pore openings of Beta zeolite.

isobutyl alcohol	isobutylene	diisobutylene	triisobutylene	tetraisobutylene	Beta
0.53×0.42nm	0.42×0.42nm	0.75×0.44nm	0.83×0.51nm	0.96×0.63nm	0.68nm

Table 2.4. The carbon balance of experiment over the Beta zeolite by different treatments.

Catalysts	BEA	EDTA1h -BEA	EDTA2h -BEA	EDTA4h -BEA	EDTA8h -BEA	HCl0.25h -BEA	HCl0.5h -BEA	HCl1h -BEA	HCl2h -BEA
Carbon balance	78%	81%	83%	82%	84%	80%	83%	85%	89%
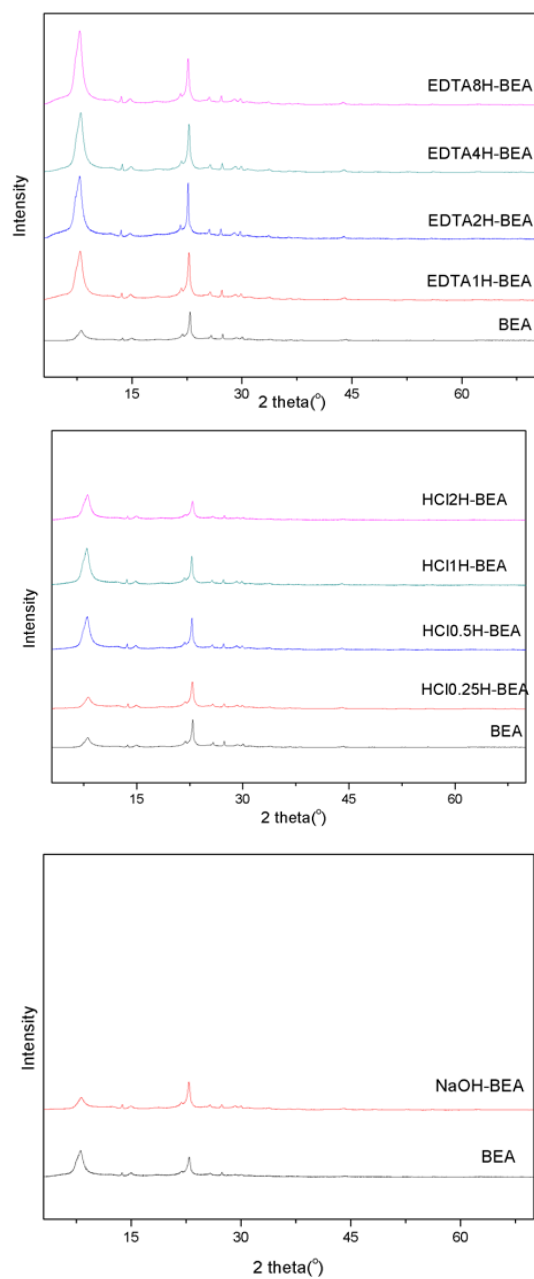
**Figure 2.1. XRD patterns of the Beta zeolite with different treatments.**
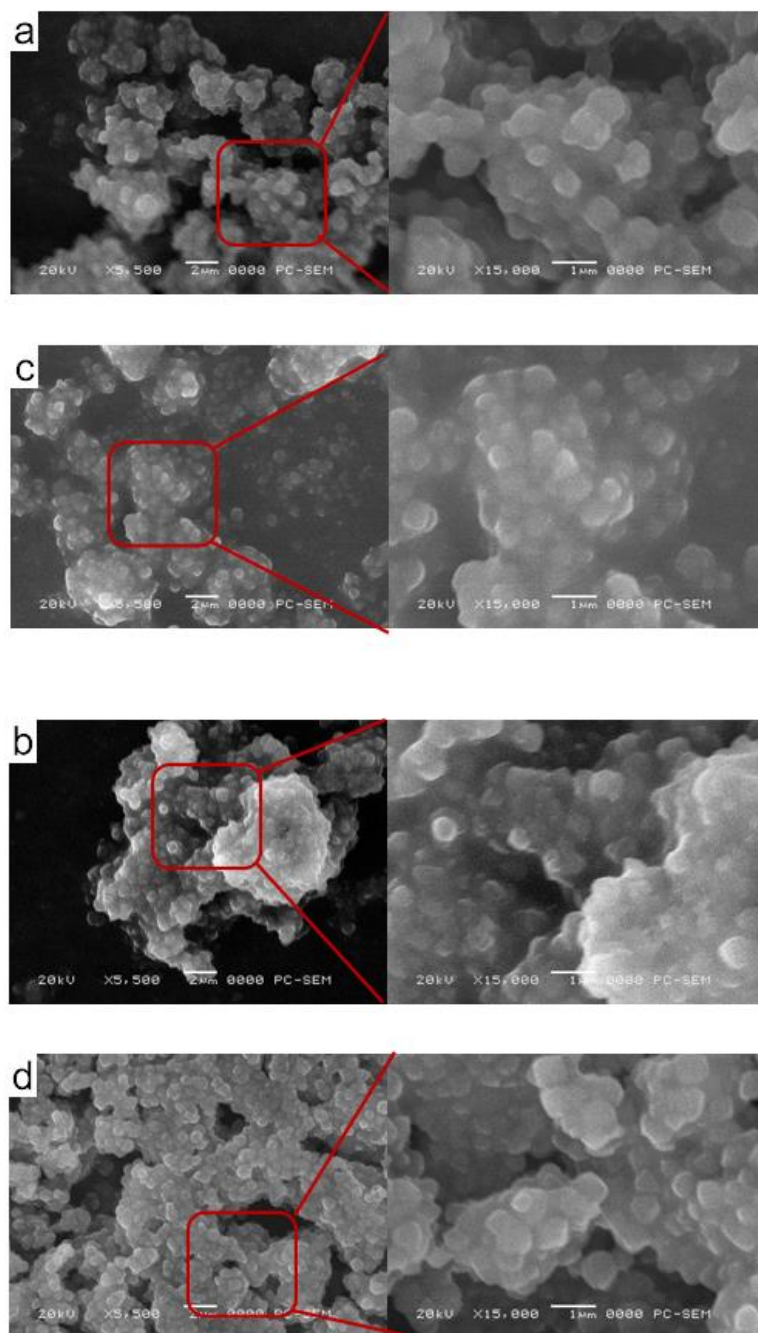
Figure 2.2. The surface morphologies of the Beta zeolite by different treatments. (a:BEA; b: NaOH-BEA; c: HCl2h-BEA; d: EDTA8h-BEA.)
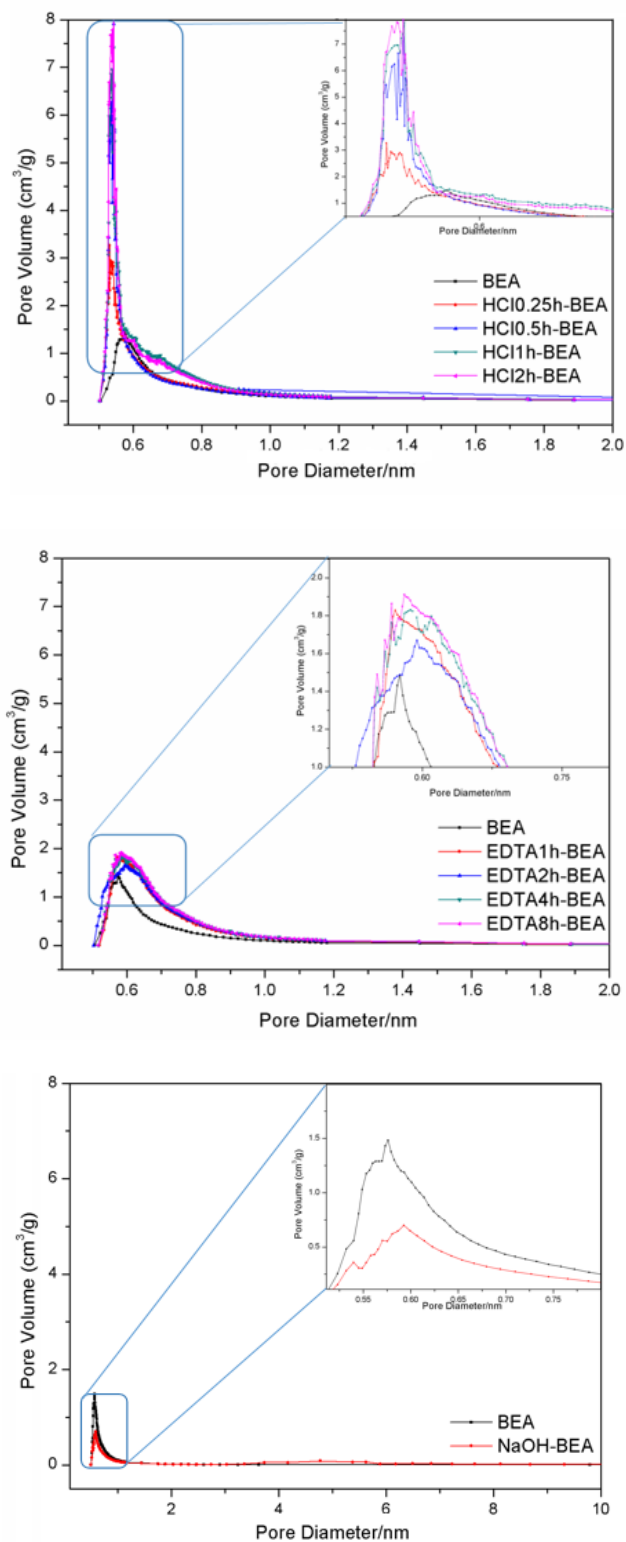
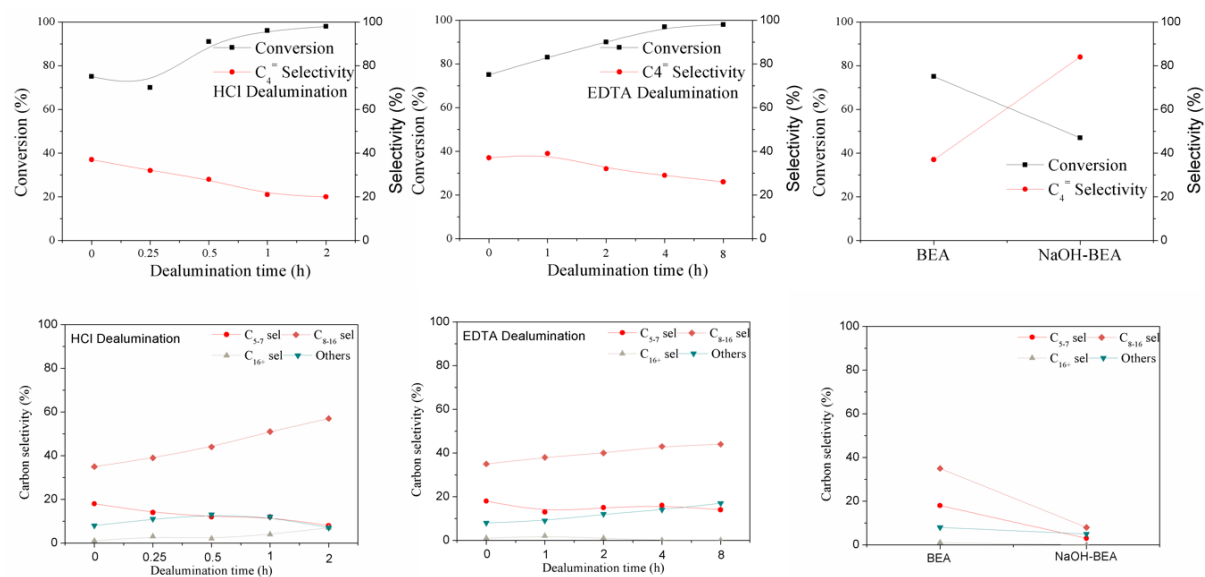**Figure 2.3. Pore size distribution of the Beta zeolite by different treatments.**
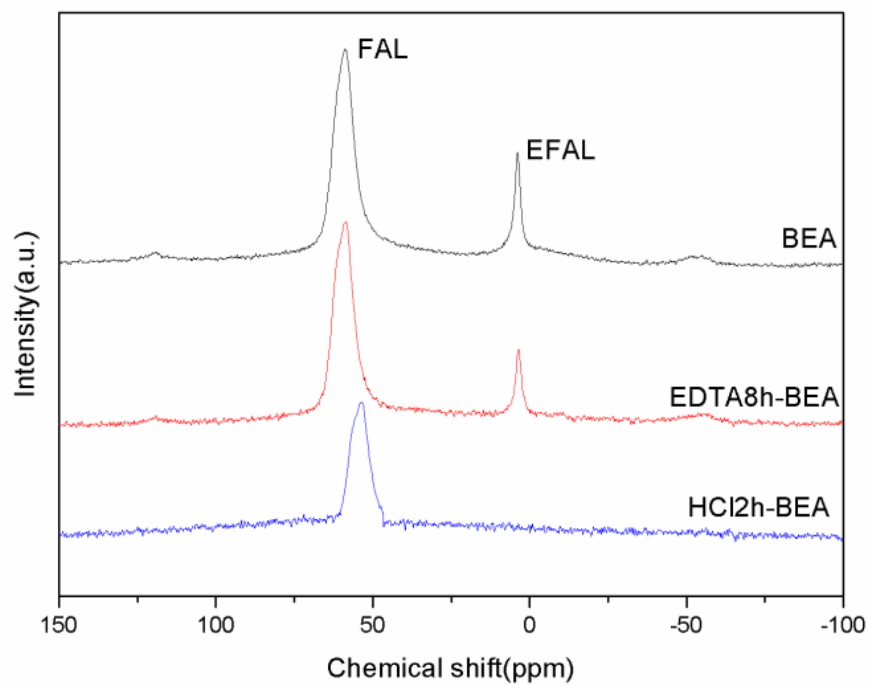
Figure 2.4. ^{27}Al-NMR spectra of the fresh Beta zeolite and the Beta zeolites after acid treatment. (EDTA and HCl)
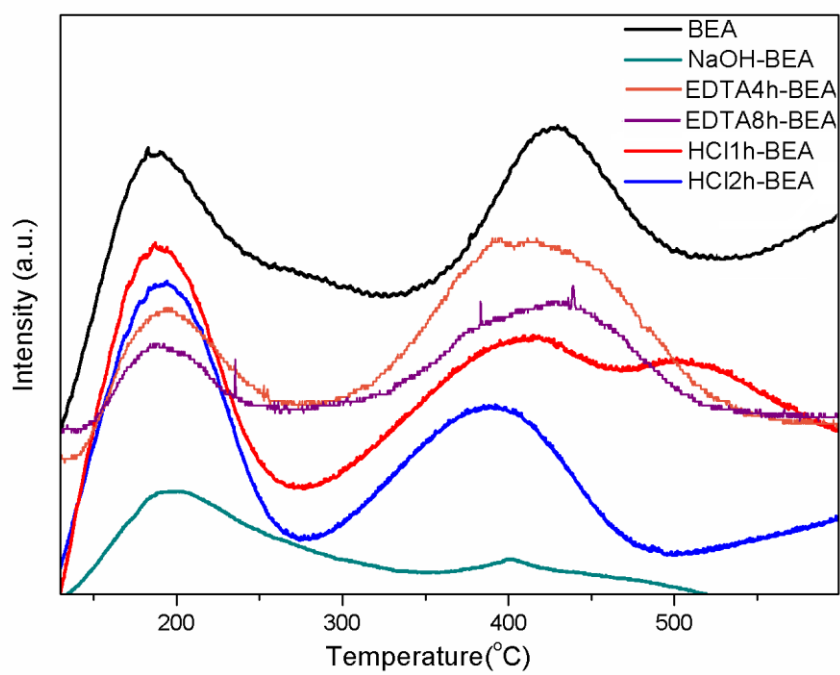
Figure 2.5. NH₃-TPD profiles of the beta zeolites prepared under different treatment conditions.
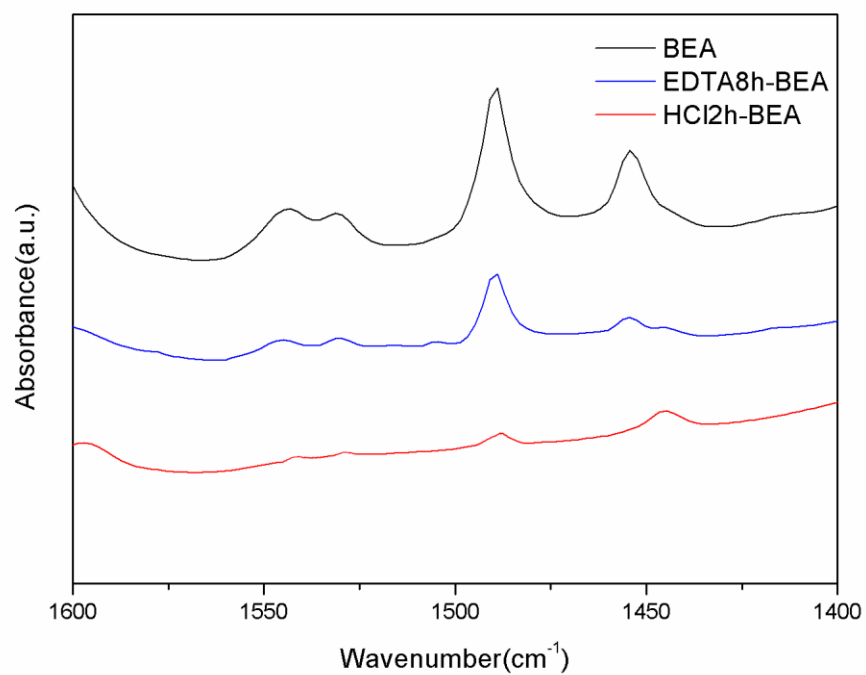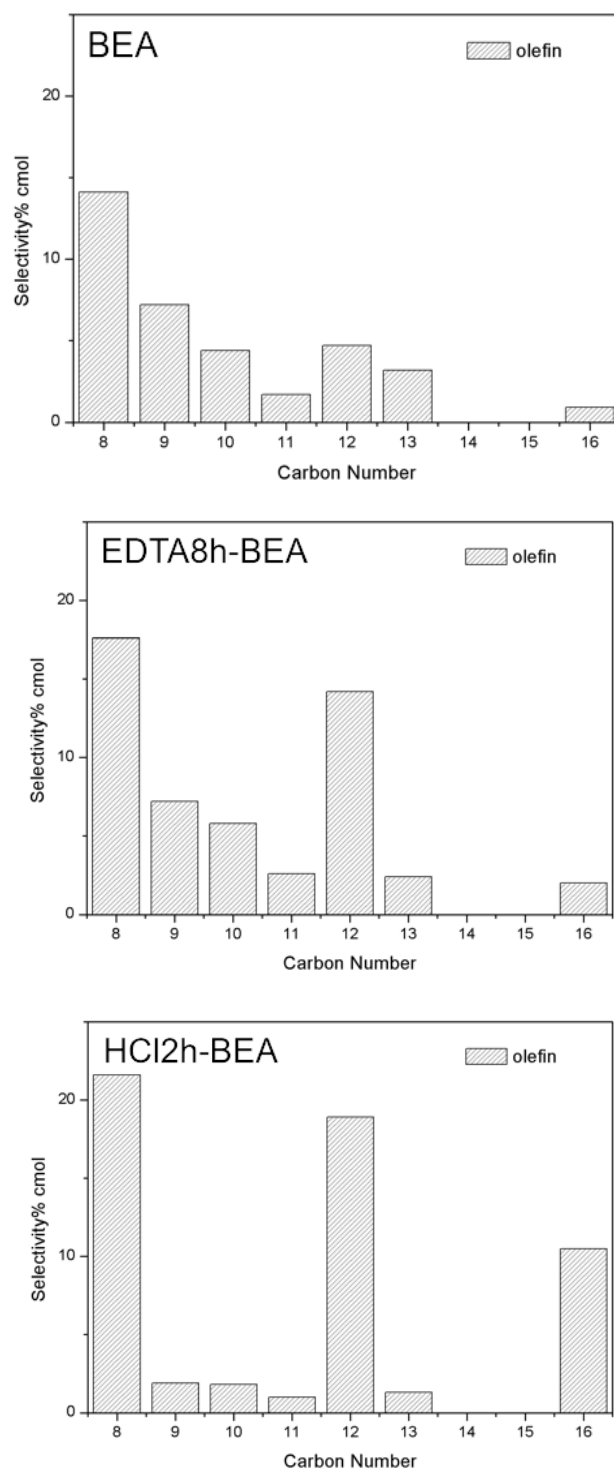
Figure 2.6. Py-FTIR of of the beta zeolite by different treatments.

Figure 2.7. Catalytic performance of the catalysts in isobutyl alcohol oligomerization. (Reaction condition: 10 ml isobutyl alcohol; 0.5 g catalysts; 1.0 MPa N_2; Reaction temperature: 240 ^{o}C; Reaction time: 4 h;)

Figure 2.8. The hydrocarbon distribution in C$_{8\text{-}16}$ over the Beta zeolite by different treatments.
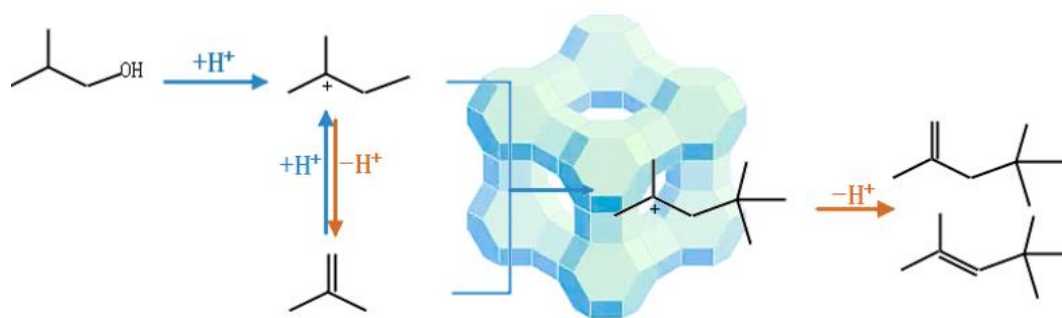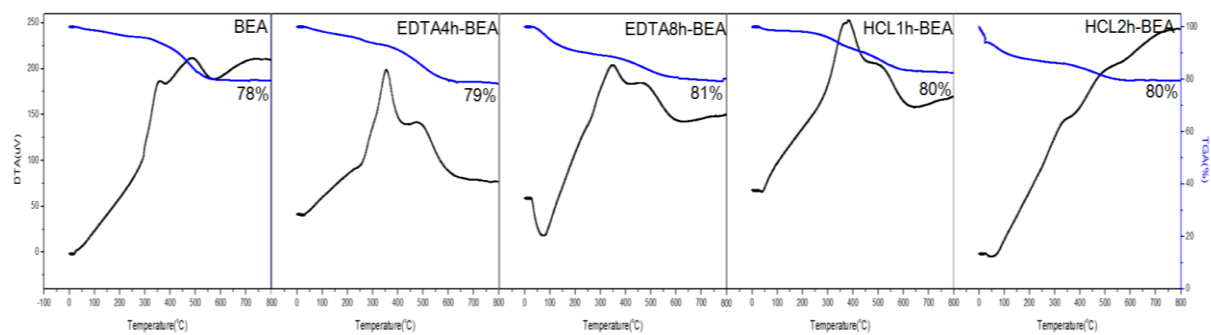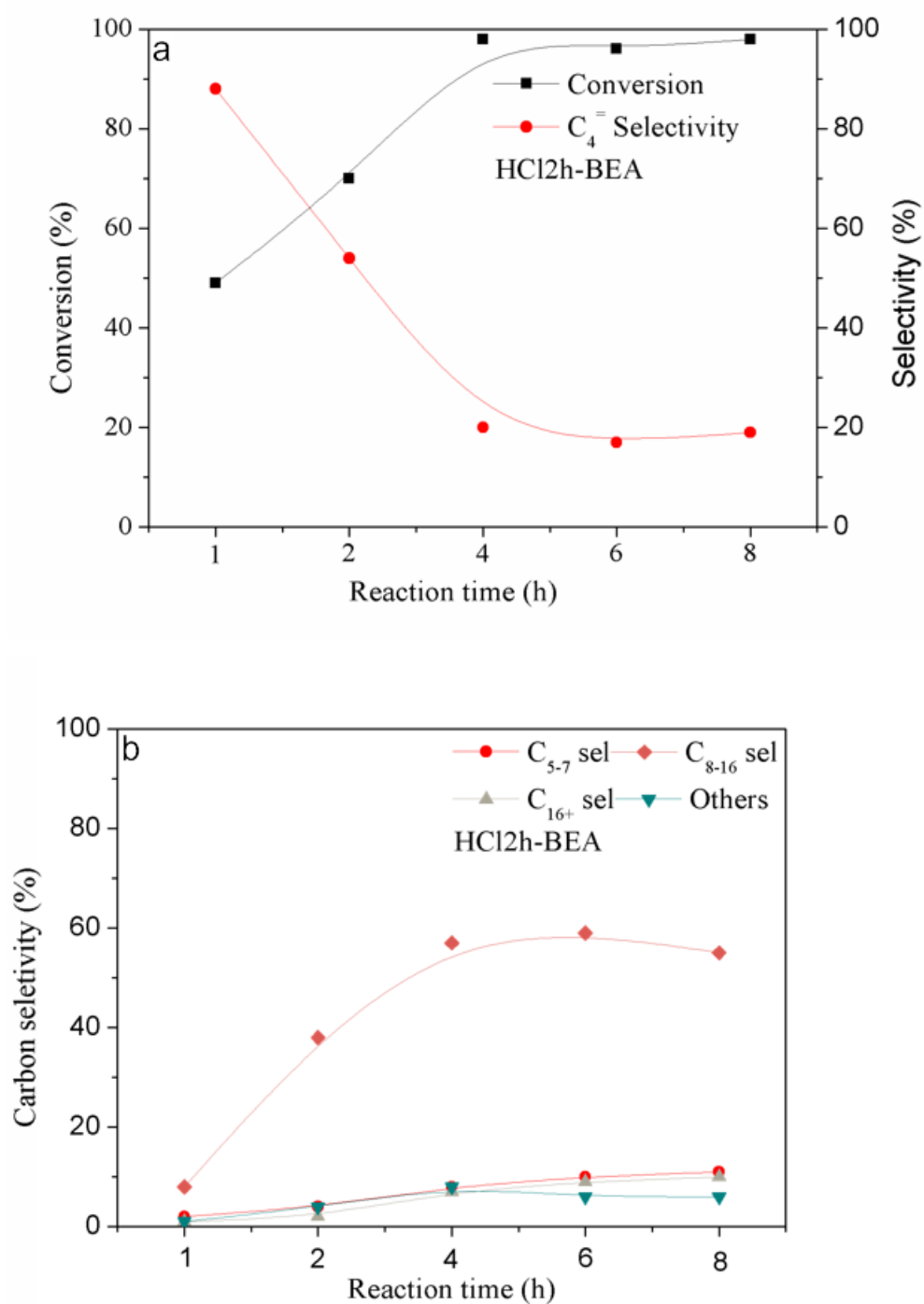
Figure 2.9. Mechanism of carbonium ions in isobutyl alcohol oligomerization.

Figure 2.10. The TG/DTA result of the spent catalysts. (Inserted number stands for the final weight left)

**Figure 2.11. The effect of reaction time on isobutyl alcohol oligomerization over HCl2h-BEA.** (Reaction condition: 10 mL isobutyl alcohol; 0.5 g catalysts; 1.0 MPa N_2; Reaction temperature: 240 ºC)
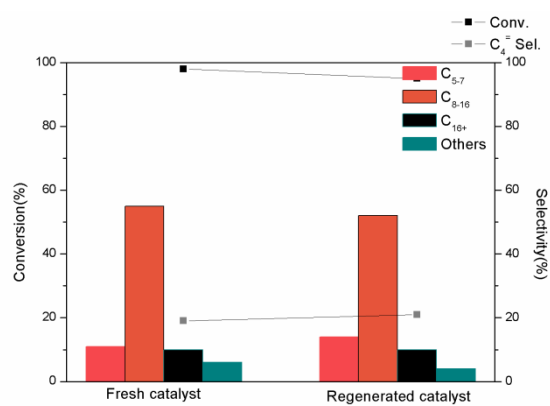
Figure 2.12. Catalytic performance of regenerated HCl2h-BEA in 8 h. (Reaction condition: 10 mL isobutyl alcohol; 0.5 g catalysts; 1.0 MPa N_2; Reaction temperature: 240 ^{o}C; Reaction time: 8 h;)

Chapter 3

Direct Conversion of CO_2 to Aromatics with High Yield via

a Modified Fischer-Tropsch Synthesis Pathway
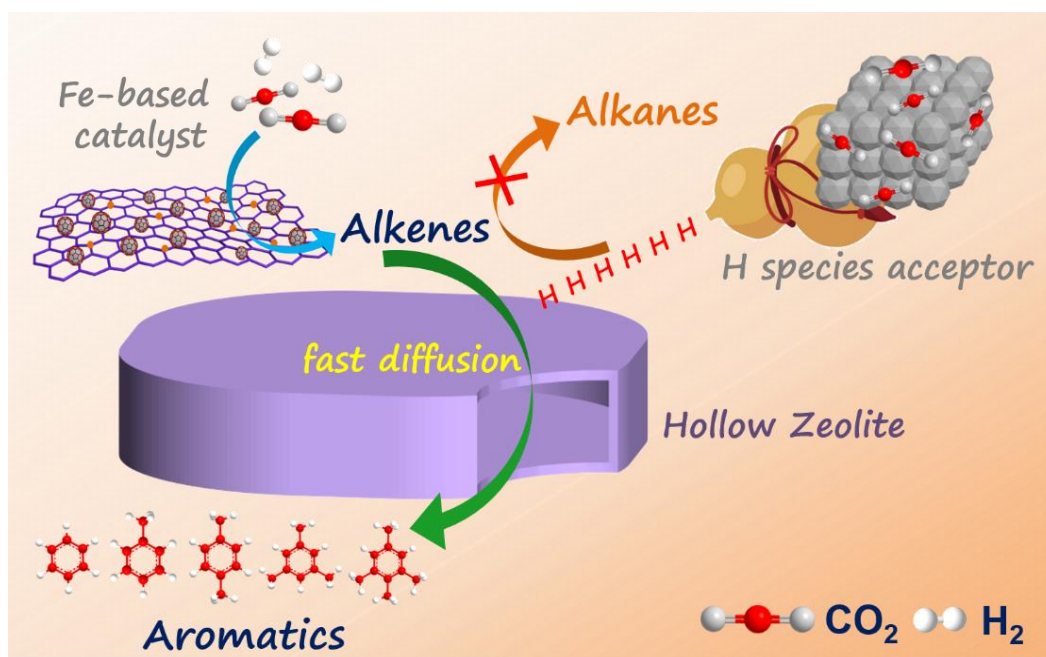
Abstract

The direct conversion of CO_2 to aromatics not only reduces carbon emissions but also provides an alternative way for value-added chemicals synthesis. Even though the hydrogenation of CO_2 to aromatics has been realized via a methanol-mediated pathway or a modified Fischer-Tropsch synthesis route, low yield of aromatics is still the bottleneck of this strategy. Here, we develop a multifunctional catalyst composed of Na modified Fe-based catalyst and hollow acidic zeolite H-ZSM-5 to catalyze the hydrogenation of CO_2 to aromatics by single pass. Na modified Fe-based catalyst prepared by pyrolysis of Fe-based metal-organic frameworks (Fe-MOFs) can boost the formation of alkenes intermediates because of its high active sites accessibility and precisely tailored catalytic interfaces. Thereafter, the produced alkenes can be converted to aromatics via the dehydrogenation and cyclization reactions when they diffuse to the acid sites of H-ZSM-5. The hollow H-ZSM-5 with short diffusional channels, appropriate density and strength of acid sites guaranteed the high yield of aromatics (203.8 g_{CH2} kg_{cat}^{-1} h^{-1}). Furthermore, the driving force in the tandem process can be attributed to the cooperative interplay between the multifunctional catalysts. The CO_2 adsorbed on Fe-based catalyst can be employed as acceptors for H species produced from the dehydrogenation and cyclization reactions, thereby increasing the yield of aromatics by shifting the chemical thermodynamic equilibrium.

Keywords: Methane conversion; Methanol; Pd-Au nanoparticles; Carbon materials

3.1. Introduction

The ever-increasing CO_2 emissions into the atmosphere along with rapid growth of the economy has placed a huge burden on the environment, such as global warming, ocean acidification, climate change, etc.[1] The transformation of CO_2 back into high-value-added chemicals is a promising strategy that not only reduces the carbon emissions but also meets the demand of sustainable development.[2] Despite more and more attention has been paid on the photo- and electro-driven CO_2 conversion, thermal-catalysis of CO_2 is still the most efficient and powerful method.[3] The discovery of novel pathways for direct CO_2 conversion to targeted products is imperative.

Aromatics, as the most important platform molecules for modern industry, are usually produced by naphtha hydrocracking. With the diminishing of the crude oil, the discovery of alternative strategy to produce aromatics is highly needed.[4,5] CO_2, a cheap and abundant carbon source, is an ideal feedstock for aromatics synthesis in view of the concept of low-carbon and sustainable development.[6] Being driven by the rapid development of low-cost water electrolysis hydrogen evolution techniques, thermal-catalyzed CO_2 hydrogenation to aromatics is becoming more and more promising.[7–9] In the past decades, much attention has been paid to CO_2 hydrogenation to basic chemicals, such as methanol and dimethyl ether (DME).[10,11] Recently, the direct conversion of CO_2 to aromatics has been realized via a methanol-mediated pathway, in which a bifunctional catalyst containing high-temperature methanol synthesis (such as Zn-ZrO_2, ZnAlOx, Cr_2O_3, and $ZnCrO_x$) and methanol to aromatics (MTA) active sites was employed.[12–15] However, the dominated CO production (more than 50% CO selectivity) due to the favorable reverse water gas shift reaction (RWGS, $CO_2 + H_2 \rightarrow CO + H_2O$) under the corresponding reaction conditions makes this strategy inefficient (as compared in Figure 3.1 and Table 3.1). Even though the co-feed of CO in the methanol-mediated pathway is an effective strategy to suppress the CO selectivity, the space time yield (STY) of aromatics is still low due to its limited reaction rate.[16] The modified Fischer-Tropsch synthesis (FTs) route for CO_2 conversion is a process

consisting of reverse water gas shift (RWGS) and FT synthesis reactions, and has been widely employed to realize the direct conversion of CO_2 to gasoline-range hydrocarbons or iso-paraffins over metal/zeolite multifunctional catalyst.[17,18] Theoretically, the combination of an alkenes-producing catalyst with a dehydrogenated aromatization zeolite can realize the direct conversion of CO_2 to aromatics in a tandem process, during which RWGS, FTs for alkenes production, and the subsequent alkenes dehydrocyclization are the main reactions of the whole process.[19,20] Recently, Liu *et al.* reported the direct conversion of CO_2 to aromatics via the Fe-based multifunctional catalysts.[21] Even though a higher aromatics yield was achieved through the modified FTs strategy compared with that of methanol-mediated pathway, it is still hard to meet the demand of industrial application. The critical point for the direct conversion of CO_2 to aromatics via the modified FTs strategy relies on the precise construction of multifunctional catalyst with appropriate intimacy mode.

Iron-based catalyst is the preferred catalyst candidate for CO_2 conversion via modified FTs due to its catalytic capability of both RWGS and FTs reactions.[22] The alkenes synthesis from CO_2 hydrogenation catalyzed by iron-based catalyst can be boosted by alkali metal (K or Na) modification.[23,24] For example, Sun *et al.* clarified the effect of Na doping on Fe_3O_4 for CO_2 hydrogenation to light olefins.[25] Gascon *et al.* compared the effect of different promoters on alkenes synthesis from CO_2 hydrogenation, and found that alkali metal K modified iron-based catalyst exhibited the most excellent alkenes selectivity.[26] On the other hand, the chemical and texture properties of the acidic zeolite play a vital role in determining the aromatics selectivity during the tandem process.[27] H-ZSM-5, with unique topology structure, is an ideal aromatics synthesis catalyst from methanol or alkenes.[20,28] However, the parent H-ZSM-5 usually possesses narrow channel and unsuitable acidic property, which lead to a high selectivity of undesirable short-chain hydrocarbons derived from the over-hydrocracking reaction.[29,30] The post-treatment of H-ZSM-5, especially etched by alkaline medium, is an efficient strategy to construct hierarchical structure, which is

beneficial to increase the mass-transfer efficiency of intermediates during the catalysis process.[31] Simultaneously, alkaline etching of H-ZSM-5 can modulate its acidic property by redistributing the Al species in zeolite skeleton.[32] Furthermore, the catalyst with hollow interior has attracted more and more attention owing to its outstanding mass-transfer efficiency and active sites accessibility.[33,34] It is no doubt that H-ZSM-5 with hollow structure can efficiently increase the selectivity of aromatics endowed by the shortened diffusion pathway of intermediates.[35,36] The formed aromatics are easier to leave the hollow H-ZSM-5 without undergoing the undesirable over-hydrocracking reaction that usually occurs in the narrow three-dimensional channels of untreated H-ZSM-5.[19]

In this report, a carbon encapsulated iron catalyst with Na modification (Na-Fe@C) was prepared using Fe-based metal-organic frameworks (Fe-MOFs) as precursors. Benefiting from the periodic structure of Fe-MOFs, highly dispersed Fe_3O_4 nanoparticles encapsulated by a few graphene-like carbon layers were obtained after pyrolysis of Fe-MOFs under N_2 atmosphere. After combining Na-Fe@C with the NaOH treated H-ZSM-5, the alkenes produced from Na-Fe@C can be converted to aromatics via the dehydrogenation and cyclization reactions on the acidic sites of H-ZSM-5. Surprisingly, the STY of aromatics (203.8 g_{CH2} kg_{cat}^{-1} h^{-1}) obtained from the multifunctional catalyst composed of Na-Fe@C and hollow H-ZSM-5 is higher than the data reported in other literature (Figure 3.1). Furthermore, the driving force in the tandem process was also clarified, the interplay between the two catalyst components facilitated the dehydrogenation and cyclization reactions of the intermediate alkenes, which was beneficial for the aromatics synthesis.

3.2. Experimental

3.2.1. Catalyst preparation

Firstly, the Fe-based MOFs was prepared by a hydrothermal method.[37] Typically, ferric nitrate nonahydrate [$Fe(NO_3)_3 \cdot 9H_2O$, 4.0 mmol, 1.62 g, Wako Pure Chemical

Co.] and triethylenediamine (2.0 mmol, 0.22 g, Wako Pure Chemical Co.) were dissolved in 50 mL of dimethyl formamide (DMF, Wako Pure Chemical Co.) under vigorous stirring for 30 min. Then a 10 mL DMF solution containing 1,4-benzenedicarboxylic acid (0.70 g, 4.2 mmol, Sigma-Aldrich Co.) was added to the above solution dropwise. After stirring for 1 h, the mixture was transferred into an 80 mL Teflon-lined autoclave and kept at 120 ^{o}C for 24 h. The crystalline products were recovered by centrifugation, followed by washing with DMF three times and drying at 60 ^{o}C in a vacuum oven overnight. The Fe catalyst for alkenes synthesis was prepared by pyrolysis of Fe-MOFs at 550 ^{o}C for 3 h under N_2 atmosphere with a heating rate of 2 ^{o}C min^{-1}. The MOFs derived catalyst was denoted as Fe@C. Na-Fe@C with 0.47 wt% Na (determined by X-ray fluorescence spectrum) was prepared by a wetness impregnation method with Na_2CO_3 (Sigma-Aldrich Co.) as Na source.

The acidic zeolite H-ZSM-5 was prepared according to a method reported in other literature.[14,16] To prepare the hollow H-ZSM-5, the parent H-ZSM-5 (4 g) was immersed into aqueous solution of NaOH (100 mL) with different concentrations. After being treated at 80 ^{o}C for 1 h, the white solid was collected by centrifugation, washed with deionized water, dried at 120 ^{o}C for 8 h, and then calcined at 350 ^{o}C for 6 h. At last, the NaOH treated zeolite (2 g) was ion-exchanged in aqueous solution of NH_4NO_3 (200 mL, 1.0 mol L^{-1}) for three times. The ion-exchanged zeolite was dried at 120 ^{o}C for 8 h, and then calcined at 350 ^{o}C for 6 h to get the proton-formed zeolite. The NaOH treated zeolite was denoted as H-ZSM-5-X, where X represents the NaOH concentration. The multifunctional catalyst with a granule stacking mode was constructed by physical mixing the Na-Fe@C (0.1 g, 20-40 meshes) and H-ZSM-5-X (0.1-0.5 g, 20-40 meshes) granules in a vessel. Na-Fe@C&H-ZSM-5-0.2M was prepared by physical mixing. Typically, Na-Fe@C and H-ZSM-5-0.2M were mixed in an agate mortar for 10 min, and then pressed, crushed, and sieved to 20-40 meshes. Na-Fe@C‖H-ZSM-5-0.2M was prepared by separating the two catalyst components into two reactors.

3.2.2. Catalyst characterizations

The crystal structures of the catalysts were recorded by a Rigaku RINT 2400 X-ray diffractometer with Cu Kα radiation. The element contents in the catalysts were measured by a Phillips 2400 X-ray fluorescence (XRF) spectrometer. X-ray photoelectron spectroscopy (XPS) was performed on a Thermo Fisher Scientific ESCALAB 250Xi multifunctional spectroscopy with an in situ reduction chamber. The morphologies of the catalysts were observed by a transmission electron microscopy (TEM, JEM-2100UHR, JEOL) and a scanning TEM (STEM, JEM-2100F, JEOL). The specific surface areas and pore size distributions of the catalysts were measured by a Micromeritics 3Flex 2MP instrument. Prior to the measurements, the catalysts were degassed at 300 ^{o}C for 10 h. The specific surface area was calculated by the Brunauer-Emmett-Teller (BET) method, and the average pore size and pore volume were calculated based on the Barrett-Joyner-Halenda (BJH) method. The pore size distribution was analyzed according to the BJH (mesopores) and Horváth-Kawazoe (HK, micropores) methods. $NH_3/CO_2/H_2$ temperature programmed desorption (TPD) were performed on a MicrotracBEL BELCATII-T-SP instrument. For the TPD tests, the catalyst (50 mg) was pretreated at 150 ^{o}C for 1h in a flow of pure He. Then the sample was saturated with the targeted molecules at 50 ^{o}C. After removing the physisorbed molecules by He flow, the desorption profiles were recorded under He flow with a heating rate of 10 ^{o}C min^{-1}. Pyridine adsorbed FTIR spectra were recorded by a Bruker Tensor 27 FTIR spectrometer. Prior to the test, the catalyst was pressed into a self-supported wafer and degassed at 400 ^{o}C and 10^{-4} pa for 1h. The adsorption of pyridine molecules was performed at 50 ^{o}C for 1 h. Then the IR spectra were collected when the catalyst was heated to 100, 200, or 350 ^{o}C with a heating rate of 10 ^{o}C min^{-1}.

3.2.3. Catalytic tests

The catalytic performances of the catalysts were measured in a fixed-bed reactor with an internal diameter of 6 mm. Prior to the reaction, the catalyst was reduced by pure H_2 at 400 °C for 8 h. After cooling down to room temperature, the reactant gas (24.3% CO_2, 71.8% H_2, and 3.9% Ar) was fed into the reactor until the pressure reaches 3 MPa. At the same time, the temperature of the reactor was increased to 320 °C. An ice trap set between the reactor and the back pressure valve was employed to collect the heavy hydrocarbons. The heavy hydrocarbons were analyzed by an off-line gas chromatograph (GC, Shimadzu GC-2014) equipped with a flame ionization detector (FID) and a DB-1 capillary column. The reaction effluents were analyzed by two on-line GCs (Shimadzu GC-2014), one equipped with a thermal conductive detector (TCD) and an active charcoal column for Ar, CO, CH_4, and CO_2 analysis, another one equipped with a FID and a Porapak-Q column for the analysis of light hydrocarbons. The selectivity of hydrocarbons in the products was calculated on the molar carbon basis. The carbon balances of the reaction data were calculated, which were all higher than 90%. And the reaction data after 12 h were used for discussion. Na-Fe@C∥H-ZSM-5-0.2M represents two catalyst components loaded into two reactors. Na-Fe@C particles (20-40 meshes) was loaded into reactor 1 for alkenes synthesis and H-ZSM-5-0.2M (20-40 meshes) was loaded into reactor 2 for alkenes conversion to aromatics. For the conversion of 1-hexene via H-ZSM-5-0.2M and Na-Fe@C*/H-ZSM-5-0.2M (Na-Fe@C* represents the spent Na-Fe@C catalyst after CO_2 hydrogenation), the pressure and temperature of the reactor were firstly increased to 2 MPa and 320 °C, respectively. Then the liquid 1-hexene was fed into the gasification chamber by a TOSOH DP 8020 pump. The gaseous 1-hexene was carried into the catalyst bed to initiate the reaction with the help of N_2 or CO_2 gas flow.

3.3. Results and discussion

3.3.1. MOFs derived Fe-based catalyst

The preparation procedures for Fe-based alkenes synthesis catalyst are illustrated in Scheme 1. Firstly, Fe-based metal-organic frameworks (Fe-MOFs) were synthesized by a hydrothermal method. Then Fe-MOFs were pyrolyzed to Fe/C composites under N_2 atmosphere (denoted as Fe@C). The X-ray diffraction (XRD) pattern of Fe@C (Figure 3.2a) shows strong typical peaks assigned to Fe_3O_4 phase. Fe_3O_4 has been widely recognized as the active site for reverse water-gas shift reaction (RWGS, $CO_2 + H_2 \rightarrow CO + H_2O$), which is the initial step for CO_2 conversion through a modified Fischer-Tropsch synthesis (FTs) route. Benefiting from the periodic architecture of the Fe-MOFs, Fe@C catalyst exhibits hierarchical structure accompanied with significant N_2 adsorption at low pressure and obvious hysteresis loop as shown in the N_2 adsorption-desorption isotherms (Figure 3.2b and Table 3.2). Unfortunately, Fe@C exhibited poor alkenes selectivity (5%) in CO_2 hydrogenation under 320 °C and 3 MPa. After Na doping, the catalytic performance of Na-Fe@C underwent significant changes with high alkenes selectivity amounting to 70.6% at a CO_2 conversion of 30.6% (Table 3.3).

3.3.2. The role of Na in Na-Fe@C for alkenes synthesis from CO_2 hydrogenation

To elucidate the promotion role of Na in alkenes synthesis, multiple characterization techniques, such as XRD, XPS, and CO_2/H_2 temperature programmed desorption (CO_2/H_2-TPD), were performed on the used Fe@C and Na-Fe@C. In addition to the typical peak of the majority Fe_3O_4, Fe_5C_2 phase was also detected in the XRD pattern of the used Na-Fe@C (Figures 3.3a and 3.3b), while only Fe_3C phase appeared in the used Fe@C, which has been proved to be less active than Fe_5C_2 for alkenes synthesis in FTs.[26,38] The chemical states of Fe species in the catalysts were characterized by XPS technique. As shown in Figure 3.4, divalent (Fe^{2+}, at 711.0 and 724.0 eV) and trivalent Fe (Fe^{3+}, at 713.1 and 726.1 eV) were detected in all three catalysts Fe@C,

used Fe@C, and used Na-Fe@C. The appearance of Fe-C bond (704.6 eV) in the used Na-Fe@C catalyst confirmed the formation of iron carbides during the reaction, which is consistent with the XRD results. No Fe-C species were found in the XPS spectra of the used Fe@C catalyst due to the detection limits of the instrument. More in-depth, CO_2/H_2-TPD was employed to clarify the surface chemical properties of the spent Fe@C and Na-Fe@C. As we know, the re-adsorption of alkenes and their further hydrogenation on the surface of catalyst are the primary factors leading to the low alkenes selectivity. The spent Na-Fe@C exhibited stronger CO_2 adsorption capability with higher CO_2 desorption temperature compared with that of Fe@C without Na doping (Figure 3.3c). Conversely, the H_2 desorption temperature of Na-Fe@C was approximately 10 ^{o}C lower than that of Fe@C, which confirmed its weaker H_2 adsorption ability (Figure 3.3d). The adsorption of CO_2 on Na-Fe@C was enabled by the electron transfer from Na-Fe@C to CO_2. The strength of chemical bond between Fe and CO_2 (Fe-C) was enhanced after Na doping due to the electron donating property of alkali metals, which is beneficial for the adsorption of acidic CO_2 molecules on Na-Fe@C.[39] However, the similar electron donating property of H_2 with alkali metals led to its weaker adsorption strength on the surface of Na-Fe@C. More importantly, alkenes with C=C double bond are typical Lewis bases, which are difficult to be adsorbed onto the basis surface of Na-Fe@C due to Na existence. Consequently, the interface of Na-Fe@C with deficient H_2 effectively suppressed the unfavorable over-hydrogenation of the re-adsorbed alkenes, which endowed Na-Fe@C with excellent catalytic performance for alkenes synthesis from CO_2 hydrogenation.

3.3.3. Morphology of the spent Na-Fe@C catalyst

The microstructure of the used Na-Fe@C was characterized by transmission electron microscopy (TEM). As shown in Figure 3.5a, Fe-based nano-polyhedrons with a diameter in the range of 30-40 nm were uniformly dispersed on the carbon carriers. As expected, the MOF derived Fe-based nano-polyhedrons were encapsulated by a few

carbon layers (Figure 3.5b), which is effective to suppress the undesirable aggregation during the catalytic process. This core-shell structure of Na-Fe@C has great potential for CO_2 conversion, a) high metal loadings for catalytic reaction without aggregation; 2) the core-shell structure maximizes the dispersion of the metal particles, which is beneficial to the efficient utilization of the active sites; 3) the carbon layers surrounded the metal particles can suppress the undesirable deactivation phenomena.[40-42] The scanning TEM (STEM) and EDS mapping images of the used Na-Fe@C further confirmed that Fe-based nano-polyhedrons were individually anchored on the carbon carriers, and the alkali metal Na was homogeneously distributed on the catalyst substrate (Figure 3.5c).

3.3.4. Multifunctional catalyst (Na-Fe@C/H-ZSM-5) for direct conversion of CO_2 to aromatics

A multifunctional catalyst system composed of alkenes synthesis catalyst Na-Fe@C and acidic zeolite H-ZSM-5 (Na-Fe@C/H-ZSM-5) were constructed to realize the direct conversion of CO_2 to aromatics in a single-pass. Ideally, the alkenes produced from Na-Fe@C catalyst can be converted to aromatics through dehydrogenation and cyclization reactions on acidic H-ZSM-5 with unique topology structure. After combining Na-Fe@C with H-ZSM-5, more aromatics (30.9%, Figure 3.6 and Table 3.3) were produced along with the ratio of alkenes to alkanes decreased greatly from 5.63 to 0.68, indicating that the aromatics were mainly produced from the dehydrogenation and cyclization of alkenes on H-ZSM-5. However, the high iso-paraffin/paraffin ratio (3.56) and low aromatics selectivity obtained from Na-Fe@C/H-ZSM-5 turned our attention to the precise regulation of acidic and texture properties of the acidic zeolite, which have been widely recognized as the vital factors affecting the products distribution in zeolite-catalyzed reactions.[43,44]

3.3.5. Fabrication of the hierarchical zeolites and their catalytic performances

Alkaline treatment is seemed to be the most efficient method to construct hierarchical structured H-ZSM-5 because this strategy not only constructs hierarchical structure by desilication but also tunes the acidic property of H-ZSM-5.[45,46] The parent H-ZSM-5 was treated by NaOH medium with different concentrations, and the desilicated H-ZSM-5 was denoted as H-ZSM-5-X, where X represents the concentration of NaOH solution. The selectivity of aromatics was increased to 40.0% on Na-Fe@C/H-ZSM-5-0.1M along with a decrease in selectivity of C_{5+} non-aromatics (Figure 3.6 and Table 3.3). Higher aromatics selectivity of 50.2% was achieved by combining Na-Fe@C with H-ZSM-5-0.2M etched by a higher concentration of NaOH solution. However, further increasing the concentration of NaOH medium to 0.4 M (H-ZSM-5-0.4M) resulted in a dramatic decrease in aromatics selectivity (27.8%).

3.3.6. Texture properties of the hierarchical zeolites

The trends in catalytic performance mentioned above can be attributed to the variations of architectures and acidic properties of the NaOH treated H-ZSM-5. As shown in Figure 3.7 and Figure 3.8, H-ZSM-5-0.2M with hollow zeolite architecture was fabricated by NaOH etching due to the Al gradient contained in the parent H-ZSM-5 crystals. The process of Si extraction can be controlled by the distribution of framework Al in zeolite skeleton. High framework Al concentration suppresses the Si extraction, conversely low framework Al concentration leads to the excessive Si extraction. The different Si extraction rates in H-ZSM-5 with Al-rich external surface (denoted Al-zoned) upon NaOH etching guaranteed the formation of hollow architecture.[47,48] Compared with the bulk H-ZSM-5, the hollow structure of H-ZSM-5-0.2M with thin shell of ~20 nm (Figure 3.8b) will greatly reduce the residue time of intermediates in the channel of zeolite, thereby suppressing the undesirable over-hydrocracking of hydrocarbons. In addition to the hollow architecture, some holes with a diameter of ~10 nm were also detected in the shell of H-ZSM-5-0.2M. These

holes can be acted as nano-tracks connecting the exterior and interior of H-ZSM-5-0.2M, which accelerate the mass transfer during the catalytic process.

The N_2 adsorption-desorption isotherm of the parent H-ZSM-5 exhibited microporous property with sharp N_2 uptake at the low relative pressure (Figure 3.9). After NaOH treatment, mesoporous structures were formed as confirmed by the appearance of obvious hysteresis loop. The mesopore volume and specific surface area increased with increasing the NaOH concentration from 0.1 to 0.2 M (Table 3.2). However, further increasing the NaOH concentration to 0.4 M led to a decrease in mesopore specific surface area, which originated from the collapse of zeolite framework under such a strong alkaline solution. This phenomenon can also be proved by the decreased XRD intensity (Figure 3.10) and confusing external morphology as shown in TEM images (Figure 3.11).

3.3.7. Acidic properties of the hierarchical zeolites

The variations in acidic properties of alkaline treated H-ZSM-5 were investigated by NH_3-TPD and in-situ pyridine adsorption FTIR. NH_3-TPD profiles of H-ZSM-5 and NaOH-treated H-ZSM-5 (Figure 3.12a) confirmed that the acid strengths and densities were increased after alkaline treatment with the typical NH_3 desorption peaks enlarged and shifted to higher temperatures. The in-situ pyridine adsorption FT-IR spectra of H-ZSM-5 and NaOH treated H-ZSM-5 confirmed the existence of Brønsted (1540 cm^{-1}) and Lewis (1450 cm^{-1}) acid sites in the zeolites (Figure 3.12b and Figure 3.13). It has been widely accepted that the medium and strong Brønsted acid sites in H-ZSM-5 play key roles in determining the catalytic performance for dehydrogenation and cyclization of alkenes to aromatics.[49] By recording the FT-IR spectra after pyridine evacuation at different temperatures, the acid sites with different strengths in the zeolites were analyzed quantitatively. As shown in Figure 3.12c, the amount of (medium + strong) acid sites in H-ZSM-5 increased dramatically after NaOH treatment, which is consistent with the NH_3-TPD findings. The variation in acid sites density of Al-zoned H-ZSM-5

after NaOH etching is different from that of traditional H-ZSM-5 treated with NaOH medium. For the traditional H-ZSM-5 with Al species distributed in the crystals homogeneously, the density of strong Brønsted acid sites usually decreases after desilication by NaOH medium due to the destruction of Si-O-Al bonds in the zeolite skeleton. However, for the Al-zoned H-ZSM-5, the desilication process occurs preferentially in the Si-rich interior due to the Al gradients in the zeolite crystals. Therefore, the NaOH treated Al-zoned H-ZSM-5 (hollow H-ZSM-5) with increased density of Si-O-Al bonds in unit mass possesses much more Brønsted acid sites compared with the parent H-ZSM-5. Based on the characterization results, the excellent catalytic performance of Na-Fe@C/H-ZSM-5-0.2M for aromatics synthesis can be attributed to the synergistic effect between the appropriate amount of Brønsted acid sites and hierarchical structure of H-ZSM-5-0.2M. Even though higher aromatics selectivity (40.0%) was obtained on Na-Fe@C/H-ZSM-5-0.1M due to the increased amount of medium and strong Brønsted acid sites in H-ZSM-5-0.1 compared with the parent H-ZSM-5, the narrow pore size and volume of H-ZSM-5-0.1 (Table 3.2) still led to the over-hydrocracked of long-chain hydrocarbons to light alkanes (C_2-C_4^0, 15.1%). On the other hand, high CH_4 and C_{5+} non-aromatics selectivities were obtained from Na-Fe@C/H-ZSM-5-0.4M with larger pore size and volume, which can be attributed to the excessive Brønsted acid sites in H-ZSM-5-0.4M. In addition to the important role of Brønsted acid, the synergistic effect between the Brønsted and Lewis acid sites has also been proven to play a vital role in enhancing the aromatics selectivity.[50] It has been widely accepted that cyclohexene and cyclopentene are the main intermediates during aromatics synthesis on the acid sites of zeolite. Here cyclohexene was employed as an example. As shown in Figure 3.14a, the cycloalkenes are readily cracked to light hydrocarbons on the Brønsted acid sites, which results in lower aromatics selectivity. However, the Lewis acid sites can be employed as active site for C-H activation (Figure 3.14b). The cyclohexene is liable to form carbenium ions via the strong Lewis acid sites by the hydride abstraction. Then the hydride combines with the acidic proton in the

Bronsted acid site. After the H_2 releasing, the cyclic carbenium ion undergoes the further deprotonation, leading to the formation of cyclodihexene and the recovery of the Brønsted acid site. After repeating this process, aromatics will be produced. Therefore, the co-existence of Brønsted and Lewis acid sites is beneficial for aromatics synthesis due to their cooperative effect.

3.3.8. Optimal reaction conditions for aromatics synthesis by Na-Fe@C/H-ZSM-5-0.2M

In order to further clarify the structure-function effect of the bifunctional catalyst in the tandem process, a series of reference experiments were performed. The weight ratio of Na-Fe@C to H-ZSM-5-0.2M was varied to explore the effect of acid sites density on aromatics selectivity (Table 3.4). When increasing the amount of H-ZSM-5-0.2M in the bifunctional catalyst (weight ratio, from 1:1 to 1:3), the aromatics selectivity was increased from 31.6% to 50.2 %, accompanied by a decrease in the ratio of olefins to paraffins (o/p, from 1.19 to 0.66). However, further increasing the amount of zeolite led to a decrease in the aromatics selectivity, while much more isoparaffins were produced due to the over-hydrocracking reaction on the excessive Brønsted acid sites. Therefore, an appropriate amount of Brønsted acid sites in the bifunctional catalyst is essential to the aromatics synthesis in the tandem process. In addition to the appropriate density of Brønsted acid sites, the unique hollow structure of H-ZSM-5-0.2M also played an important role in enhancing the aromatics selectivity in the tandem process. The hollow H-ZSM-5-0.2M with thin shell and shortened intermediates diffusional pathway will effectively suppress the undesirable hydrocracking and isomerization reactions that usually occurred in the bulk zeolite crystals.

The optimal reaction conditions for aromatics synthesis from CO_2 hydrogenation via Na-Fe@C/H-ZSM-5-0.2M were also studied (Table 3.5). Long contact time (low GHSV, 6000 mL g_{cat}^{-1} h^{-1}) of intermediates on the acidic zeolite produced much more CH_4 and C_2-C_4^0 due to over-hydrocracking of hydrocarbons in the zeolite channels. On

the other hand, higher GHSV (12000 mL g_{cat}^{-1} h^{-1}) made the alkenes produced on Na-Fe@C leave the catalyst bed quickly, without undergoing the dehydrogenation and cyclization reactions on the acid zeolite, which was proved by the high ratio of alkenes to paraffins (o/p = 0.88). Even though higher reaction temperature (350 ^{o}C) is beneficial for the CO_2 conversion due to the endothermic property of RWGS reaction, the hydrocracking reaction of the intermediates will also be accelerated under such hydrogen-rich atmosphere, which is harmful to the aromatics synthesis.

The catalytic performances of the multifunctional catalyst with different intimacy modes were investigated. As shown in Table 3.6, Na-Fe@C&H-ZSM-5-0.2M with the closest proximity exhibited low CO_2 conversion and high selectivity of CH_4. This products distribution can be attributed to the poison of basic catalytic interface of Na-Fe@C by the acid sites of H-ZSM-5-0.2M. In the above discussion, the important role of alkali doping in Na-Fe@C for alkenes synthesis has been clarified. However, when the two components were separated into two reactors (denoted as Na-Fe@C‖H-ZSM-5-0.2M), the CO_2 conversion (29.5%) and aromatics selectivity (46.1%) were slightly decreased. The aromatics selectivity from Na-Fe@C‖H-ZSM-5-0.2M (46.1%) with two catalyst components separated into two reactors is very close to that of Na-Fe@C/H-ZSM-5-0.2M (50.2%). However, for the practical application, the catalytic reaction operated in a single reactor is a more cost-effective strategy compared with the two reactor series. On the other hand, slight differences in the catalytic performances can also be detected between this two intimacy modes. In addition to the slight decrease in the aromatics selectivity, the CO_2 conversion was also decreased from 33.3% to 29.5% after separating two catalyst components into two reactors. For Na-Fe@C/H-ZSM-5-0.2M, the alkenes produced from Na-Fe@C can be consumed easily by the acidic zeolite due to the short diffusional pathway from Na-Fe@C to H-ZSM-5-0.2M, and this continuous consumption of alkenes by zeolite can shift the chemical thermodynamic equilibrium forward, which is beneficial for CO_2 conversion. Na-Fe@C‖H-ZSM-5-0.2M with prolonged distance between two components is difficult to convert the

intermediates immediately, therefore, the driving force between Na-Fe@C and H-ZSM-5-0.2M was reduced in the two reactor series. Therefore, the intimacy mode is also an important factor for aromatics synthesis from the tandem reaction of CO_2 hydrogenation.

3.3.9. Long-term stability of Na-Fe@C/H-ZSM-5-0.2M and Na-Fe@C/H-ZSM-5

The long-term stability of Na-Fe@C/H-ZSM-5-0.2M and Na-Fe@C/H-ZSM-5 was tested at 320 $^{\circ}$C and 3 MPa (Figure 3.15). Na-Fe@C/H-ZSM-5-0.2M exhibited superior stability with no obvious degradation in CO_2 conversion and aromatics selectivity after long-term stability test of 60 h. However, for Na-Fe@C/H-ZSM-5 catalyst, the selectivity of aromatics was decreased from 30.9% to 21.8% during reaction of 60 h. The short lifetime of Na-Fe@C/H-ZSM-5 can be attributed to the rapid coke deposition in the channels of H-ZSM-5, which will cover the acidic sites for aromatics synthesis. As shown in the TG curves of the spent zeolite, H-ZSM-5-0.2M with hollow cavity and thin shell exhibited less weight loss (1.2%, Figure 3.16), corresponding to the less carbon deposition amount. In contrast, H-ZSM-5 with long channels will slow down the diffusional efficiency of reactants and products, which increases the probability of carbon deposition during the reaction process (3% weight loss). Thus, it is reasonable to conclude that NaOH treatment not only tailored the acidic property of zeolite, but also fabricated the hollow structure to shorten the diffusional pathway of the reaction intermediates, which is beneficial to suppress the carbon deposition.

3.3.9. Identification of the driving force in the tandem process

In order to identify the driving forces for aromatics synthesis in the tandem process, the conversion of 1-hexene, a model intermediate during the tandem process, catalyzed by H-ZSM-5-0.2M or Na-Fe@C*/H-ZSM-5-0.2M (Na-Fe@C*, spent Na-Fe@C after CO_2 hydrogenation) was performed under N_2 or CO_2 atmosphere (Figure 3.17a and

Table 3.7). For H-ZSM-5-0.2M, low selectivity for aromatics ($< 35\%$) were observed under either CO_2 or N_2 atmosphere. The selectivity of aromatics was increased to 37.4% on the multifunctional catalyst Na-Fe@C*/H-ZSM-5-0.2M under N_2 atmosphere due to the H species adsorption capability of Fe-based catalyst as determined by H_2-TPD measurements (Figure 3.3d). The tandem catalysis process catalyzed by the multifunctional catalyst was not the simple combination of several reactions (mainly RWGS, alkenes synthesis, and alkenes dehydrogenative aromatization reactions). In fact, the targeted aromatics synthesis from tandem CO_2 conversion can be regarded as a result of the cooperative interplay between Na-Fe@C* and H-ZSM-5-0.2M. The H species produced from the dehydrogenative aromatization of alkenes on H-ZSM-5-0.2M can be adsorbed by Na-Fe@C* catalyst, which is beneficial for the conversion of 1-hexene to aromatics. Interestingly, on switching to a CO_2 atmosphere, the aromatics selectivity over Na-Fe@C*/H-ZSM-5-0.2M was further increased to 45.8%. In addition to the cooperative interplay between the multifunctional catalysts, it is evident that the reaction atmosphere also played an important role in determining and promoting the aromatics synthesis from the tandem catalysis of CO_2 hydrogenation. As shown in Figure 3.17b, different from the 1-hexene conversion over Na-Fe@C*/H-ZSM-5-0.2M in N_2 atmosphere, CO_2 present in the reaction can be employed as acceptors for H species being adsorbed on the surface of Na-Fe@C*. This continuous H species removal realized by CO_2 hydrogenation catalytic activity of Na-Fe@C* guaranteed the accelerated conversion of alkenes to aromatics by shifting the chemical thermodynamic equilibrium.[14] The driving force derived from the multiple active sites will be reduced after separating the two catalyst components into two reactors along with the decreases of CO_2 conversion and aromatics selectivity in Na-Fe@C‖H-ZSM-5-0.2M mode (Table 3.6). This phenomenon can be attributed to the suppressed removal of H species produced from dehydrogenation and aromatization reactions due to the prolonged distance between the two catalyst components. At last, the conversion of 1-hexene catalyzed by Na-Fe@C*/H-ZSM-5 was also performed in a CO_2

atmosphere. Unfortunately, the aromatics selectivity was severely hampered by the tedious channels in H-ZSM-5, where undesirable isomerization and alkylation reactions usually occurred.

3.4. Conclusion

The direct conversion of CO_2 to aromatics was realized by a multifunctional catalyst Na-Fe@C/H-ZSM-5-0.2M with precisely tailored catalytic interface and acidity. Na-Fe@C prepared by pyrolysis of Fe-based MOFs exhibited high alkenes selectivity (70.6%) at a CO_2 conversion of 30.6% due to its appropriate intermediate adsorption capability and high active sites accessibility. After combining with alkali-treated acidic H-ZSM-5, the alkenes produced from Na-Fe@C were converted to aromatics through the dehydrogenative aromatization reaction. The suitable acid density and strength in the multifunctional catalyst, which play a vital role in the synthesis of aromatics, were systematically investigated. Different from the simple combination of two catalyst components, the cooperative interplay between Na-Fe@C and H-ZSM-5-0.2M guaranteed the enhanced aromatics synthesis from the tandem CO_2 conversion. CO_2 adsorbed on Fe-based catalyst acted as acceptors for the H species produced from the dehydrogenation and cyclization reactions, thereby accelerating the conversion of alkenes to aromatics by shifting the thermodynamic equilibrium. Our study not only provides a novel multifunctional catalyst system for direct conversion of CO_2 to value-added aromatics but also sheds new light on the sustainable strategy to alleviate the environmental pressure derived from carbon emissions.

References

[1] D.R. Feldman, W.D. Collins, P.J. Gero, M.S. Torn, E.J. Mlawer, T.R. Shippert, Observational determination of surface radiative forcing by CO_2 from 2000 to 2010, Nature 519 (2015) 339-343.

[2]   G.A. Olah, G.K.S. Prakash, A. Goeppert, Anthropogenic chemical carbon cycle for a sustainable future, J. Am. Chem. Soc. 133 (2011) 12881-12898.

[3]   W. Wang, S. Wang, X. Ma, J. Gong, Recent advances in catalytic hydrogenation of carbon dioxide, Chem. Soc. Rev. 40 (2011) 3703-3727.

[4]   P. Zhang, L. Tan, G. Yang, N. Tsubaki, One-pass selective conversion of syngas to para-xylene, Chem. Sci. 8 (2017) 7941-7946.

[5]   A.M. Niziolek, O. Onel, Y.A. Guzman, C.A. Floudas. Biomass-Based Production of Benzene, Toluene, and Xylenes via Methanol: Process Synthesis and Deterministic Global Optimization, Energy Fuels 30 (2016) 4970-4998.

[6]   P. Zhu, J. Sun, G. Yang, G. Liu, P. Zhang, Y. Yoneyama, N. Tsubaki, Tandem catalytic synthesis of benzene from CO_2 and H_2, Catal. Sci. Technol. 7 (2017) 2695-2699.

[7]   V. Kumaravel, S. Mathew, J. Bartlett, S. C. Pillai, Photocatalytic hydrogen production using metal doped TiO_2: A review of recent advances, Appl. Catal. B-Environ. 244 (2019) 1021-1064.

[8]   T. Wang, Y. Wei, X. Chang, C. Li, A. Li, S. Liu, J. Zhang, J. Gong, Homogeneous Cu_2O p-n junction photocathodes for solar water splitting, Appl. Catal. B-Environ. 226 (2018) 31-37.

[9]   Y. Wang, S. Zhu, N. Tsubaki, M. Wu, Highly dispersed Mo_2C anchored on N,P-codoped graphene as efficient electrocatalyst for hydrogn evolution reaction, ChemCatChem 10 (2018) 2300-2304.

[10] X. Dong, F. Li, N. Zhao, F. Xiao, J. Wang, Y. Tan, CO_2 hydrogenation to methanol over $Cu/ZnO/ZrO_2$ catalysts prepared by precipitation-reduction method, Appl. Catal. B-Environ. 191 (2016) 8-17.

[11] F. Frusteri, G. Bonura, C. Cannilla, G.D. Ferrante, A. Aloise, E. Catizzone, M. Migliori, G. Giordano, Stepwise tuning of metal-oxide and acid sites of CuZnZr-MFI hybrid catalysts for the direct DME synthesis by CO_2 hydrogenation, Appl. Catal. B-Environ. 176-177 (2015) 522-531.

[12] Z. Li, Y. Qu, J. Wang, H. Liu, M. Li, S. Miao, C. Li, Highly selective conversion of carbon dioxide to aromatics over Tandem Catalysts, Joule 3 (2019) 570-583.

[13] Y. Ni, Z. Chen, Y. Fu, Y. Liu, W. Zhu, Z. Liu, Selective conversion of CO_2 and H_2 into aromatics, Nat. Commun. 9 (2018) 3457.

[14] Y. Wang, G. Gao, S. Kazumi, H. Li, G. Yang, N. Tsubaki, Direct and oriented conversion of CO_2 into value-added aromatics, Chem. Eur. J. 25 (2019) 5149-5153.

[15] J. Zhang, M. Zhang, S. Chen, X. Wang, Z. Zhou, Y. Wu, T. Zhang, G. Yang, Y. Han, Y. Tan, Hydrogenation of CO_2 into aromatics over ZnCrOx–zeolite composite catalyst, Chem. Commun. 55 (2019) 973-976.

[16] Y. Wang, L. Tan, M. Tan, P. Zhang, Y. Fang, Y. Yoneyama, G. Yang, N. Tsubaki, Rationally designing bifunctional catalysts as an efficient strategy to boost CO_2 hydrogenation producing value-added aromatics, ACS Catal. 9 (2019) 895-901.

[17] J. Wei, R. Yao, Q. Ge, Z. Wen, X. Ji, C. Fang, J. Zhang, H. Xu, Sun, J. Catalytic hydrogenation of CO_2 to isoparaffins over Fe-based multifunctional catalysts, ACS Catal. 8 (2018) 9958-9967.

[18] J. Wei, Q. Ge, R. Yao, Z. Wen, C. Fang, L. Guo, H. Xu, J. Sun, Directly converting CO_2 into a gasoline fuel, Nat. Commun. 8 (2017) 15174.

[19] Y. Xu, J. Liu, J. Wang, G. Ma, J. Lin, Y. Yang, Y. Li, C. Zhang, M. Ding, Selective conversion of syngas to aromatics over Fe_3O_4@MnO_2 and hollow HZSM-5 bifunctional catalysts, ACS Catal. 9 (2019) 5147-5156.

[20] B. Zhao, P. Zhai, P. Wang, J. Li, T. Li, M. Peng, M. Zhao, G. Hu, Y. Yang, Y. Li, Q. Zhang, W. Fan, D. Ma, Direct transformation of syngas to aromatics over Na-Zn-Fe_5C_2 and hierarchical HZSM-5 tandem catalysts. Chem 3 (2017) 323-333.

[21] Y. Xu, C. Shi, B. Liu, T. Wang, J. Zheng, W. Li, D. Liu, X. Liu, Selective production of aromatics from CO_2, Catal. Sci. Technol. 9 (2019) 593-610.

[22] M.K. Gnanamani, G. Jacobs, H.H. Hamdeh, W.D. Shafer, F. Liu, S.D. Hopps, G.A. Thomas, B.H. Davis, Hydrogenation of carbon dioxide over Co-Fe bimetallic catalysts, ACS Catal. 6 (2016) 913-927.

[23] L. Guo, J. Sun, X. Ji, J. Wei, Z. Wen, R. Yao, H. Xu, Q. Ge, Directly converting carbon dioxide to linear α-olefins on bio-promoted catalysts, Commun. Chem. 1 (2018) 11.

[24] W.D. Shafer, G. Jacobs, U.M. Graham, H.H. Hamdeh, B.H. Davis, Increased CO_2 hydrogenation to liquid products using promoted iron catalysts, J. Catal. 369 (2019) 239-248.

[25] J. Wei, J. Sun, Z. Wen, C. Fang, Q. Ge, H. Xu, New insights into the effect of sodium on Fe_3O_4-based nanocatalysts for CO_2 hydrogenation to light olefins, Catal. Sci. Technol. 6 (2016) 4786-4793.

[26] A. Ramirez, L. Gevers, A. Bavykina, S. Ould-chikh, J. Gascon, Metal organic framework-derived iron catalysts for the direct hydrogenation of CO_2 to short chain olefins, ACS Catal. 8 (2018) 9174-9182.

[27] X. Cui, P. Gao, S. Li, C. Yang, Z. Liu, H. Wang, L. Zhong, Y. Sun, Selective Production of Aromatics Directly from Carbon Dioxide Hydrogenation, ACS Catal. 9 (2019) 3866-3876.

[28] N. Wang, Y. Hou, W. Sun, D. Cai, Z. Chen, L. Liu, B. Ge, L. Hu, W. Qian, F. Wei, Modulation of b-axis thickness within MFI zeolite: Correlation with variation of product diffusion and coke distribution in the methanol-to-hydrocarbons conversion, Appl. Catal. B-Environ. 243 (2019) 721-733.

[29] X. Peng, K. Cheng, J. Kang, B. Gu, X. Yu, Q. Zhang, Y. Wang, Impact of hydrogenolysis on the selectivity of the Fischer-Tropsch synthesis: diesel fuel production over mesoporous zeolite-Y-supported cobalt nanoparticles, Angew. Chem. Int. Ed. 54 (2015) 4553-4556.

[30] J. Li, Y. He, L. Tan, P. Zhang, X. Peng, A. Oruganti, G. Yang, H. Abe, Y. Wang, N. Tsubaki, Integrated tuneable synthesis of liquid fuels via Fischer–Tropsch technology, Nat. Catal. 1 (2018) 787-793.

[31] J. He, D. Chen, N. Li, Q. Xu, H. Li, J. He, J. Lu, Controlled fabrication of mesoporous ZSM-5 zeolite-supported PdCu alloy nanoparticles for complete oxidation of toluene, Appl. Catal. B-Environ. 265 (2020) 118560.

[32] J. Li, M. Liu, X. Guo, S. Xu, Y. Wei, Z. Liu, C. Song, Interconnected hierarchical ZSM-5 with tunable acidity prepared by a dealumination−realumination process : a superior MTP catalyst, ACS Appl. Mater. Interfaces 9 (2017) 26096-26106.

[33] Y. Wang, D. Wang, M. Tan, B. Jiang, J. Zheng, N. Tsubaki, M. Wu, Monodispersed hollow SO_3H-functionalized carbon/silica as efficient solid acid catalyst for esterification of oleic acid, ACS Appl. Mater. Interfaces 7 (2015) 26767-26775.

[34] X. Wang, J. Feng, Y. Bai, Q. Zhang, Y. Yin, Synthesis, properties, and applications of hollow micro-/nanostructures, Chem. Rev. 116 (2016) 10983-11060.

[35] J.C. Groen, T. Bach, U. Ziese, A.M.P. Donk, K. P. De Jong, J.A. Moulijn, J.P. Ramírez, Creation of hollow zeolite architectures by controlled desilication of Al-zoned ZSM-5 crystals, J. Am. Chem. Soc. 127 (2005) 10792-10793.

[36] D. Fodor, L. Pacosova, F. Krumeich, J. A. Van Bokhoven, Facile synthesis of nano-sized hollow single crystal zeolites under mild conditions. Chem. Commun. 50 (2014) 76-78.

[37] Y. Wang, W. Wu, Y. Rao, Z. Li, N. Tsubaki, M. Wu, Cation modulating electrocatalyst derived from bimetallic metal-organic frameworks for overall water splitting, J. Mater. Chem. A 5 (2017) 6170-6177.

[38] P. Zhai, C. Xu, R. Gao, X. Liu, M. Li, W. Li, X. Fu, C. Jia, J. Xie, M. Zhao, X. Wang, Y. Li, Q. Zhang, X. Wen, D. Ma, Highly tunable selectivity for syngas-derived alkenes over zinc and sodium-modulated Fe_5C_2 catalyst, Angew. Chem. Int. Ed. 55 (2016) 9902-9907.

[39] P.M. Maitlis, R. Quyoum, H.C. Long, M.L. Turner, Towards a chemical understanding of the Fischer–Tropsch reaction : alkene formation, Appl. Catal. A: Gen. 186 (1999) 363-374.

[40]   H. Park, S. Oh, S. Lee, S. Choi, M. Oh, Cobalt- and nitrogen-codoped porous carbon catalyst made from core-shell type hybrid metal-organic framework (ZIF-L@ZIF-67) and its efficient oxygen reduction reaction (ORR) activity, Appl. Catal. B-Environ. 246 (2019) 322-329.

[41]   J. Li, R. Hu, H. Qu, Y. Su, N. Wang, H. Su, X. Gu, Radio-frequency thermal plasma-induced novel chainmail-like core-shell MoO_2 as highly stable catalyst for converting syngas to higher alcohols, Appl. Catal. B-Environ. 249 (2019) 63-71.

[42]   T. Ji, R. Tu, L. Mu, X. Lu, J. Zhu, Structurally tuning microwave absorption of core/shell structured CNT/polyaniline catalysts for energy efficient saccharide-HMF conversion, Appl. Catal. B-Environ. 220 (2018) 581-588.

[43] X. Niu, J. Gao, Q. Miao, M. Dong, G. Wang, W. Fan, Z. Qin, J. Wang, Influence of preparation method on the performance of Zn-containing HZSM-5 catalysts in methanol-to-aromatics, *Microporous Mesoporous Mater.* 197 (2014) 252-261.

[44] Y. Wei, T.E. Parmentier, K.P. De Jong, J. Zecevic, Tailoring and visualizing the pore architecture of hierarchical zeolites, Chem. Soc. Rev. 4 (2015) 7234-7261.

[45] C. Fernandez, I. Stan, J. Gilson, K. Thomas, A. Vicente, A. Bonilla, J.P. Ramírez, Hierarchical ZSM-5 zeolites in shape-selective xylene isomerization : role of mesoporosity and acid site speciation, Chem. Eur. J. 16 (2010) 6224-6233.

[46] J.C. Groen, W. Zhu, S. Brouwer, S.J. Huynink, F. Kapteijn, J.A. Moulijn, J.P. Ramírez, Direct demonstration of enhanced diffusion in mesoporous ZSM-5 zeolite obtained via controlled desilication, J. Am. Chem. Soc. 129 (2007) 355-360.

[47] C. Dai, A. Zhang, M. Liu, X. Guo, C. Song, Hollow ZSM-5 with silicon-rich surface, double shells, and functionalized interior with metallic nanoparticles and carbon nanotubes, Adv. Funct.Mater. 25 (2015) 7479-7487.

[48] J. Li, M. Liu, X. Guo, S. Zeng, S. Xu, Y. Wei, Z. Liu, C. Song, Influence of Al coordinates on hierarchical structure and T atoms redistribution during base leaching of ZSM-5, Ind. Eng. Chem. Res. 57 (2018) 15375-15384.

[49] D. Ma, Y. Lu, L. Su, Z. Xu, Z. Tian, Y. Xu, L. Lin, X. Bao, Remarkable improvement on the methane aromatization reaction : a highly selective and coking-resistant catalyst, J. Phys. Chem. B 106 (2002) 8524-8530.

[50]   P. Gao, J. Xu, G. Qi, C. Wang, Q. Wang, Y. Zhao, Y. Zhang, N. Feng, X. Zhao, J. Li, F. Deng, A mechanism study of methanol-to-aromatics reaction over Ga-modified ZSM-5 zeolite: understanding the dehydrogenation process, ACS Catal. 8 (2018) 9809-9820.

Tables and Figures

Table 3.1 Comparison of the space time yield (STY) of aromatics obtained in this work with other literature.

Catalyst	T (°C)	P (MPa)	CO_2 Conv. (%)	CO Sel. (%)	Aromatics Sel. (%) in total HC	GHSV (ml g_{cat}^{-1} h^{-1})	STY of A (g_{CH2} kg_{cat}^{-1} h^{-1})	Reference
Na-Fe@C/H-ZSM-5-0.2M	320	3	33.3	13.3	50.2	9000	203.8	**This work**
Na-Fe₃O₄/H-ZSM-5	320	3	33.6	14.2	40.2	8000	144.9	1
Na/Fe/H-ZSM-5	300	1	21.8	40.9	54.7	4800	52.9	2
ZnAlOx/H-ZSM-5	320	3	9.1	57.4	73.9	4000	17.9	3
In₂O₃/H-ZSM-5	340	3	13.1	44.8	14.6	13500	22.3	4
Zn-ZrO₂/H-ZSM-5	320	4	14.1	44.0	73.0	2400	21.6	5
ZnCrOx/H-ZSM-5	320	5	19.9	70.2	56.5	3000	15.8	6
Cr₂O₃/H-ZSM-5	350	3	34.5	11.4	75.9	2400	87.0	7
Cr₂O₃/Zn-ZSM-5@SiO₂	350	3	22.1	35.1	70.1	1800	30.0	8

Table 3.2. Texture and chemical properties of Fe@C, H-ZSM-5, and hierarchical H-ZSM-5-X.

Sample	S_{BET} (m^2 g^{-1})	S_{BET}^{Micro} (m^2 g^{-1})	S_{BET}^{Meso} (m^2 g^{-1})	V_{Micro} (cm^3 g^{-1})	V_{Meso} (cm^3 g^{-1})	D (nm)	Si/Al[a]
Fe@C	286.6	133.5	153.1	0.07	0.30	5.15	-
H-ZSM-5	385.4	244.6	140.8	0.12	0.15	2.83	40.5
H-ZSM-5-0.1M	395.8	77.6	318.2	0.04	0.27	3.14	35.2
H-ZSM-5-0.2M	419.9	134.1	285.8	0.06	0.44	4.80	32.8
H-ZSM-5-0.4M	345.2	167.3	177.9	0.08	0.77	9.90	25.7

[a]Si/Al ratios in the zeolites were determined by XRF.

Table 3.3. Catalytic performances of Na-Fe@C and multifunctional catalysts Na-Fe@C/H-ZSM-5-X for CO_2 Conversion.[a]

Catalyst	CO_2 Conv. (%)	CO Sel. (%)	Product distribution (%)					o/p[c]	i/p[d]	mass[e]
			CH_4	C_2-C_4^0	C_2-$C_4^=$	C_{5+}[b]	Aromatics			
Fe@C	28.1	17.9	33.1	35.1	5.0	26.7	0	0.09	0.10	93
Na-Fe@C	30.6	14.4	12.6	5.8	29.8	49.8	2.0	5.63	-	91
Na-Fe@C/H-ZSM-5	32.1	12.6	5.8	14.8	0.9	47.6	30.9	0.68	3.56	92
Na-Fe@C/H-ZSM-5-0.1M	30.2	11.9	5.4	15.1	0.4	39.1	40.0	0.42	3.10	94
Na-Fe@C/H-ZSM-5-0.2M	33.3	13.3	4.8	9.6	0.8	34.6	50.2	0.66	3.40	95
Na-Fe@C/H-ZSM-5-0.4M	30.4	24.8	12.4	13.6	1.8	44.4	27.8	0.41	2.95	93

[a]Reaction conditions: 320 °C, 3 MPa, H_2/CO_2/Ar = 71.8/24.3/3.9, GHSV = 9000 mL g_{cat}^{-1} h^{-1}, and time on stream (TOS) = 12 h. Catalyst weight: Na-Fe@C of 0.1 g and zeolite of 0.3 g;
[b]C_{5+} hydrocarbons without aromatics;
[c]ratio of alkenes to linear paraffin;
[d]ratio of iso-paraffin to linear paraffin.
[e]% of mass balance.

Table 3.4. The effect of weight ratios of Na-Fe@C to H-ZSM-5-X on the catalytic performances of CO_2 conversion.[a]

Weight ratio of Na-Fe@C to H-ZSM-5-0.2M	CO_2 Conv. (%)	CO Sel. (%)	Product distribution (%)					o/p[c]	i/p[d]	mass[e]
			CH_4	C_2-C_4^0	C_2-$C_4^=$	C_{5+}[b]	Aromatics			
1 : 1	33.1	13.1	7.2	6.9	4.0	50.3	31.6	1.19	2.17	92
1 : 2	31.6	14.0	5.0	9.3	1.8	38.4	45.5	0.94	3.25	93
1 : 3	33.3	13.3	4.8	9.6	0.8	34.6	50.2	0.66	3.40	94
1 : 5	26.7	25.3	7.9	15.5	1.2	41.3	34.1	0.52	3.56	91

[a]Reaction conditions: 320 ºC, 3 MPa, H_2/CO_2/Ar = 71.8/24.3/3.9, and time on stream (TOS) = 12 h. Catalyst weight: Na-Fe@C of 0.1 g, zeolite of 0.1-0.5 g;
[b]C_{5+} hydrocarbons without aromatics;
[c]ratio of alkenes to linear paraffin;
[d]ratio of iso-paraffin to linear paraffin.
[e]% of mass balance

Table 3.5. The effect of reaction conditions on the catalytic performances of CO_2 conversion over Na-Fe@C/H-ZSM-0.2M.[a]

GHSV (ml g_{cat}^{-1} h^{-1})	T (ºC)	P (MPa)	CO_2 Conv. (%)	CO Sel. (%)	Product distribution (%)					o/p[c]	i/p[d]	mass[e]
					CH$_4$	C$_2$-C$_4$^{0}	C$_2$-C$_4$$^=$	C$_{5+}$[b]	Aromatics			
6000	320	3	31.1	14.9	10.2	15.9	2.0	53.9	18.0	0.33	2.75	94
9000	320	3	33.3	13.3	4.8	9.6	0.8	34.6	50.2	0.66	3.40	93
12000	320	3	28.4	18.2	9.1	10.1	2.9	46.6	31.3	0.88	2.30	92
9000	350	3	38.2	18.7	8.4	13.0	1.8	35.4	41.4	0.81	3.76	93

[a]Reaction conditions: H$_2$/CO$_2$/Ar = 71.8/24.3/3.9, and time on stream (TOS) = 12 h. Catalyst weight: Na-Fe@C of 0.1 g, zeolite of 0.3 g;

[b]C$_{5+}$ hydrocarbons without aromatics;

[c]ratio of alkenes to linear paraffin;

[d]ratio of iso-paraffin to linear paraffin.

[e]% of mass balance

Table 3.6. The catalytic performances of the multifunctional catalyst composed of Na-Fe@C and H-ZSM-5-0.2M with different intimacy modes.[a]

Multifunctional catalyst with different intimacy modes	CO_2 Conv. (%)	CO Sel. (%)	Product distribution (%)					o/p^c	i/p^d	mass[e]
			CH_4	C_2-C_4^0	C_2-$C_4^=$	C_{5+}[b]	Aromatics			
Na-Fe@C&H-ZSM-5-0.2M	15.5	55.5	49.0	27.6	4.3	10.9	8.2	0.23	0.22	92
Na-Fe@C/H-ZSM-5-0.2M	33.3	13.3	4.8	9.6	0.8	34.6	50.2	0.66	3.40	94
Na-Fe@C‖H-ZSM-5-0.2M	29.5	15.0	7.3	5.5	2.1	39.0	46.1	0.75	2.97	95

[a]Reaction conditions: 320 ºC, 3 MPa, $H_2/CO_2/Ar$ = 71.8/24.3/3.9, and time on stream (TOS) = 12 h. Catalyst weight: Na-Fe@C of 0.1 g, zeolite of 0.3 g;
[b]C_{5+} hydrocarbons without aromatics;
[c]ratio of alkenes to linear paraffin;
[d]ratio of iso-paraffin to linear paraffin.
[e]% of mass balance

Table 3.7. Catalytic performances of 1-hexene conversion over H-ZSM-5-0.2M, Na-Fe@C*/H-ZSM-5-0.2M, and Na-Fe@C*/H-ZSM-5 under N_2 or CO_2 atmospheres.

Catalyst	Atmosphere	Product distribution (%)				$mass^b$
		CH_4	C_2-C_4	C_{5+}	Aromatics	
H-ZSM-5-0.2M	CO_2	0	26.6	41.4	32.0	96
Na-Fe@C/H-ZSM-5-0.2M	CO_2	0.1	34.0	20.1	45.8	97
Na-Fe@C/H-ZSM-5-0.2M	N_2	0.1	32.9	29.6	37.4	96
H-ZSM-5-0.2M	N_2	0	26.4	45.6	28.0	98
Na-Fe@C/H-ZSM-5	CO_2	0.2	42.6	30.5	26.7	94

[a]Reaction conditions: 320 °C, 2 MPa, catalyst weight 1 g zeolite and 0.33 g Na-Fe@C*, liquid 1-hexene flow rate 0.005 mL min^{-1}, TOS = 8 h.
[b]% of mass balance
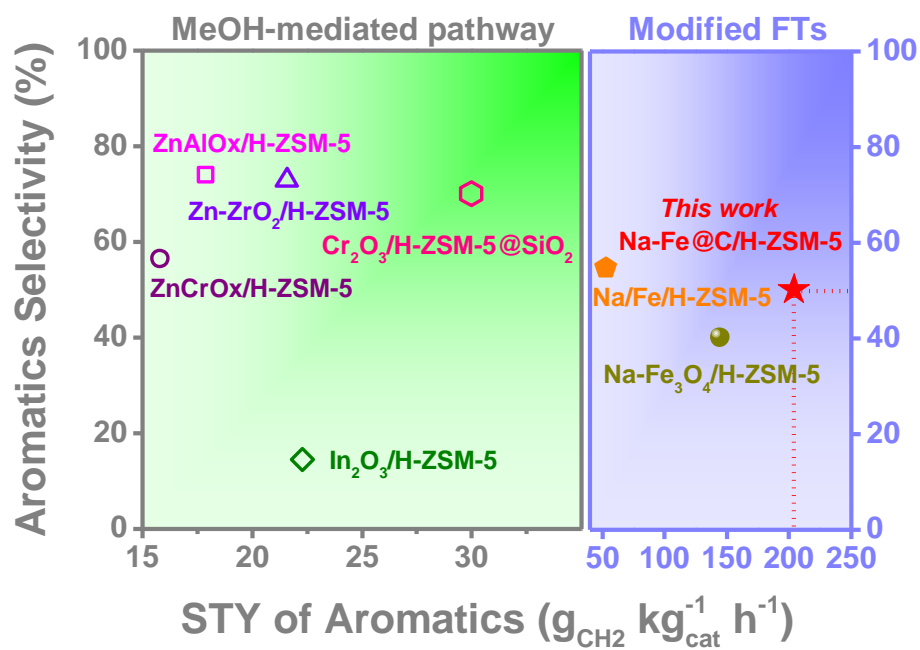
Figure 3.1. Comparison of the space time yield (STY) of aromatics obtained in this work with other literature.
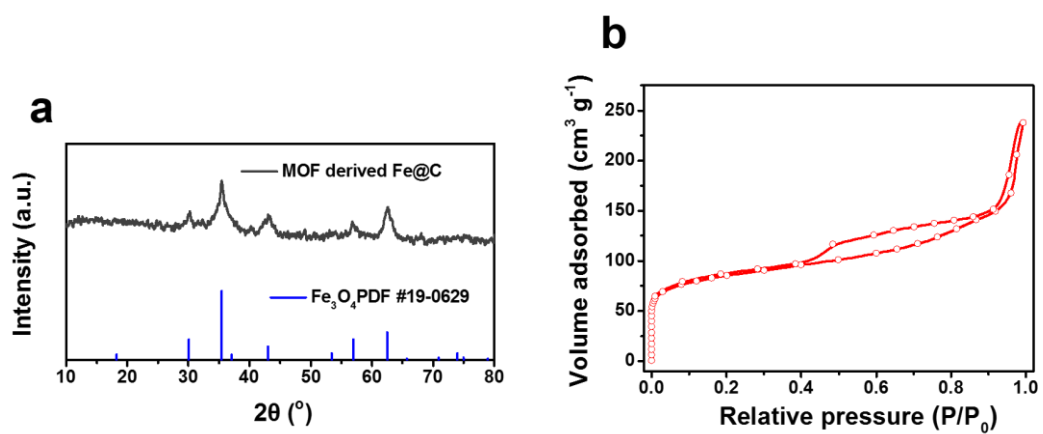
Figure 3.2. XRD pattern (a) and N_2 adsorption-desorption isotherm of the Fe-MOFs derived Fe@C catalys
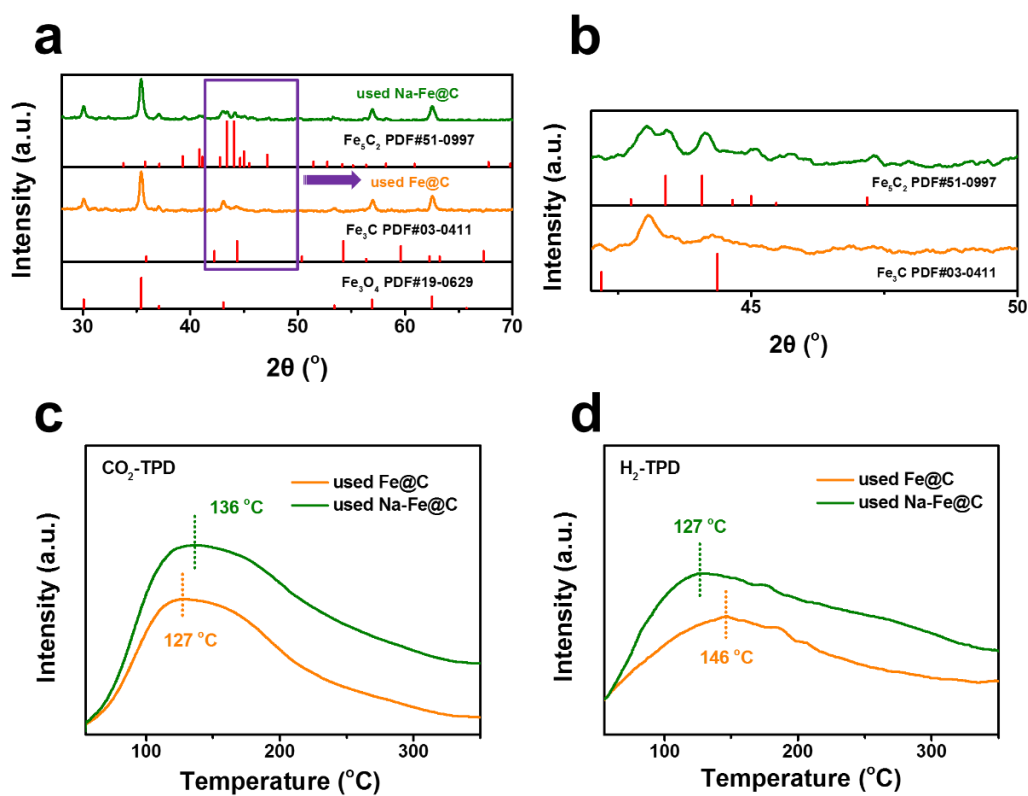
Figure 3.3. XRD patterns (a), CO_2-TPD (c), and H_2-TPD (d) profiles of the used Fe@C and Na-Fe@C. (b) is the enlarged picture of the plotted part in (a).
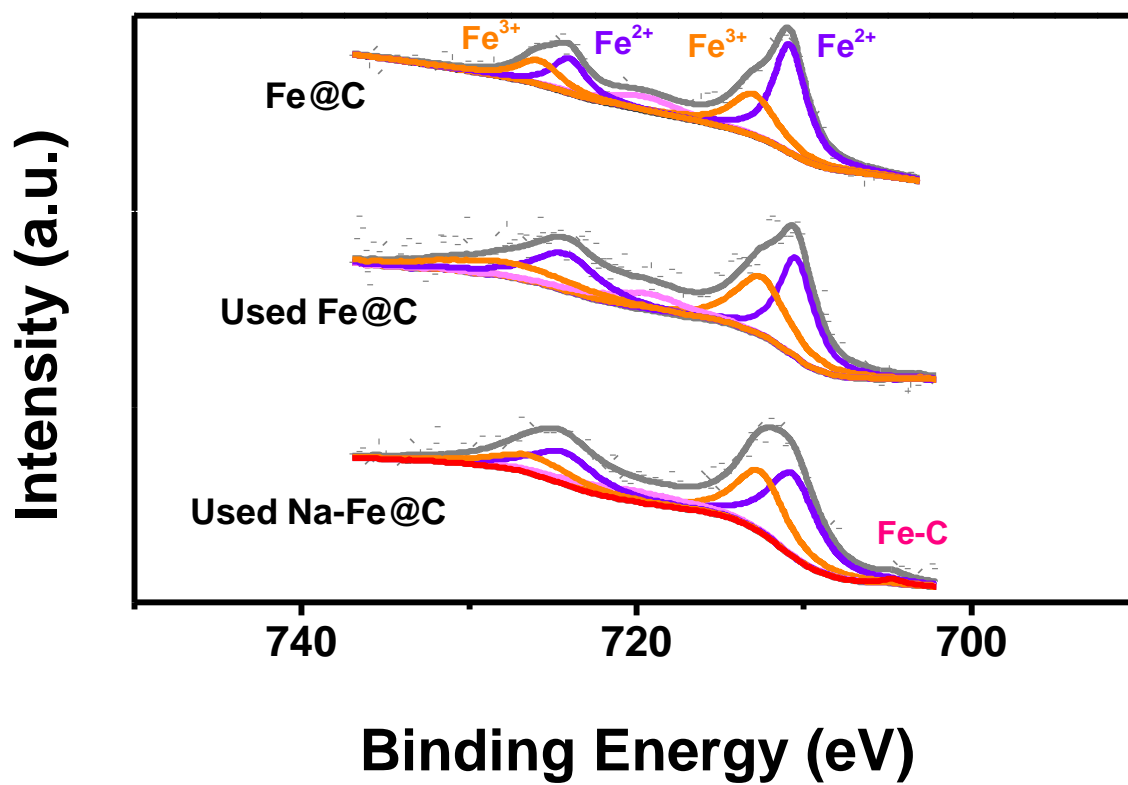
**Figure 3.4.** XPS spectra of fresh Fe@C, used Fe@C, and used Na-Fe@C.
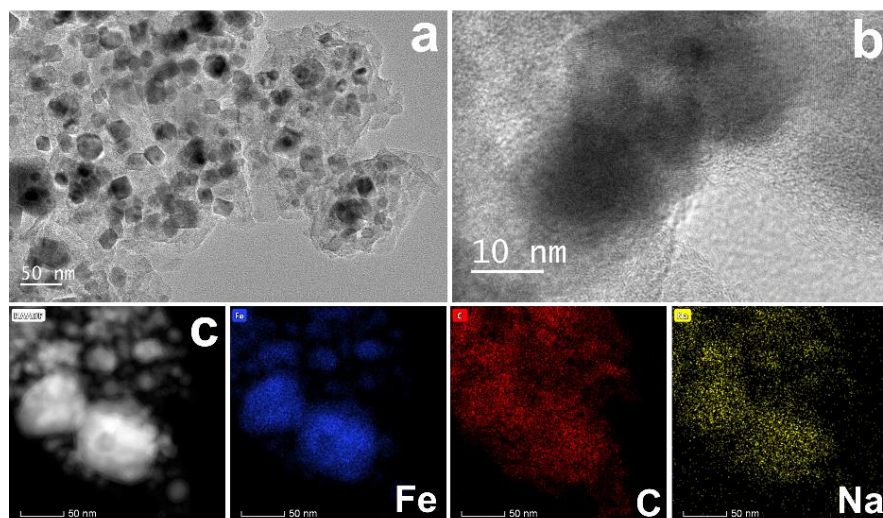
Figure 3.5. (a) TEM and (b) High Resolution TEM (HRTEM) images of the used Na-Fe@C catalyst. (c) STEM image of the used Na-Fe@C and the corresponding elemental mapping of iron (Fe), carbon (C), and sodium (Na) elements.
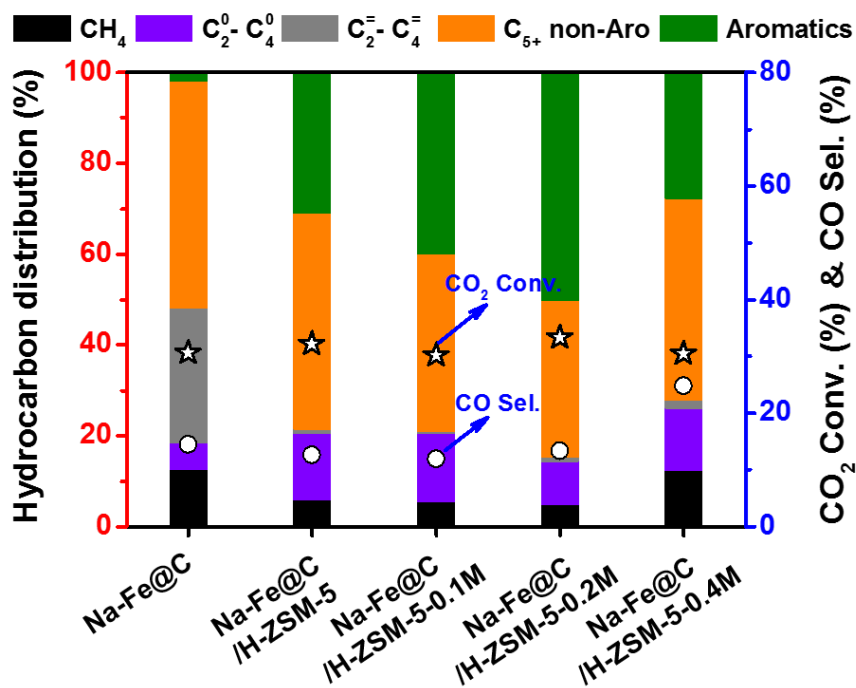
Figure 3.6. Catalytic performances of Na-Fe@C and multifunctional catalysts Na-Fe@C/H-ZSM-5-X for CO_2 conversion. Reaction conditions: 320 ℃, 3 MPa, $H_2/CO_2/Ar$ = 71.8/24.3/3.9, GHSV = 9000 mL g_{cat}^{-1} h^{-1}, and time on stream (TOS) = 12 h. Catalyst weight, Na-Fe@C of 0.1 g and zeolite of 0.3 g.
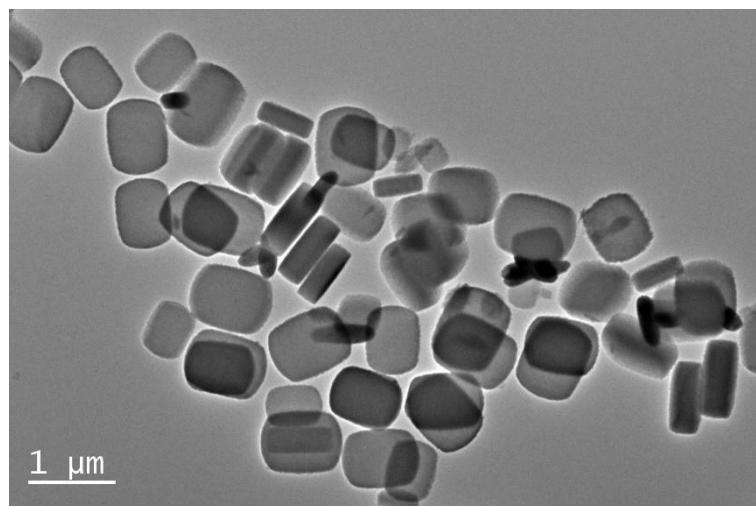
Figure 3.7. TEM image of the parent H-ZSM-5 with bulk structure.
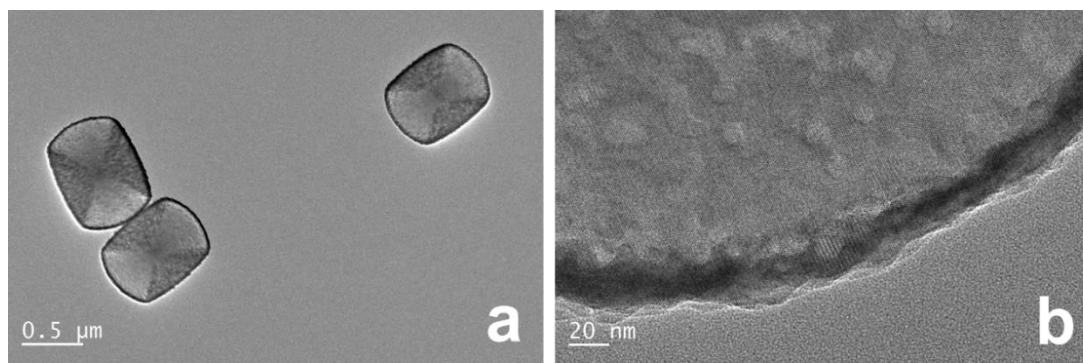
Figure 3.8. TEM (a) and HRTEM (b) images of H-ZSM-5-0.2M.
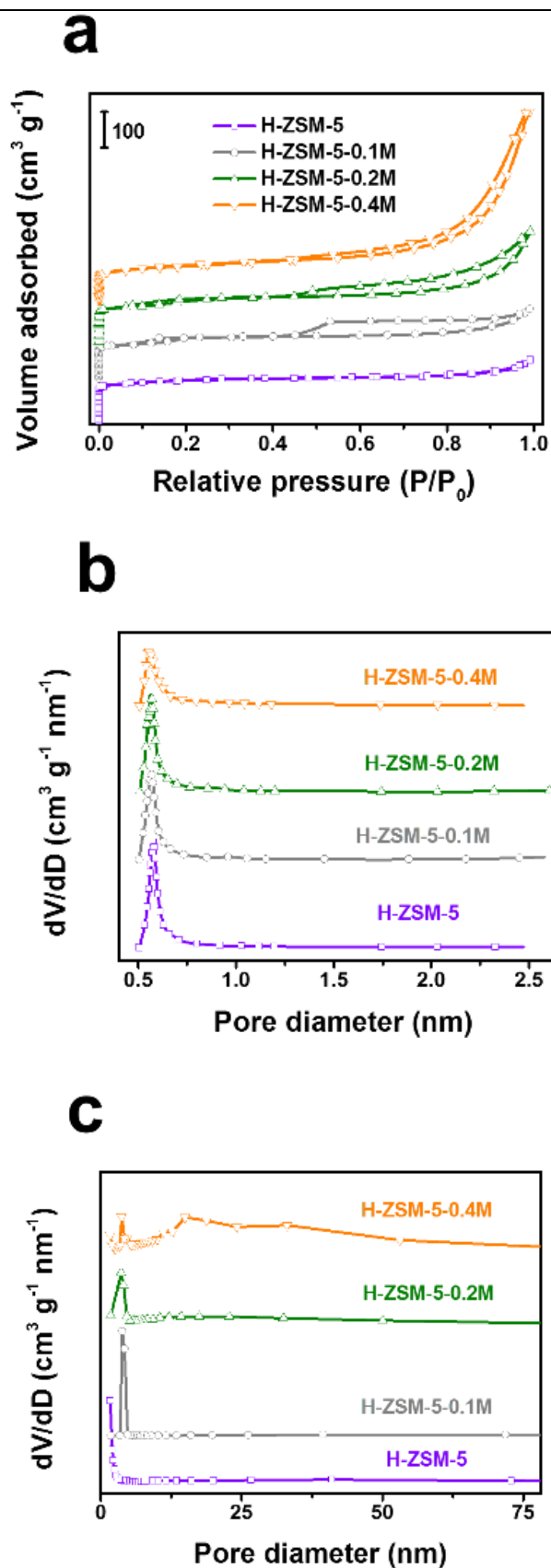
Figure 3.9. N_2 adsorption-desorption isotherms (a) and pore size distributions calculated by HK (b) and BJH (c) methods of the parent H-ZSM-5 and NaOH treated H-ZSM-5.
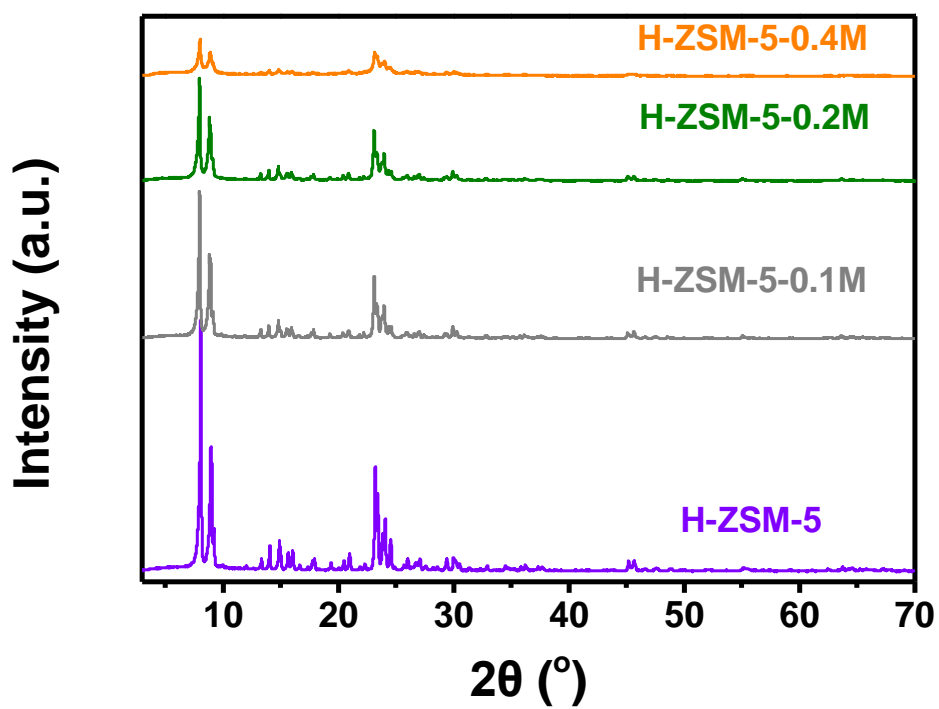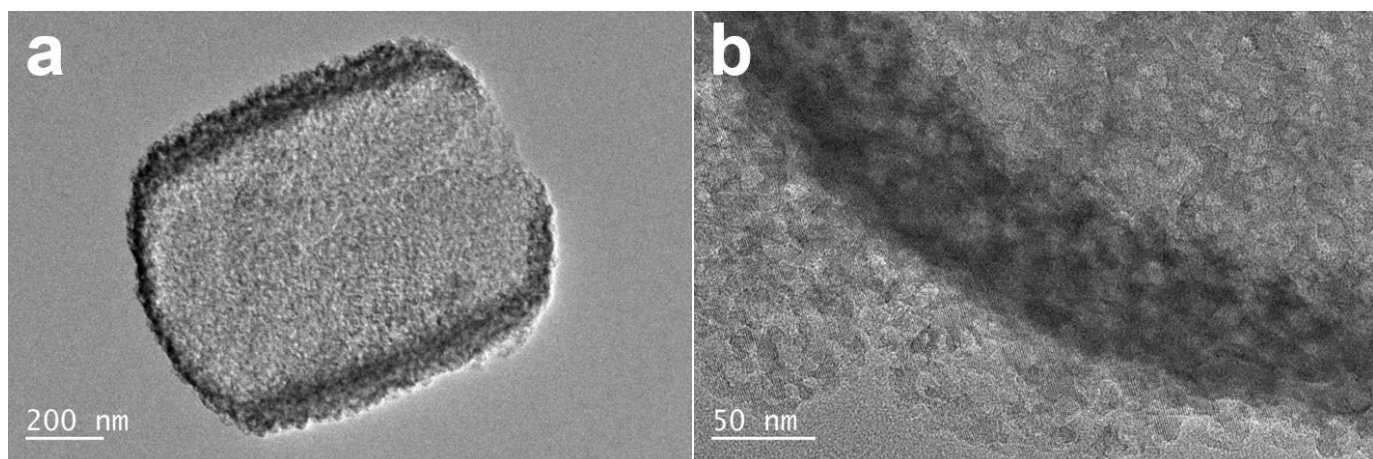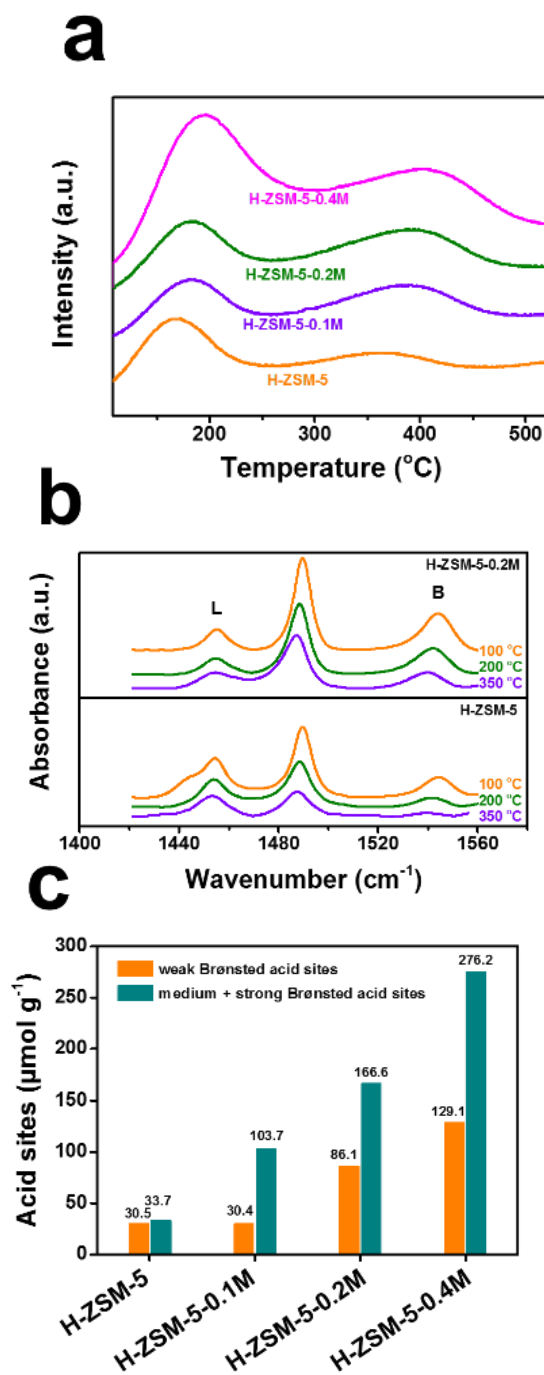
Figure 3.10. XRD patterns of H-ZSM-5 and H-ZSM-5-X prepared with different concentrations of NaOH solution.
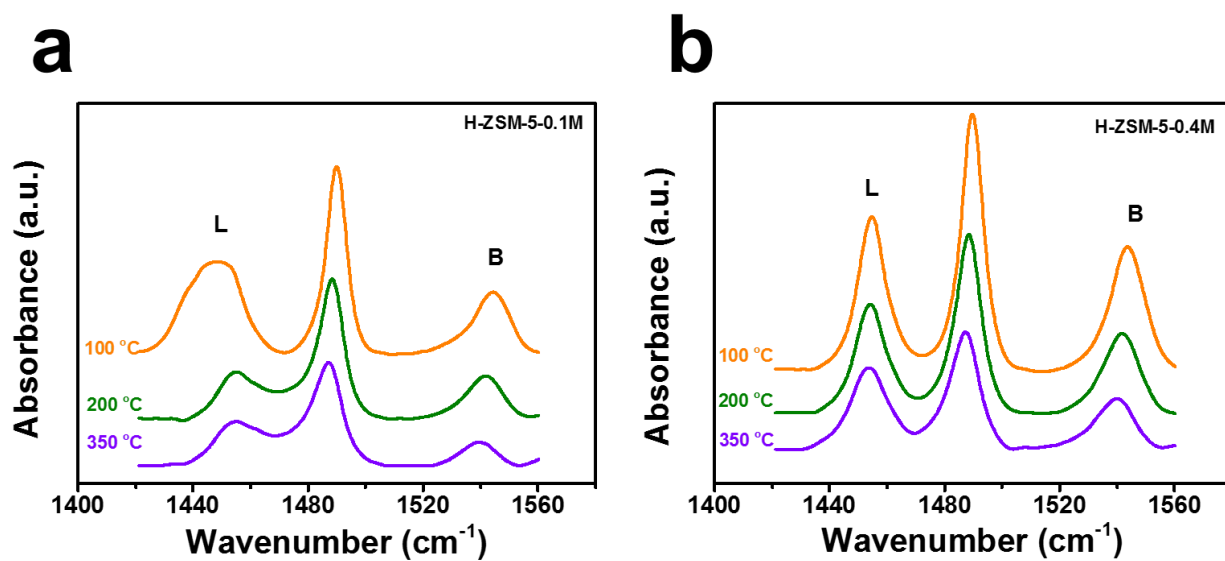
Figure 3.11. TEM images of H-ZSM-0.4M.

Figure 3.12. (a) NH$_3$-TPD profiles of H-ZSM-5 and H-ZSM-5-X, (b) FTIR spectra of adsorbed pyridine on H-ZSM-5 and H-ZSM-5-0.2M at different temperatures, (c) the number of Brønsted acid sites in H-ZSM-5 and H-ZSM-5-X.

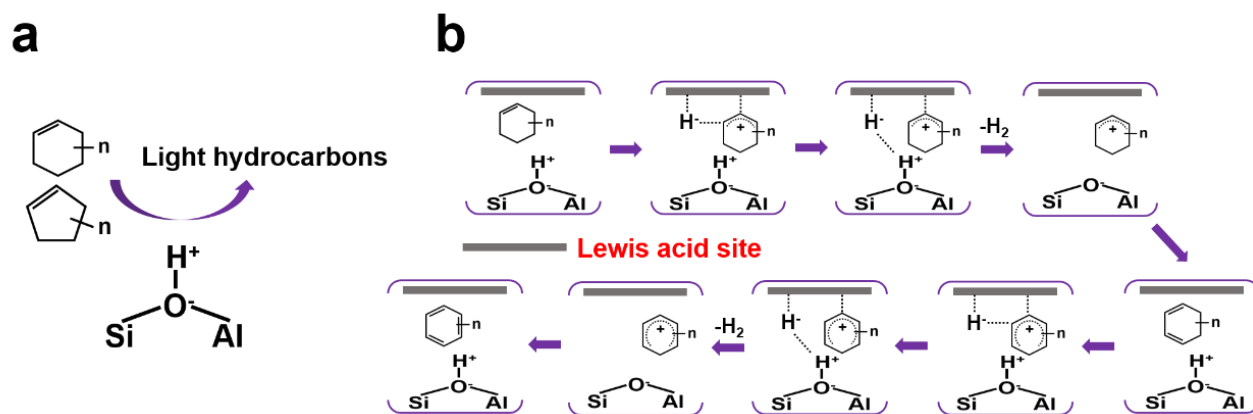**Figure 3.13.** FTIR spectra of adsorbed pyridine on H-ZSM-5-0.1M and H-ZSM-5-0.4M at different temperatures.
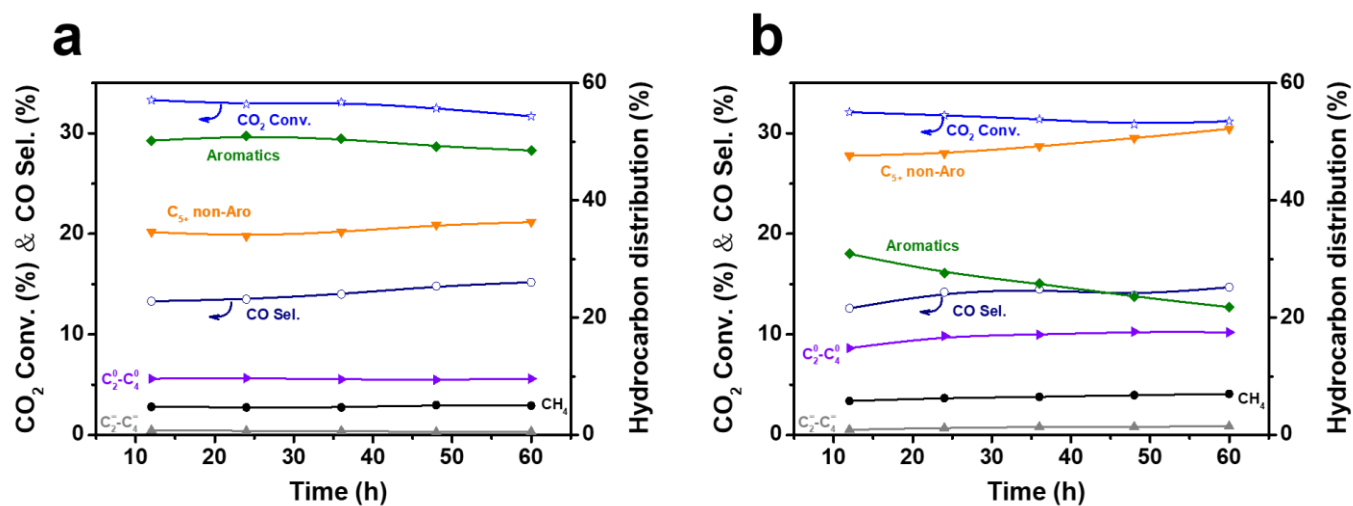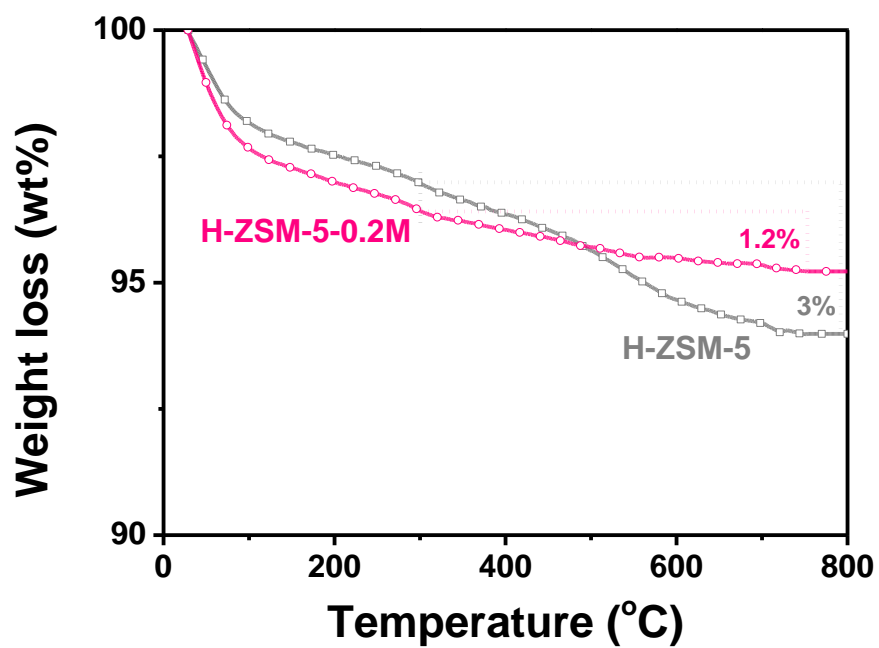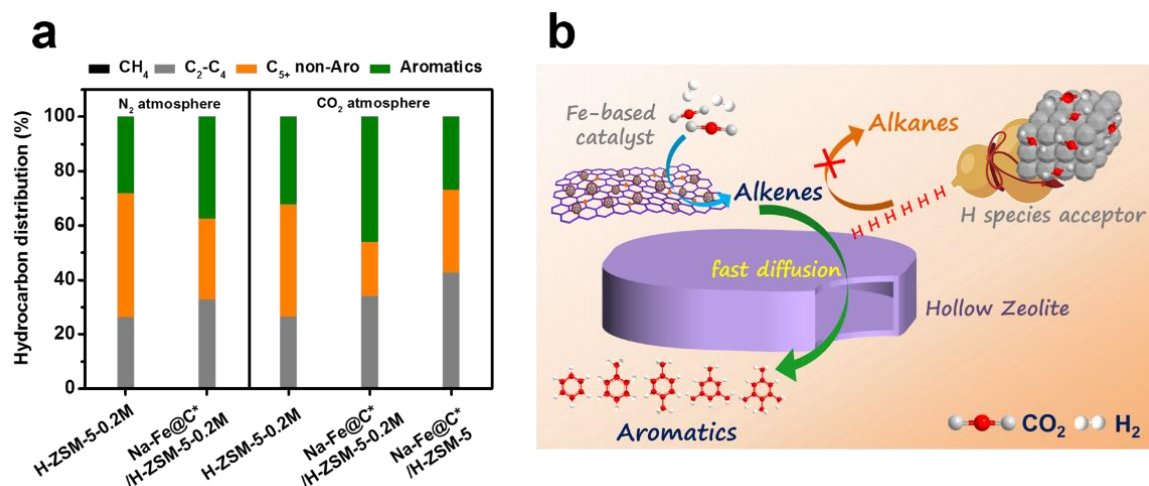
Figure 3.14. (a) Cracking of cycloalkenes on the Brønsted acid site; (b) reaction mechanism of aromatics synthesis via the synergistic effect between Brønsted and Lewis acid sites.

Figure 3.15. Long-term stability of (a) Na-Fe@C/H-ZSM-5-0.2M and (b) Na-Fe@C/H-ZSM-5.

Figure 3.16. TG curves of the spent H-ZSM-5 and H-ZSM-5-0.2M after tandem

reaction.

Figure 3.17. (a) Catalytic performances of 1-hexene conversion over H-ZSM-5-0.2M, Na-Fe@C*/H-ZSM-5-0.2M (Na-Fe@C* represents the used Na-Fe@C), and Na-Fe@C*/H-ZSM-5 under N_2 or CO_2 atmosphere. Reaction conditions, 320 °C, 2 MPa, catalyst weight 1 g zeolite and 0.33 g Na-Fe@C*, liquid 1-hexene flow rate 0.005 mL min^{-1}, TOS = 8 h. (b) Schematic representation of the cooperative interplay between the multifunctional catalyst for the enhanced aromatics synthesis from CO_2 hydrogenation.

Chapter 4

Summary

Due to with the fossil resource decreasing and the serious pollution caused by fossil fuel combustion, the jet fuels and low-carbon aromatics synthesis by petroleum-free method has attracted a wide range of academic and industrial interest in past decades. It has become one of the most attractive research fields in heterogeneous catalysis.

In this thesis, we successfully found new ways are beneficial to designing and building new catalysis reactions and new catalysts in jet fuels and low-carbon aromatics synthesis from sample renewable resources. We designed and synthesized three types of high performance of the catalysts with special structure, and various reaction systems were used to test the catalytic performance. H-Y, SAPO-34, H-MOR zeolite and Al-MCM-41 catalysts for catalytic isobutyl alcohol oligomerization to generate liquid fuels. Various dealuminum methods of zeolite Beta to generate the jet fuels by converting isobutyl alcohol. Multifunctional catalyst composed of Na-Fe@C and hollow H-ZSM-5 was used to directly convert CO_2 to low-carbon aromatics.

Chapter 1 offers a series of zeolites were adopted for dehydration reaction of isobutyl alcohol to generate liquid hydrocarbon fuels. SAPO-34 zeolite was easy to be deactivated due to the presence of microporous, while Al-MCM-41 zeolite was also not suitable for dehydration process owing to the low weak acid sites. By contrary, isobutyl alcohol conversion of 82% and C_{5+} olefins of 58% were achieved on H-MOR zeolite at 240°C. In addition, the conversion was enhanced with increasing temperature and reached its maximum at 240°C. Obviously, the factors that affect the catalytic performance include not only the physicochemical properties of catalysts (such as pore structure and the acid sites) but also the physical properties of isobutyl alcohol. With the proceeding of reaction, the conversion of the catalysts was increased rapidly at first 4 h from 30% to 82% and then slowly increased to the maximum level of 94% at 10 h. According to the results of TG/DTA, the generating of hard coke made the deactivation

of the catalyst rapidly. These findings provide new insights for the potential applications of isobutyl alcohol oligomerization to liquid hydrocarbon fuels.

As mentioned in Chapter 2, we used various dealuminization methods, with HCl and EDTA as acids, to treat zeolite, by which to effectively adjust the pore structure and acidity of Beta zeolite. With the obtained zeolite as catalysts, we also investigated their catalytic performance for isobutyl alcohol oligomerization to synthesize jet fuels. Although undergoing dealumination processes, the Beta zeolite still remains its integrated channels and framework. The employed dealumination process could effectively remove the extra-framework aluminum and impurities. As a result, the pores of zeolite samples become smoother, by which to further improve their catalytic activity. Due to the dealumination process, the total acidic sites and the number of Brønsted acid sites on zeolite were reduced to some extent. However, the increased ratio of Lewis/Brønsted acidic sites was available for promoting the oligomerization reaction step to form jet fuels. Meanwhile, the promoted oligomerization reaction step also facilitated the dehydration reaction step of isobutyl alcohol. Among the tested catalysts, the HCL2h-BEA catalyst exhibited the highest conversion of 98% and the highest C_{8-16} selectivity of 59%. In addition, after removing the carbon deposit on this HCL2h-BEA catalyst by calcination, this spent catalyst also given similar catalytic performance to its fresh one.

As mentioned in Chapter 3, The direct conversion of CO_2 to aromatics was realized by a multifunctional catalyst Na-Fe@C/H-ZSM-5-0.2M with precisely tailored catalytic interface and acidity. Na-Fe@C prepared by pyrolysis of Fe-based MOFs exhibited high alkenes selectivity (70.6%) at a CO_2 conversion of 30.6% due to its appropriate intermediate adsorption capability and high active sites accessibility. After combining with alkali-treated acidic H-ZSM-5, the alkenes produced from Na-Fe@C were converted to aromatics through the dehydrogenative aromatization reaction. The suitable acid density and strength in the multifunctional catalyst, which play a vital role in the synthesis of aromatics, were systematically investigated. Different from the simple combination of two catalyst components, the cooperative interplay between Na-

Fe@C and H-ZSM-5-0.2M guaranteed the enhanced aromatics synthesis from the tandem CO_2 conversion. CO_2 adsorbed on Fe-based catalyst acted as acceptors for the H species produced from the dehydrogenation and cyclization reactions, thereby accelerating the conversion of alkenes to aromatics by shifting the thermodynamic equilibrium. Our study not only provides a novel multifunctional catalyst system for direct conversion of CO_2 to value-added aromatics but also sheds new light on the sustainable strategy to alleviate the environmental pressure derived from carbon emissions.

List of publications

1.**Xiaoyu Guo,** Lisheng Guo, Yuichi Suzuki, Jinhu Wu, Yoshiharu Yoneyama, Guohui Yang, Noritatsu Tsubaki. Catalytic Oligomerization of Isobutyl Alcohol to Hydrocarbon Liquid Fuels over Acidic Zeolite Catalysts. *ChemistrySelect*, Vol. 5(2), 528–532, 2020(IF=1.811)

2. **Xiaoyu Guo,** Lisheng Guo, Yan Zeng, Rungtiwa Kosol, Xinhua Gao, Yoshiharu Yoneyama, Guohui Yang, Noritatsu Tsubaki. Catalytic oligomerization of isobutyl alcohol to jet fuels over dealuminated zeolite Beta. *Catalysis Today*, in press, 2020 (IF=5.825)

3. Yang Wang, Shun Kazumi, Weizhe Gao, Xinhua Gao, Hangjie Li, **Xiaoyu Guo,** Yoshiharu Yoneyama, Guohui Yang, Noritatsu Tsubaki. Direct conversion of CO2 to aromatics with high yield via a modified Fischer-Tropsch synthesis pathway. *Applied Catalysis B: Environmental,* Vol. 269, 118792, 2020(IF=16.683)

Related publications

1. **<u>Xiaoyu Guo</u>**, Lisheng Guo, Yu Cui, Tharapong Vitidsant, Prasert Reubroycharoen, Guangbo Liu, Jinhu Wu, Yoshiharu Yoneyama, Guohui Yang, Noritatsu Tsubaki. Enhanced α-olefins selectivity by promoted CO adsorption on ZrO2@FeCu catalyst. *Catalysis Today,* in press, 2020 (IF=5.825)

2. AL-Hassan Nasser, Lisheng Guo, Hamada ELnaggar, Yang Wang, **<u>Xiaoyu Guo,</u>** Ahmed Abdel Moneim and Noritatsu Tsubaki. Mn–Fe nanoparticles on a reduced graphene oxide catalyst for enhanced olefin production from syngas in a slurry reactor. *RSC Advances,* Vol.8, 14854-14863, 2018(IF=3.070)

3. Yingluo He, Jiaming Liang, Yusuke Imai, Koki Ueda, Hangjie Li, **<u>Xiaoyu Guo,</u>** Guohui Yang, Yoshiharu Yoneyama, Noritatsu Tsubaki. Highly selective synthesis of methanol from methane over carbon materials supported Pd-Au nanoparticles under mild conditions. *Catalysis Today*, in press, 10.1016/j.cattod.2019.10.017, 2019(IF=5.825)

4. Li Tan, **<u>Xiaoyu Guo</u>**, Xinhua Gao, Noritatsu Tsubaki. Designing a Mesoporous Zeolite Catalyst for Products Optimizing in n-Decane Hydrocraking. *Catalysts*, Vol. 9, 766, 2019(IF=3.623)

5. Lisheng Guo, Jie Li, Yan Zeng, Rungtiwa Kosol, Yu Cui, Naoya Kodama, **<u>Xiaoyu Guo</u>**, R. Prasert, V. Tharapong, Guangbo Liu, Jinhu Wu, Guohui Yang, Yoshiharu Yoneyama, Noritatsu Tsubaki. Heteroatom doped iron-based catalysts prepared by urea self-combustion method for efficient CO2 hydrogenation. *Fuel,* Volume 276, 118102, 2020(IF=5.578)

List of conferences

(1) **<u>Xiaoyu Guo,</u>** Yang Wang, Lisheng Guo, Guohui Yang, Noritatsu Tsubaki, Nano-capsule catalyst ZrO2@FeCu for enhanced liquid fuels synthesis via Fischer-Tropsch technology in slurry bed, Bangkok, Thailand, 2019, The 8th Asia-Pacific Congress on Catalysis(APCAT-8), Oral.

(2) **<u>Xiaoyu Guo,</u>** Yang Wang, Lisheng Guo, Guohui Yang, Noritatsu Tsubaki, Enhanced α-olefins selectivity by promoted CO adsorption on ZrO2@FeCu catalyst, Toyama, Japan, 2019, The 29th Characterization conference (第 29 回キャラクタリゼーション講習会), post

Acknowledgments

I wish to express my deep appreciation to my supervisor, Professor Noritatsu Tsubaki, for his warm-heart encouragement and the most valuable advice, especially for giving me this opportunity to study in Japan for both master and doctor degrees. What is more important is that his profound erudition and rigorous attitude to science influenced me profoundly, inspiring me to move towards the scientific way of passing the future. Without his pushing, encouragement, and guidance, I could not have completed this paper.

My sincere thanks also go to Associate Professor. Guohui Yang, for his invaluable guidance, constant encouragement, and precise modification, and I admire his knowledge and personality. I shall extend my thanks to Associate Professor Yoshiharu Yoneyama for providing me with advice and assistance in the experiment. Their keen and vigorous academic observation enlighten me in my doctor academic career and my future study.

I would like to give my deeply thanks to the senior and junior sisters and brothers apprentice of Tsubaki Lab for offering me a lot of help in my experiment and life. They are Dr. Xinhua Gao, Dr Jie Li, Dr. Qinhong Wei, Dr, Minghui Tan, Dr. Peipei Ai, Dr. Peipei Zhang, Dr. Li Tan, Dr. Guoguo Liu, Dr. Yang Wang, Dr. Xiaobo Feng, Dr. Hangjie Li, Dr. Lisheng Guo, Dr. Yuan Fang, Dr. Yingluo He, Miss Yan Zeng, Miss Kosol, Mr. Yu Cui, Mr. Kangzhou Wang, Mr. Weizhe Gao, Mr. Baizhang Zhang, Mr. Jie Yao, Mr. Fei Chen, Mr. Chengwei Wang, Mr. Jiaming Liang, Mr. Jiaqi Fan, Mr. Liwei Xiao, Mr. Wenhang Wang, Mr. Xu Sun. Besides, I also want to thank Dr, Xiaobo Peng, Dr. Liang Wang, Dr. Ye Tian, Dr. Jian Zhang, Dr. Guangbo Liu, Mrs. Hongli Wu, Mr. Yuichi Suzuki, Mr. Araki, Miss Tammy, Mr. Jaru, and many other researchers and students in the university of Toyama for their assistance in study and life.

Last but not least, I would like to express my thanks to my beloved family and my friends for their continued encouragement and spiritual support during my study.